

Department of Physics  
University of Fribourg (Switzerland)

**Magnetic Proximity Effect in Oxide-Based  
Superconductor/Ferromagnet and  
Superconductor/Antiferromagnet Heterostructures**

Thesis

Presented to the Faculty of Science of the University of Fribourg (Switzerland)  
in consideration for the award of the academic degree of  
*Doctor rerum naturalium*

by

**Kaushik Sen**

from Rajbalhat, India

Thesis No. 1981  
UniPrint, Fribourg  
2016

Accepted by the Faculty of Science of the University of Fribourg (Switzerland) upon the recommendation of

Prof. Dr. Antoine Weis	University of Fribourg, Switzerland	President of the Jury
Prof. Dr. Christian Bernhard	University of Fribourg, Switzerland	Thesis Supervisor
Prof. Dr. Philipp Aebi	University of Fribourg, Switzerland	Examiner
Prof. Dr. Christof Niedermayer	Paul Scherrer Institute, Switzerland	Examiner

Fribourg, July 13, 2016

Thesis supervisor:

Dean:



.....  
Prof. Dr. Christian Bernhard



.....  
Prof. Dr. Fritz Müller





# Abstract

The first topic of this thesis concerns a study of the magnetic proximity effect (MPE) in  $\text{YBa}_2\text{Cu}_3\text{O}_7/\text{La}_{2/3}\text{Ca}_{1/3}\text{MnO}_3$  (YBCO/LCMO) multilayers (MLs). In particular, it has been investigated how the strength of the antiferromagnetic exchange interaction (AEI) between the interfacial Cu and Mn ions depends on the electronic and magnetic properties of the LCMO layers. It was previously shown that this MPE gives rise to a ferromagnetic moment of the interfacial Cu ions that is antiparallel to the one of the Mn ions of LCMO [1–4]. This phenomenon has been explained in terms of a covalent bonding between the Cu  $3d_{3z^2-r^2}$  and Mn  $3d_{3z^2-r^2}$  orbitals of the interfacial Cu and Mn ions which gives rise to an induced ferromagnetic Cu moment and a AEI with the Mn moment [1]. This covalent bonding is also at the heart of an orbital reconstruction of the interfacial Cu ions which leads to a comparable occupation of the  $3d_{3z^2-r^2}$  and  $3d_{x^2-y^2}$  orbitals [5]. To further explore the relevancy of this model in this study, it has been investigated how the interfacial ferromagnetic Cu moment depends on the electronic properties of the LCMO layers and the related orbital order of the Mn ions. In particular, it has been tested whether the strength of the orbital reconstruction, the magnitude of the induced ferromagnetic Cu moment and the strength of its AEI with the Mn moments are indeed correlated as is suggested by the covalent model of Ref. [1].

Three types of YBCO/LCMO MLs (denoted as YL\_1, YL\_2 and YL\_3) were grown on (001)-oriented  $\text{Sr}_{0.7}\text{La}_{0.3}\text{Al}_{0.65}\text{Ta}_{0.35}\text{O}_3$  (LSAT) substrates with pulsed laser deposition (PLD). The properties of their LCMO layers have been modified by changing their growth and annealing conditions. For all three types of MLs, the YBCO layers exhibit reasonably sharp superconducting (SC) transitions with the transition temperatures in the range of  $T_C \approx 70$ -75 K. The Curie temperatures of the LCMO layers in YL\_1 and YL\_2 are fairly high with  $T^{\text{Curie}} = 215$  and 180 K, respectively. The average values of the low-temperature magnetization amount to 2.0 and 2.5  $\mu_B$  per Mn ion, respectively. Despite of the comparable ferromagnetic orders, the electronic properties of the LCMO layers in YL\_1 and YL\_2 exhibit notable differences. Whereas in YL\_1 the charge carriers in LCMO are itinerant, in YL\_2 their mobility is strongly reduced due to polaronic effects. These polarons maintain the ferromagnetic order, but involve a specific kind of orbital order that is very different from the one in the itinerant ferromagnetic state. Finally, in YL\_3, the ferromagnetic order of the Mn moments is strongly suppressed with an average magnetization of only 0.25  $\mu_B$  per Mn ion.

With x-ray linear dichroism (XLD) studies, it was found that the interfacial Cu ions in all three samples undergo a similar orbital reconstruction. With corresponding x-ray magnetic circular dichroism (XMCD) experiments, it was furthermore shown that in the three kinds of MLs, the ferromagnetic Cu moments have similar magnitudes in the range of 0.11-0.24  $\mu_B$ . Nevertheless, contrary to the prediction of the covalent bonding model of Ref. [1], it was found that the strength of the AEI with the Mn moments exhibits a large variation in these different MLs, i.e., it is strong in YL\_1, very weak in YL\_2 and entirely absent in YL\_3. Most stunning is the big difference in the strength of the AEI between YL\_1 and YL\_2 for which the LCMO layers are strongly ferromagnetic. The findings suggest that the Cu moments are not induced by the AEI with the Mn moment, but rather intrinsic to the interfacial  $\text{CuO}_2$  planes for which the Cu ions undergo the orbital reconstructions. Furthermore, the strong suppression of the AEI in YL\_2 has been explained in terms of the specific kind of orbital order of the ferromagnetic polarons in the LCMO layers.

The second topic of this thesis involves a study of the superconductivity and the charge car-

rier localization in  $\text{La}_{1.85}\text{Sr}_{0.15}\text{CuO}_4$  (LSCO) ultrathin films. The LSCO films with  $\text{La}_2\text{CuO}_4$  (LCO) and LCMO capping layers of various thicknesses were grown with PLD on (001)-oriented  $\text{SrLaAlO}_4$  (SLAO) substrates. For the heterostructures that were grown in pure  $\text{N}_2\text{O}$  gas (growth mode A), the first LSCO monolayer next to the substrate is strongly disordered. This disorder could be substantially reduced by growing in a mixture of  $\text{N}_2\text{O}$  and  $\text{O}_2$  gases (growth mode B). The structural characterization of the samples confirmed that the LSCO and LCO layers are almost fully strained and the LCMO layers are partially strain relaxed. A single LSCO film with a thickness of 7 unit cell (u.c.) from growth mode A has a sharp superconducting transition with an onset temperature of  $T_{C,on} \approx 38$  K. A single LCMO film (20 u.c. with growth mode A) have  $T^{Curie}$  of about 190 K, and the low-temperature magnetization  $2.0 \mu_B$  per Mn ion.

The LSCO(N u.c.)/LCO(2 u.c.) bilayers (BLs) of N=2-5 from growth mode A are still superconducting with  $T_{C,on}$  in the range of 30-38 K. The  $T_C$  and  $T_{C,on}$  values are somewhat reduced for the corresponding LSCO(N u.c.)/LCMO(20 u.c.) BLs. This is possibly due to the injection and/or diffusion of spin polarized charge carriers across the interface from the ferromagnetic LCMO into the superconducting LSCO layers. This effect due to the ferromagnetism of the LCMO layer is apparently limited to the first LSCO monolayer next to the LSCO/LCMO interface. Surprisingly, the  $T_C$  values are much more strongly reduced in the corresponding LSCO(N u.c.)/LCO(2 u.c.)/LCMO(20 u.c.) trilayers (TLs). Remarkably, the TLs for N=2 & 3, exhibit a charge carrier localization at low temperature. Similar charge localization phenomena at low temperature are evident in a LSCO(3 u.c.)/LCO(7 u.c.) BL. The magneto-transport data suggest that the charge carriers are localized in a static antiferromagnetic background. It is further shown that this charge carrier localization is reproducible in another set of LSCO/LCO BLs from the growth mode B. These systematic studies reveal that this charge carrier localization occurs right at the LSCO/LCO interface. Several potential mechanisms are discussed which could lead to this kind of charge carrier localization.

# Zusammenfassung

Der erste Teil dieser Arbeit behandelt die Untersuchung des magnetischer Proximity-Effekt (MPE) in  $\text{YBa}_2\text{Cu}_3\text{O}_7/\text{La}_{2/3}\text{Ca}_{1/3}\text{MnO}_3$  (YBCO/LCMO) Multilagen (MLs). Insbesondere wurde untersucht, wie die antiferromagnetische Austauschwechselwirkung (AEI) der Cu und Mn Ionen von den elektronischen und magnetischen Eigenschaften der LCMO Lagen abhängt. In vorherigen Arbeiten wurde bereits gezeigt, dass dieser MPE ein ferromagnetisches Moment erzeugt, sodass das Moment des Cu Ions antiparallel zu dem des Mn Ions vom LCMO steht [1–4]. Dieses Phänomen wurde durch eine kovalente Bindung zwischen den Cu  $3d_{3z^2-r^2}$  und der Mn  $3d_{3z^2-r^2}$  2 Orbitalen der angrenzenden Cu und Mn Ionen erklärt, welches ein ferromagnetisches Cu Moment und einer AEI im Mn Moment erzeugt [1]. Diese kovalente Bindung ist ebenfalls das Kernstück einer orbitalen Rekonstruktion der angrenzenden Cu Ionen, welche zu einer vergleichbaren Besetzung der  $3d_{3z^2-r^2}$  und  $3d_{x^2-y^2}$  Orbitale führt [5]. Um weiterhin die Relevanz dieses Modells in der folgenden Arbeit zu erkunden, wurde untersucht wie das angrenzende Cu Moment von den elektronischen Eigenschaften der LCMO Lagen und der damit zusammenhängenden orbitalen Ordnung des Mn Ions abhängt. Insbesondere wurde überprüft, ob die Stärke der orbitalen Rekonstruktion, die Größe des induzierten ferromagnetischen Cu Momentes und die Stärke AEI mit den Mn Momenten tatsächlich miteinander korrelieren, wie es von dem kovalenten Modell in [1] vorgeschlagen wurde.

Drei Arten von YBCO/LCMO MLs (namentlich YL\_1, YL\_2 and YL\_3) wurden mittels Gepulster Laserdeposition (PLD) auf einem (001)-orientierten  $\text{Sr}_{0.7}\text{La}_{0.3}\text{Al}_{0.65}\text{Ta}_{0.35}\text{O}_3$  (LSAT) Substrat gewachsen. Die Eigenschaften dieser LCMO Lagen wurden verändert indem die Wachstums und Ausglühen Bedingungen variiert wurden. Für alle drei Arten der MLs haben die YBCO Lagen einen verhältnismäßig scharfen supraleitenden (SC) Übergang gezeigt, mit Übergangstemperaturen im Bereich von  $T_C \approx 70\text{-}75\text{ K}$ . Die Curietemperaturen der LCMO Lagen in YL\_1 and YL\_2 sind verhältnismäßig groß mit  $T^{\text{Curie}} = 215$  and  $180\text{ K}$ . Die durchschnittlichen Werte der Tieftemperatur-Magnetisierung liegen zwischen  $2.0$  and  $2.5\ \mu\text{B}$  pro Mn Ion. Außer der vergleichbaren ferromagnetischen Ordnungen zeigen die elektronischen Eigenschaften der LCMO Lagen in YL\_1 and YL\_2 beachtliche Unterschiede. Während in YL\_1 die Ladungsträger in LCMO äußert mobil sind, ist deren Beweglichkeit in YL\_2 durch polaronische Effekte reduziert. Diese Polaronen behalten die ferromagnetische Ordnung bei, aber involvieren eine spezifische Art von orbitaler Ordnung die unterschiedlich zu der in dem mobilen ferromagnetischen Zustand ist. In YL\_3, ist die ferromagnetische Ordnung der Mn Momente stark unterdrückt mit einer durchschnittlichen Magnetisierung von nur  $0.25\ \mu\text{B}$  pro Mn Ion.

Mittels Röntgen Lineardichroismus Untersuchungen (XLD) wurde herausgefunden, dass die angrenzenden Cu Ionen in allen drei Proben einer ähnlichen orbitalen Rekonstruktion unterlaufen. Mit entsprechenden Röntgenstrahlen zirkularen Magnetischen Dichroismus (XMCD) Experimenten wurde weiterhin gezeigt, dass in den drei Arten von Multilagen die ferromagnetischen Cu Momente ähnliche Stärken im Bereich von  $0.11\text{-}0.24\ \mu\text{B}$ . Im Gegensatz zu der Vorhersage des kovalenten Bindung Modells von Ref. [1] wurde herausgefunden, dass die Stärke der AEI mit den Mn Momente für die drei verschiedenen MLs variiert: Sie ist stark in YL\_1, sehr schwach in YL\_2 und vollständig verschwunden in YL\_3. Sehr verblüffend ist der große Unterschied zwischen der AEI-Stärke von YL\_1 und YL\_2, für die die LCMO Lagen stark ferromagnetisch sind. Die Ergebnisse lassen vermuten, dass die Cu Momente nicht durch die AEI mit den Mn Momenten erzeugt werden, sondern eher intrinsisch zu den angrenzenden  $\text{CuO}_2$

Ebenen, für die die Cu Ionen eine orbitale Rekonstruktion unterlaufen. Des Weiteren wurde die starke Unterdrückung der AEI in YL 2 durch die spezifische Art der orbitalen Ordnung der ferromagnetischen Polaronen in den LCMO Lagen erklärt.

Der zweite Teil dieser Arbeit beinhaltet Untersuchungen der Supraleitung und der Ladungsträgerlokalisierung von ultradünnen  $\text{La}_{1.85}\text{Sr}_{0.15}\text{CuO}_4$  (LSCO) Filmen. Die LSCO Filme mit  $\text{La}_2\text{CuO}_4$  (LCO) und LCMO als überdeckende Lagen verschiedener Dicken wurden mittels PLD auf (001)-orientierten  $\text{SrLaAlO}_4$  (SLAO) Substraten gewachsen. Bei den Heterostrukturen die in purem  $\text{N}_2\text{O}$  gas (Wachstumsmodus A) gewachsen wurden, ist die erste LSCO Monolage in der Substratnähe stark ungeordnet. Diese Unordnung konnte substantiell reduziert werden, indem der Film in einer Mischung von  $\text{N}_2\text{O}$  and  $\text{O}_2$  Gas wächst (Wachstumsmodus B). Strukturelle Analysen der Proben bestätigen, dass die LSCO und LCO Lagen fast gänzlich verspannt und die LCMO Lagen zum Teil entspannt sind. Ein einzelner LSCO Film mit einer Dicke von 7 Einheitszellen (u.c.) von der Wachstumsmodus A zeigt einen scharfen supraleitenden Übergang mit einer beginnenden Temperatur  $T_{C,on} \approx 38$  K. Ein einzelner LCMO Film (20 u.c. mit Wachstumsmodus A) besitzt ein  $T^{Curie} \approx 190$  K und eine Tieftemperatur-Magnetisierung von  $2.0 \mu_B$  pro Mn Ion.

Die LSCO(N u.c.)/LCO(2 u.c.) Bilagen (BLs) mit N=2-5, Wachstumsmodus A, sind ebenfalls supraleitend mit einem  $T_{C,on} \approx 30-38$  K. Die Werte für  $T_C$  and  $T_{C,on}$  sind für die entsprechenden LSCO(N u.c.)/LCMO(20 u.c.) BLs reduziert. Dies ist möglicherweise durch die Injektion und/oder Diffusion von spin polarisierten Ladungsträgern entlang der Grenzfläche der ferromagnetischen LCMO in die supraleitenden LSCO Lagen zu erklären. Dieser Effekt ist aufgrund des Ferromagnetismus des LCMO Lage offensichtlich begrenzt auf die erste LSCO Monolage neben der LSCO/LCMO Grenzfläche. Überraschenderweise sind die  $T_C$  Werte viel stärker in den bezüglichen LSCO(N u.c.)/LCO(2 u.c.)/LCMO(20 u.c.) Trilagen (TLs) reduziert. Die TLs für N=2 & 3 zeigen bemerkenswerterweise eine Ladungsträgerlokalisierung bei tiefen Temperaturen. Ähnliche Ladungslokalisationsphänomene sind offensichtlich in einem LSCO(3 u.c.)/LCO(7 u.c.) BL zu finden. Die Magnetismus-Transport Daten weisen darauf hin, dass die Ladungsträger in einem statischen antiferromagnetischen Hintergrund lokalisiert sind. Es ist weiterhin gezeigt, dass die Ladungsträgerlokalisierung reproduzierbar in einem Set von LSCO/LCO BLs mit Wachstumsmodus B sind. Diese systematischen Studien zeigen, dass die Ladungsträgerlokalisierung direkt an der LSCO/LCO Grenzfläche auftreten. Mehrere mögliche Mechanismen werden diskutiert, die zu so einer Art von Ladungsträgerlokalisierung führen könnten.





# Contents

<b>Abstract</b>	<b>iii</b>
<b>1 Introduction</b>	<b>1</b>
<b>2 Properties of individual materials</b>	<b>3</b>
2.1 Cuprate high- $T_C$ superconductors . . . . .	3
2.1.1 $\text{La}_{2-x}\text{Sr}_x\text{CuO}_4$ . . . . .	3
2.1.2 $\text{YBa}_2\text{Cu}_3\text{O}_{7-\delta}$ . . . . .	5
2.2 $\text{La}_{1-x}\text{Ca}_x\text{MnO}_3$ . . . . .	5
2.2.1 Crystal structure . . . . .	7
2.2.2 Electronic and magnetic properties . . . . .	7
<b>3 Experimental techniques</b>	<b>9</b>
3.1 Pulsed laser deposition . . . . .	9
3.1.1 Basic principle of pulsed laser deposition . . . . .	9
3.1.2 Monitoring the film growth . . . . .	11
3.1.3 PLD setup . . . . .	11
3.2 Rutherford backscattering spectrometry . . . . .	12
3.3 Resistance and magnetization measurements . . . . .	13
3.4 Ellipsometry . . . . .	14
3.5 Polarized neutron reflectometry . . . . .	16
3.5.1 Interaction of neutron with matter . . . . .	16
3.5.2 Specular reflectivity . . . . .	17
3.5.3 Impact of roughness on reflectivity profile . . . . .	18
3.5.4 Impact of instrumental resolution on reflectivity profile . . . . .	18
3.5.5 Setting up a PNR experiment . . . . .	19
3.6 X-ray absorption spectroscopy . . . . .	19
3.6.1 Interaction of x-ray on the atomic scale . . . . .	19
3.6.2 X-ray magnetic circular dichroism . . . . .	21
3.6.3 X-ray linear dichroism . . . . .	23
3.6.4 Setting up a XAS experiment . . . . .	25
<b>4 Magnetic proximity effect in YBCO/LCMO multilayers</b>	<b>26</b>
4.1 Growth parameters . . . . .	26
4.2 Structural characterization . . . . .	27
4.3 Scanning transmission electron microscopy . . . . .	29
4.4 Rutherford backscattering . . . . .	29
4.5 Transport and magnetization . . . . .	30
4.6 Optical spectroscopy and ferromagnetic polarons . . . . .	31
4.7 Polarized neutron reflectometry . . . . .	33
4.7.1 Structural depth profile . . . . .	33
4.7.2 Magnetic depth profile . . . . .	35
4.7.3 Summary . . . . .	37
4.8 X-ray absorption spectroscopy . . . . .	37

4.8.1	Experimental details . . . . .	37
4.8.2	X-ray linear dichroism at Cu $L_{3,2}$ -edges . . . . .	39
4.8.3	X-ray linear dichroism at the Mn $L_{3,2}$ -edges . . . . .	41
4.8.4	XMCD at the Cu $L_{3,2}$ -edges . . . . .	43
4.8.5	X-ray magnetic circular dichroism at Mn $L_{3,2}$ -edges . . . . .	46
4.8.6	Summary . . . . .	47
4.9	Discussion and concluding remarks . . . . .	48
<b>5</b>	<b>Superconductivity and charge localization in ultrathin LSCO</b>	<b>51</b>
5.1	Pulsed laser deposition of thin films and heterostructures . . . . .	51
5.1.1	Growth . . . . .	51
5.1.2	Improving the PLD growth of $\text{La}_{2-x}\text{Sr}_x\text{CuO}_4$ . . . . .	53
5.1.3	Summary . . . . .	55
5.2	Structural characterization of the thin films and heterostructures . . . . .	55
5.2.1	Thin films . . . . .	55
5.2.2	Heterostructures . . . . .	55
5.3	Electromagnetic properties of the thin films . . . . .	56
5.3.1	LSCO . . . . .	56
5.3.2	LCO . . . . .	58
5.3.3	LCMO . . . . .	58
5.4	Impact of ferromagnetic LCMO on ultrathin LSCO . . . . .	59
5.4.1	Superconductivity in ultrathin LSCO films . . . . .	59
5.4.2	Suppression of superconductivity in LSCO/LCMO bilayers . . . . .	62
5.5	Transport properties of LSCO/LCO/LCMO trilayers . . . . .	62
5.5.1	Experimental results . . . . .	63
5.5.2	Discussion . . . . .	63
5.6	Origin of the charge carrier localization . . . . .	66
5.6.1	Charge carrier localization in LSCO/LCO bilayers . . . . .	66
5.6.2	Magneto-transport in the hopping regime . . . . .	67
5.6.3	Summary . . . . .	68
5.7	Further studies of charge carrier localization . . . . .	69
5.7.1	Superconductivity in 1 u.c. thick LSCO . . . . .	69
5.7.2	Impact of a thicker LCO layer on superconductivity . . . . .	70
5.7.3	Charge glass state in the LSCO(1 u.c.)-LCO(7 u.c.)-BL* . . . . .	71
5.7.4	Summary . . . . .	72
5.8	Concluding remarks . . . . .	72
<b>6</b>	<b>Conclusions and outlook</b>	<b>74</b>
6.1	Conclusions . . . . .	74
6.2	Outlook . . . . .	75
<b>A</b>	<b>Analysis of the x-ray absorption curves</b>	<b>77</b>
A.1	Background subtraction and normalization of the x-ray absorption spectra . . . . .	77
A.2	Multi-peak fitting to the XAS curves at the $L_3$ -edges . . . . .	77
A.3	Deriving the orbital and effective spin magnetic moment from XMCD in TEY mode . . . . .	80
A.4	Electron polarization of the Mn $e_g$ -orbitals . . . . .	81
<b>B</b>	<b>Electron polarization of <math>e_g</math>-orbitals in a FM polaron</b>	<b>82</b>
<b>C</b>	<b>Origin of the Cu moment at the interfacial <math>\text{CuO}_2</math> planes</b>	<b>83</b>
<b>D</b>	<b>Variable range hopping model</b>	<b>85</b>
<b>E</b>	<b>MATLAB code to measure V-I characteristics with Keithley</b>	<b>86</b>

---

<b>F</b>	<b>The R-T curves of a LCO(2 u.c.)-LCMO(20 u.c.)-BL</b>	<b>87</b>
<b>G</b>	<b>Hopping conduction in the LSCO(3 u.c.)-LCO(7 u.c.)-BL</b>	<b>88</b>
<b>H</b>	<b>Hopping conduction in the LCO(1 u.c.)-LCO(7 u.c.)-BL*</b>	<b>89</b>
<b>I</b>	<b>7 u.c. thick <math>\text{La}_{1.94}\text{Sr}_{0.06}\text{CuO}_4</math> capping on 2 u.c. thick LSCO</b>	<b>90</b>
	<b>Acknowledgement</b>	<b>91</b>
	<b>Curriculum Vitae</b>	<b>93</b>
	<b>Bibliography</b>	<b>95</b>



# Chapter 1

## Introduction

Superconductivity (SC) is based on so-called ‘Cooper pairs’ that consist of two electrons with opposite spin and momentum [6]. To the contrary, the ferromagnetic (FM) order parameter arises from an exchange interaction between two electrons with the same spin orientation [7]. The SC and FM orders therefore involve antagonistic spin correlations which makes it difficult to realize both of them simultaneously in a homogeneous material. On the other hand, in the cuprate and the Fe-based high- $T_C$  superconductors it has been shown that the SC order parameter can readily coexist and compete with an antiferromagnetic (AF) order [8–10]. Accordingly, since the discovery of the high- $T_C$  superconductors, the interplay between the superconducting and magnetic order parameters has become a very active and fascinating topic of condensed matter physics.

SC/FM heterostructures are the ideal candidates to study the interplay between the SC and FM order parameters whose relative strengths can be controlled via their thickness ratio. In heterostructures, comprising conventional superconductors and elemental or alloy ferromagnets, the competing interaction leads to several phenomena, such as domain wall SC [11], an oscillatory behavior of the SC transition temperature ( $T_C$ ) as a function of the thickness of the FM layer [12], and a long-range proximity effect for which the spin-triplet SC state is a prerequisite [13]. Experimental studies on oxide-based SC/FM heterostructures found a reduction of the  $T_C$  value as a function of the thickness of the FM layer [14], an enhancement of  $T_C$  in response to an applied magnetic field [15], a giant magneto-resistance [16], etc.

Unlike SC/FM heterostructures, the proximity effect in SC/AF type heterostructures is largely unexplored. This is because the AF alignment of the electron spins does not generate a net internal field which can break the ‘Cooper pairs’. However, it was theoretically shown that the nesting features of the Fermi surfaces of so-called band antiferromagnets destroy the symmetry in momentum space, and thus can strongly suppress superconductivity [17]. The strongest  $T_C$  suppression has been reported for heterostructures that are made from conventional SCs and AF alloys [18]. The experiments on corresponding oxide-based SC/AF heterostructures showed a reduction of  $T_C$  with increasing thickness of a  $C$ -type AF layer [19], and found evidences which suggest that these two order parameters do not mix [20].

A prominent example in the class of SC/FM heterostructures involves the so-called magnetic proximity effect (MPE) at the interface between high- $T_C$  superconductor  $\text{YBa}_2\text{Cu}_3\text{O}_7$  (YBCO) and ferromagnet  $\text{La}_{2/3}\text{Ca}_{1/3}\text{MnO}_3$  (LCMO) [1, 3, 14, 16, 21–28]. With polarized neutron reflectometry (PNR) it was found that, in the vicinity of the interface, the FM order of the Mn moments is strongly suppressed [3, 22, 23, 29]. This phenomenon has been discussed in terms of a ‘*dead layer*’ or a ‘*depleted layer*’. In addition, it was shown with x-ray magnetic circular dichroism (XMCD) that the interfacial Cu ions acquire a FM moment of about  $0.2 \mu_B$  which is antiparallel to the one of Mn [1–4]. Recent x-ray resonant magnetic reflectometry (XRMR) studies have demonstrated that these Cu moments reside in the interfacial  $\text{CuO}_2$  planes [30]. Furthermore, x-ray linear dichroism (XLD) studies revealed that the interfacial Cu ions undergo an orbital reconstruction which gives rise to a strong enhancement of the hole density in the Cu  $3d_{3z^2-r^2}$  orbitals, which in the bulk are almost fully occupied [4, 5]. Both the

orbital reconstruction and the magnetic moment of the interfacial Cu ions have been explained in terms of a strong hybridization between the Cu and Mn  $3d_{3z^2-r^2}$  orbitals which leads to an AF exchange interaction (AEI) between the Cu and Mn spins [5]. In this context, the ferromagnetic Cu moment is induced by the AEI with the Mn moments, and one expects that the magnitude of this Cu moment is proportional to the strength of this coupling [1, 31, 32].

The long-range AF order in  $\text{La}_2\text{CuO}_4$  is rapidly destroyed, and the SC state slowly emerges upon hole doping. At the intermediate doping, a heterogeneous state of hole-poor AF and hole-rich SC domains arises. These characteristics indicate a correlation between the AF and SC order parameters [33]. Previous experiments on  $\text{La}_{1.85}\text{Sr}_{0.15}\text{CuO}_4/\text{La}_2\text{CuO}_4/\text{La}_{1.85}\text{Sr}_{0.15}\text{CuO}_4$  (LSCO/LCO/LSCO) trilayers have indicated that a single monolayer of LCO which has a strong AF fluctuations [34], is sufficient to block a supercurrent between two neighboring LSCO layers. This suggests that the AF and SC order parameters do not mix over an extended length scale, i.e., the proximity effect between these SC and AF orders must be very weak [20]. However, a systematic study on LSCO/LCO bilayers by varying the thicknesses of the individual layers is still lacking, which in principle allows one to investigate the interplay between these competing orders.

**The first topic of this thesis** is to investigate how the strength of the AEI between the interfacial Cu and Mn ions in YBCO/LCMO heterostructures depends on the electronic and magnetic properties of the LCMO layers. The goal has been achieved by altering the growth and annealing conditions, as well as the thickness of the LCMO layers. The depth profile of the sample magnetization has been obtained from PNR experiments. The magnetism and orbital occupancies of the Cu and Mn ions have been studied with the XMCD and XLD techniques. The systematic studies show that the magnitude of the FM Cu moment does not depend on the strength of the AEI coupling. This suggests that the Cu moment is intrinsic to the interfacial  $\text{CuO}_2$  planes and subject to a weakly FM Cu-Cu exchange interaction that arises from the orbital reconstruction of the interfacial Cu ions.

**The second topic of this thesis** concerns the study of superconductivity and the charge carrier localization in ultrathin LSCO films. For this purpose, the LSCO films with LCO and LCMO capping layers of various thicknesses have been grown using pulsed laser deposition. The structural characterization of the samples has been performed with reflection high energy electron diffraction and x-ray diffraction techniques. The transport properties of the samples have been obtained by means of the conventional four-probe resistance and magneto-resistance measurements. The systematic study reveals a stronger suppression of SC in the LSCO/LCO bilayers than in the LSCO/LCMO counterparts. Moreover, the charge carriers in the LSCO/LCO bilayers have a strong tendency to become localized at low temperature. Several possible explanations for these differences between the LSCO/LCMO and LSCO/LCO bilayer systems are discussed.

The thesis is structured as follows. The bulk properties of the individual materials which are used in this thesis are briefly summarized in Chapter 2. The basics of the experimental techniques are reviewed in Chapter 3. Chapter 4 is concerned with the MPE in YBCO/LCMO multilayers and its changes as a function of the electronic and magnetic properties of the LCMO layers. The subject of Chapter 5 is the superconducting and electric transport properties of bilayers and trilayers that consist of ultrathin layers of LSCO with top layers of LCMO and/or LCO. Finally, the conclusions and the outlook of this thesis are given in Chapter 6.

# Chapter 2

## Properties of individual materials

In this chapter, we discuss the structural, electronic and magnetic properties of the high- $T_C$  cuprate and manganite systems. Thin films and heterostructures of these materials were investigated in this thesis. The properties of  $\text{La}_{2-x}\text{Sr}_x\text{CuO}_4$  and  $\text{YBa}_2\text{Cu}_3\text{O}_{7-\delta}$ , which belong to the high- $T_C$  cuprate family, are discussed in section 2.1. The physical properties of the manganite system  $\text{La}_{1-x}\text{Ca}_x\text{MnO}_3$  are summarized in section 2.2.

### 2.1 Cuprate high- $T_C$ superconductors

In September 1986, Bednorz and Müller discovered superconductivity in the La-Ba-Cu-O compound with a superconducting critical temperature ( $T_C$ ) of above 30 K [35]. This discovery earned them the Nobel prize in 1987. Soon after, J. M. Tarascon *et al.* reported the evidence of superconductivity in the La-Sr-Cu-O compound with an even higher  $T_C$  of 40 K [36]. It was later found that the  $T_C$  of  $\text{La}_{2-x}\text{Sr}_x\text{CuO}_4$  strongly depends on the Sr doping [37]. C. W. Chu *et al.* reported that the  $T_C$  of La-Ba-Cu-O can be increased to 52 K by applying an external pressure. As a next step to induce chemical pressure, M. K. Wu *et al.* replaced the La with the isovalent Y of smaller ionic radii, and found superconductivity with a  $T_C$  of 93 K [38]. The superconducting phase in this Y-Ba-Cu-O compound was later identified as  $\text{YBa}_2\text{Cu}_3\text{O}_{7-\delta}$  [39]. In the following, we discuss the structural, electronic and magnetic properties of the  $\text{La}_{2-x}\text{Sr}_x\text{CuO}_4$  and  $\text{YBa}_2\text{Cu}_3\text{O}_{7-\delta}$  compounds.

#### 2.1.1 $\text{La}_{2-x}\text{Sr}_x\text{CuO}_4$

##### Crystal structure

Undoped  $\text{La}_{2-x}\text{Sr}_x\text{CuO}_4$ , i.e.,  $\text{La}_2\text{CuO}_4$  (LCO) is tetragonal at high temperature (HTT) with a space group of  $I4/mmm$ . It undergoes a structural phase transition below 550 K into a low temperature orthorhombic (LTO) phase with a space group of  $Bmab$ . For optimal doping (Sr= 0.15), the transition temperature decreases to 200 K, as reported in Ref. [40]. Figure 2.1a shows a crystallographic unit cell of LCO in the HTT phase with lattice parameters of  $a=b=3.8006 \text{ \AA}$  and  $c=13.1172 \text{ \AA}$ . The consecutive  $\text{CuO}_2$  planes in the unit cell are separated by two LaO planes. The crystallographic unit cell in the LTO phase with lattice parameters of  $a=5.3568 \text{ \AA}$ ,  $b=5.4058 \text{ \AA}$  and  $c=13.1432 \text{ \AA}$  is depicted in Figure 2.1b. In the LTO phase, the  $\text{CuO}_6$  octahedra undergo small tilts which give rise to a buckling of the  $\text{CuO}_2$  planes.

##### Electronic and magnetic properties

The Cu ions of  $\text{La}_{2-x}\text{Sr}_x\text{CuO}_4$  are in the +2 oxidation state. Thus, they have an electron configuration of  $3d^9$  for which one hole in the  $e_g$ -orbitals. The tetragonal Jahn-Teller (JT) distortion of the  $\text{CuO}_6$  octahedra, with a larger Cu-O bond length along the  $c$ -axis as compared to the one along  $ab$ -plane, increases the relative energy of the  $3d_{x^2-y^2}$  orbitals over the one of the  $3d_{3z^2-r^2}$  orbitals. Consequently, the holes predominantly occupy the  $3d_{x^2-y^2}$

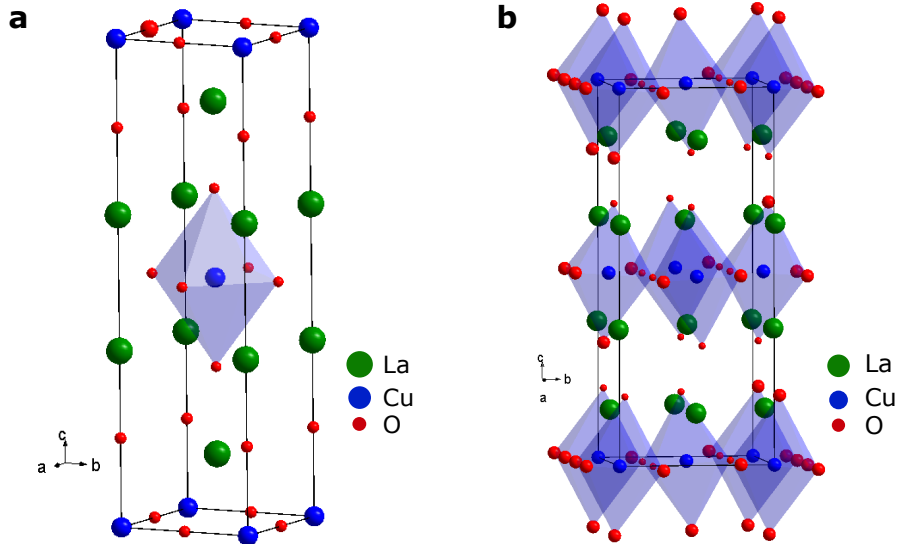


Figure 2.1: (a)  $\text{La}_2\text{CuO}_4$  unit cell in the high-temperature tetragonal phase with a space group of  $I4/mmm$ . (b)  $\text{La}_2\text{CuO}_4$  unit cell in the low-temperature orthorhombic phase with a space group of  $Bmab$ . The unit cell parameters, and the coordinate positions of the atoms in the LTO phase are taken from Ref. [41]. The tilts of the  $\text{CuO}_6$  octahedra are indicated.

orbitals, as shown in Figure 2.2a. The hopping of the electrons between the neighboring Cu sites via the  $\text{O-}2p_\sigma$  orbitals gives rise to a strong superexchange interaction which leads to the antiferromagnetic (AF) exchange coupling of the Cu ions along the  $ab$ -plane. The strength of the in-plane Cu-Cu AF coupling amounts to about  $J_{AF} \approx 135$  meV. The corresponding interplanar coupling is very weak [42]. For that reason, the three-dimensional (3D) AF order develops only below 325 K [43]. In the LTO phase, the buckling of the  $\text{CuO}_2$  planes instigates a Dzyaloshinskii-Moriya interaction between the neighboring antiparallel Cu spins. This interaction results in a small out-of-plane spin canting and a corresponding ferromagnetic moment.

The insulating behavior of LCO, with the holes in its  $e_g$ -orbitals, is the result of a strong on-site Coulomb repulsion ( $U$ ) of the electrons. According to the Mott-Hubbard model, a large  $U$  of 6-10 eV [44] splits the  $e_g$ -orbitals into an unoccupied upper Hubbard band (UHB) and an occupied lower Hubbard band (LHB), as shown in Figure 2.2b. The fully occupied energy band due to the  $\text{O-}2p_\sigma$  orbitals resides within this so-called Mott-Hubbard gap due to the  $\text{Cu-}3d_{x^2-y^2}$  levels, and is located just below the UHB. This situation corresponds to a so-called ‘charge transfer insulator’ [45] with a charge transfer gap ( $\Delta$ ) of about 1-3 eV [44].

The substitution of trivalent La-ions with divalent Sr-ions introduces holes which reportedly predominantly populate the  $\text{O-}2p_\sigma$  band [46]. These doped holes form so-called Zhang-Rice singlet (ZRS) states which also involve the  $3d_{x^2-y^2}$  orbitals of the neighboring Cu ions. According to the phase diagram, shown in Figure 2.3, a small number of holes with  $x > 0.02$  already destroys the long-range AF order. A short-range AF order still persists up to  $x < 0.05$ . The Cu spins for the doping of  $0.02 < x < 0.05$  undergo a glass transition at low temperature. This is known as a so-called spin glass (SG) state which exists up to  $x = 0.12$  [47]. The superconductivity appears only at  $x > 0.05$ , and persists up to a doping level of  $x \leq 0.275$ . The maximum  $T_C$  occurs at  $x = 0.15$  which corresponds to the optimum doping level. The interplay between the AF and the superconducting phases is considered as an indication that the mechanism of superconductivity in these cuprates is closely related to the magnetic correlations in the  $\text{CuO}_2$  planes [48]. An interesting feature on the underdoped side of the phase diagram is the pseudogap (PG) state which is characterized by the partial suppression of the low energy charge and spin excitations [49]. The normal state of  $\text{La}_{2-x}\text{Sr}_x\text{CuO}_4$  is known as ‘strange metal’ (SM) phase whose conduction property is very different from the one of a

conventional metal which follows Landau Fermi-liquid (FL) theory. According to FL theory:  $\rho \propto T^2$ , where  $\rho$  and  $T$  represent resistivity and temperature, respectively. For the optimally doped  $\text{La}_{2-x}\text{Sr}_x\text{CuO}_4$ , the normal state in-plane resistivity ( $\rho_{ab}$ ) has a linear temperature dependence. The overdoped  $\text{La}_{2-x}\text{Sr}_x\text{CuO}_4$  follows the FL theory in its normal state. The metallic conductivity in this cuprate is highly anisotropic; the in-plane conductivity shows a metallic behavior, whereas the out-of-plane conductivity displays an insulating trend up to  $x \leq 0.19$  [50].

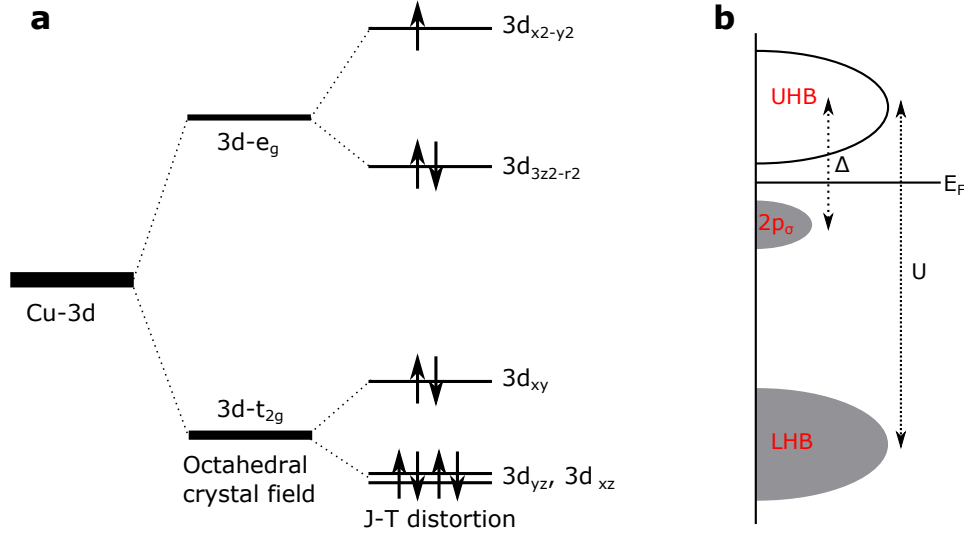


Figure 2.2: (a) For an insulated  $\text{Cu}^{2+}$  ion, the  $3d$ -orbitals are degenerate. In an octahedral crystal environment, the  $3d$ -orbitals split into  $t_{2g}$  and  $e_g$  levels. The tetragonal distortion in the octahedral crystal field environment, with a larger Cu-O bond length along  $c$ -axis compared to the one along  $ab$ -plane, splits the  $e_g$ -orbitals and brings the  $3d_{3z^2-r^2}$  orbital down in energy. (b) A band diagram for LCO, a charge transfer insulator, with the occupied O- $2p_{\sigma}$  band below the Fermi level ( $E_F$ ). At large  $U (> \Delta)$ , the  $3d$ -orbitals are divided into an occupied lower Hubbard band (UHB) and an unoccupied upper Hubbard band (UHB).

### 2.1.2 $\text{YBa}_2\text{Cu}_3\text{O}_{7-\delta}$

Figure 2.4 shows the crystallographic unit cell of  $\text{YBa}_2\text{Cu}_3\text{O}_{7-\delta}$  (YBCO) at  $\delta$  equals to zero. In this fully oxygenated state, the unit cell is orthorhombic with lattice parameters of  $a = 3.8206 \text{ \AA}$ ,  $b = 3.8851 \text{ \AA}$  and  $c = 11.6757 \text{ \AA}$  [51]. The  $\text{CuO}_2$  planes in the unit cell are oriented perpendicular to the  $c$ -axis, and the  $\text{CuO}$  chain layers are parallel to  $b$ -axis. In two consecutive unit cells, the  $\text{CuO}_2$  planes are separated by a  $\text{CuO}$  chain layer. It is generally agreed that the superconductivity takes place in the  $\text{CuO}_2$  planes, and the  $\text{CuO}$  chains serve as charge reservoir which determines the carrier density in the planes. In an oxygen deficient YBCO ( $\delta > 0$ ), electrons from the chain layers are transferred to the  $\text{CuO}_2$  planes, and thus the hole density is reduced. Hence, the oxygen content controls the electronic and magnetic properties of the system. The accessible phase diagram for YBCO with the variation of  $\delta$  is indicated by a red arrow in Figure 2.3. It is well known that the electronic and magnetic properties of the cuprate systems have similar hole dependencies.

## 2.2 $\text{La}_{1-x}\text{Ca}_x\text{MnO}_3$

The compound  $\text{La}_{1-x}\text{Ca}_x\text{MnO}_3$  (LCMO) belongs to the manganite family with the general formula  $\text{RE}_{1-x}\text{AE}_x\text{MnO}_3$ , where RE and AE stand for a trivalent rare earth and a divalent alkaline earth ions, respectively [52]. The manganites have been extensively studied in the past owing to their enriched physics arising from the interplay between the spin, charge and orbital degrees of freedom. In the parent compound of LCMO with  $x = 0$ , the Mn ions are

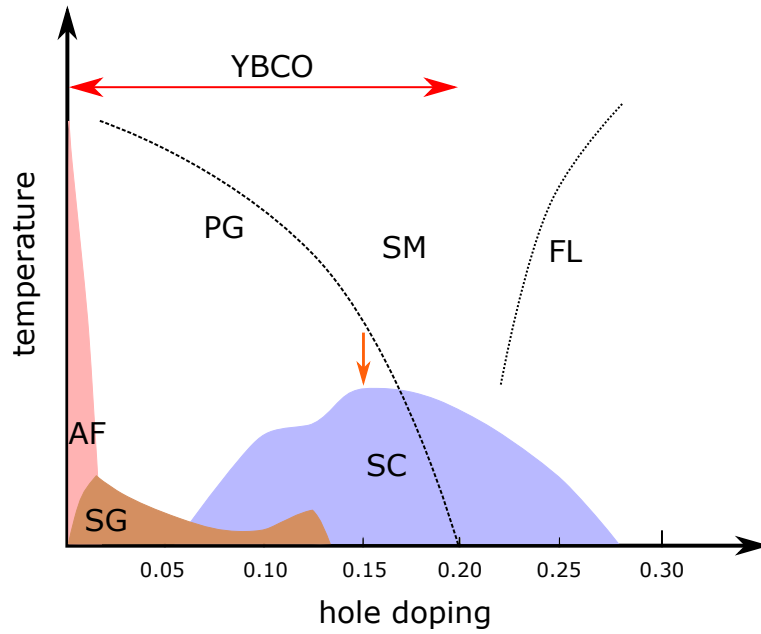


Figure 2.3: Universal phase diagram of the high- $T_C$  cuprate family. The red arrow marks the range of the phase diagram that is accessible with  $\text{YBa}_2\text{Cu}_3\text{O}_{7-\delta}$ . AF: 3D antiferromagnetic phase. SG: Spin glass phase. PG: Pseudogap phase. SC: Superconducting phase. SM: Strange metal phase. FL: Fermi-liquid phase.

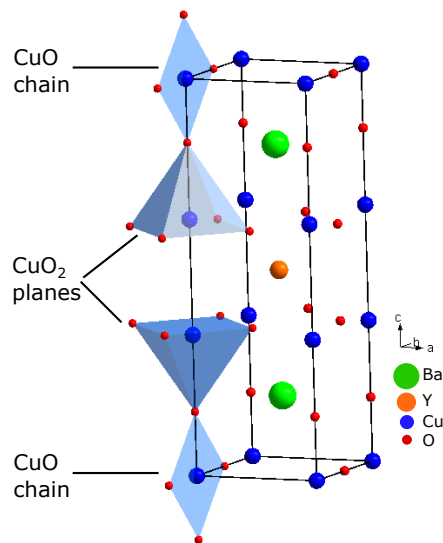


Figure 2.4: A sketch of the orthorhombic unit cell of  $\text{YBa}_2\text{Cu}_3\text{O}_7$  illustrating adjacent  $\text{CuO}_2$  planes and  $\text{CuO}$  chains.

in a +3 oxidation state, and thus have four electrons in the  $3d$ -orbital. The substitution of trivalent La ions with the divalent Ca ions introduces holes at the Mn site which result in a corresponding fraction of  $\text{Mn}^{4+}$  ions. In the following, we discuss the structural, electronic and magnetic properties of the mixed valence LCMO compound.

### 2.2.1 Crystal structure

Figure 2.5 displays the orthorhombic LCMO unit cell with the space group of  $Pbnm$ . For the doping of  $x = 0.33$ , the resulting lattice parameters are  $a = 5.4717 \text{ \AA}$ ,  $b = 5.4569 \text{ \AA}$  and  $c = 7.7112 \text{ \AA}$  [53]. The rotation and distortion of the  $\text{MnO}_6$  octahedra in the unit cell are inherent structural properties of this manganite system. In this thesis, the pseudocubic lattice notation is used, and the pseudocubic lattice parameter ( $a_{pc}$ ) is deduced following the formula:  $a_{pc} \approx \frac{\sqrt{a^2+b^2}}{2} \approx \frac{c}{2}$ .

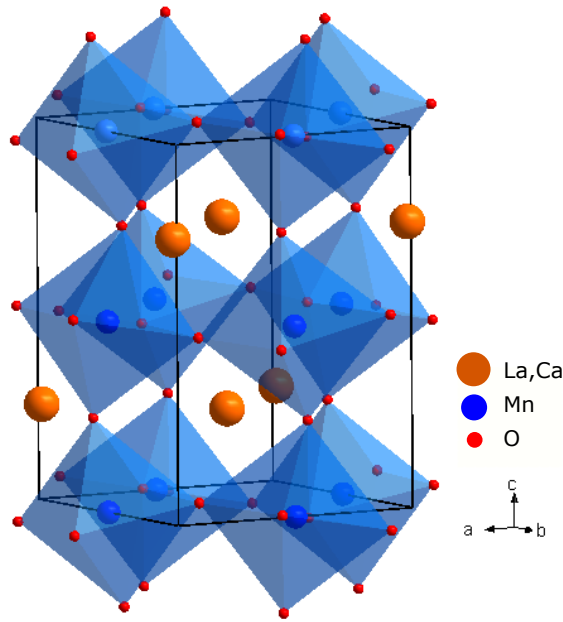


Figure 2.5: Sketch of the orthorhombic unit cell of  $\text{La}_{2/3}\text{Ca}_{1/3}\text{MnO}_3$  illustrating the tilts and rotations of the  $\text{MnO}_6$  octahedra.

### 2.2.2 Electronic and magnetic properties

The  $\text{Mn}^{3+}$  ions of the parent compound  $\text{LaMnO}_3$  (LMO) are Jahn-Teller (J-T) active since one electron per ion reside in the  $e_g$ -level. The resulting J-T distortions of  $\text{MnO}_6$  octahedra, together with the large on-site Coulomb repulsion hinder the electron hopping between two Mn sites. As a result, the undoped LMO behaves like an insulator. In this insulating phase, the orbital order associated with the J-T distortions leads to an  $A$ -type antiferromagnetic order with a Néel temperature of about 140 K [54].

A dramatical change in the electronic and magnetic properties of LMO takes place upon Ca doping which introduces  $\text{Mn}^{4+}$  ions with empty  $e_g$ -orbitals. This enables a minimization of the electronic kinetic energy happens via the hopping of  $\text{Mn}^{3+}-e_g$  electrons between  $\text{Mn}^{3+}$  and  $\text{Mn}^{4+}$  sites, given a ferromagnetic order of the spins of electrons in the  $t_{2g}$  levels. This leads to a ferromagnetic exchange interaction which is commonly known as the double exchange interaction (DE-I). Local Hund's coupling aligns the  $t_{2g}$  and  $e_g$  electrons in the same direction. Therefore, the delocalization of the fully spin-polarized  $\text{Mn}^{3+}-e_g$  electrons will be maximum if the neighboring  $\text{Mn}^{3+}$  and  $\text{Mn}^{4+}$  ions are ferromagnetically aligned, as schematically shown in Figure 2.6a. Hence, the DE-I favors the metallic and ferromagnetic state of the system, whereas the J-T distortions suppress the mobility of electrons and favors an antiferromagnetic

order. The DE-I strongly depends on the Mn-O bond length and the Mn-O-Mn bond angle which are directly linked to the doping concentration and the J-T distortions. Upon doping, the competition between the DE-I and the J-T distortions leads a rich phase diagram of LCMO, as shown in Figure 2.6b.

The DE-I is prominent for the doping of  $0.175 < x < 0.5$ . In this regime, the system behaves like a paramagnetic insulator above  $T^{Curie}$ . This is because the hopping probability of electrons is minimal in the presence of randomly oriented spins. Below  $T^{Curie}$ , when the system becomes ferromagnetic, the electrons delocalize over larger length scale, and an insulator-to-metal transition occurs. Near  $T^{Curie}$ , the application of an external magnetic field helps to aligning the spins of the  $t_{2g}$  electrons, and thereby increases the itinerancy of the  $e_g$  electrons. This effect is known as ‘colossal magneto-resistance’.

In this thesis, we used  $\text{La}_{2/3}\text{Ca}_{1/3}\text{MnO}_3$  which is almost in the middle of the ferromagnetic-metallic (FM) phase in the phase diagram as marked by a red arrow in Figure 2.6b. It is worth discussing the impact of oxygen deficiency on the electronic and magnetic properties of  $\text{La}_{2/3}\text{Ca}_{1/3}\text{MnO}_{3-\delta}$ . The oxygen deficiency reduces the hole content in the system, which in return suppresses the conductivity. Such a reduction of conductivity does not necessarily correspond to a suppression of ferromagnetic order. This is because the charge carriers may localize in the form of orbital polarons order for which the local DE-I still promotes ferromagnetic ordering [55, 56].

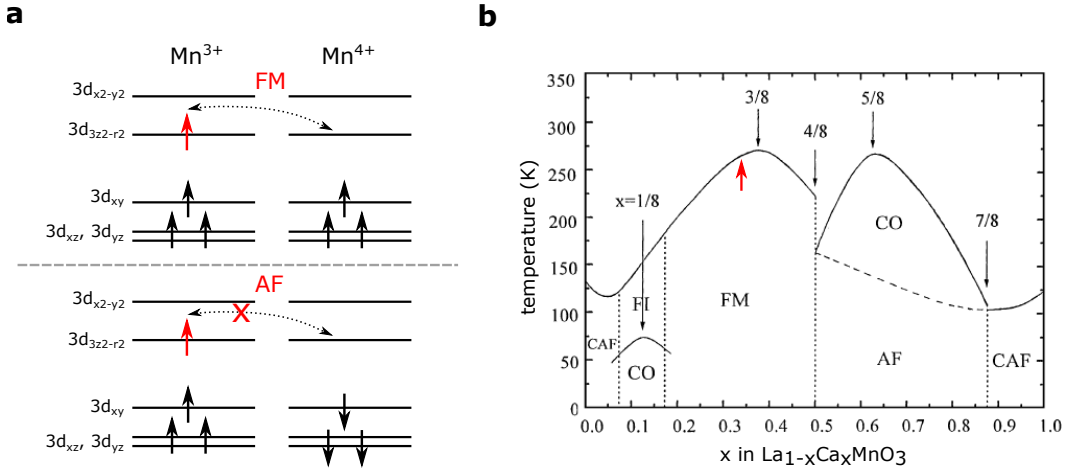


Figure 2.6: (a) A sketch explaining the double exchange interaction. The on-site Hund’s coupling aligns the spin of the  $t_{2g}$  and  $e_g$  electrons in the same direction. In case of ferromagnetic (FM) alignment between the  $\text{Mn}^{3+}$  and  $\text{Mn}^{4+}$  ions, the Hund’s coupling at the  $\text{Mn}^{4+}$  site allows the hopping of the  $\text{Mn}^{3+}$ - $e_g$  electron. When the ions are antiferromagnetically (AF) coupled, the Hund’s rule does not allow the electron hopping. (b) Phase diagram of  $\text{La}_{1-x}\text{Ca}_x\text{MnO}_3$ , as taken from Ref. [57]. Depending on doping level, the system develops several ground states of canted antiferromagnet (CAF), ferromagnetic-insulator (FI), ferromagnetic-metallic (FM) and antiferromagnet (AF). In addition, the system exhibits charge order (CO) in a certain doping regime. The red arrow marks the phase of  $\text{La}_{2/3}\text{Ca}_{1/3}\text{MnO}_3$  which is subject of this thesis.

## Chapter 3

# Experimental techniques

This chapter is dedicated to reviewing the basics of the experimental techniques which were extensively used in this thesis. The underlying concepts of the pulsed laser deposition technique are discussed in section 3.1. The principle of Rutherford backscattering spectrometry is reviewed in section 3.2. A brief on transport and magnetization measurements is given in section 3.3. Measurements of the optical conductivity with the spectroscopic ellipsometry technique are discussed in section 3.4. The concept of polarized neutron reflectometry experiment is summarized in section 3.5. Descriptions of the x-ray magnetic circular dichroism and x-ray linear dichroism techniques are given in section 3.6.

### 3.1 Pulsed laser deposition

The thin films and heterostructures, which are studied in this thesis, were grown by pulsed laser deposition (PLD). The PLD growth of epitaxial thin films involves the evaporation of a solid state materials with a highly intense short-time laser pulse. One of the main advantages of this technique is the stoichiometric material transfer from the target to the film, which allows a wide variety of materials to be grown. A small laser spot size of about  $3.1 \text{ mm}^2$  permits the use of a small target and a fast growth rate. The major disadvantage concerns the limited surface area over which a homogeneous growth can be achieved. This is important for the neutron reflectometry and the ellipsometry experiments which require films with a rather larger surface area. In the following, we review the basic principle of the PLD technique, the real-time monitoring of the film growth and the required components of a basic PLD system.

#### 3.1.1 Basic principle of pulsed laser deposition

The physical process, from the laser-assisted material vaporization to the growth of a stoichiometric film, is very complex in nature and is also largely unexplored. To understand the basic principle, the growth of a thin film is divided into three steps: (a) laser-target interaction, (b) propagation of a plasma plume towards a hot substrate surface, and (c) the deposition of ablated material on the hot substrate.

##### (a) Laser-target interaction

When a target material is exposed to laser radiation, the photons get absorbed by the material within a characteristic length which is known as the optical absorption depth,  $l_{op}$ . The wavelength of the laser and the conducting properties of the target material determine the  $l_{op}$ . Within a few femtoseconds after the photon absorption, the electrons get excited and form a high density of plasmons, excitons, and free electrons. Due to the strong electron-phonon coupling in the solid, the energy of the electronic excitations is transferred to the lattice within a few picoseconds. This leads to an intense heating of the target within the  $l_{op}$  above the melting point, and thus the start of the evaporation of the material. In this context, the thermal diffusion length,  $l_{th}$ , of the target material comes into play. It depends on the

laser pulse duration,  $\tau$ , and the thermal diffusion constant of the material,  $D$ , according to  $l_{th} = \sqrt{D\tau}$ . Congruent absorption and thereby the stoichiometric removal of the target material occurs when the condition of  $l_{op} \gg l_{th}$  is satisfied. In this case only a small fraction (on the order of  $\mu\text{J}$ ) of the total pulse energy (on the order of  $\text{mJ}$ ) is dissipated in evaporating the target material. The rest ionizes the newly developed evaporated layer, and forms a plasma plume that contains highly energetic ions, neutral atoms, and free electrons. The laser pulse duration, fluence and repetition rate are the key parameters that control the composition and kinetics of this plasma.

### (b) Propagation of the plasma plume

As the ions in the plasma plume suffer from Coulomb repulsion, the plume rapidly expands and it starts to move away from the target surface due to recoil effects. The kinetic energy of the plasma species can vary from about 1 to 500 eV. For the deposition of a good quality thin film, it should be in the range of 5-50 eV. Otherwise, the sputtering of high energetic particles gives rise to the defects in the deposited film. The kinetic energy of the plume as it reaches to the substrate surface can be controlled via the laser fluence, the repetition rate, the background gas pressure and the target-to-substrate distance. Since the laser fluence has to remain high to ablate material, the rest of the parameters play key roles in this process. Another relevant parameter is the angular spread of the plume near to the substrate surface; that determines the maximal area over which a homogeneous and stoichiometric film growth is possible. The laser spot size, the background gas pressure and the target to the substrate distance determine the angular spread of the plume.

### (c) Deposition of film

A hot substrate is typically placed with its surface normal along the direction of the plume propagation. The energetic plasma species are adsorbed as they reach to the substrate surface. These are thermodynamically unstable at the beginning, but eventually they develop chemical bonds with each other. This leads to the growth of a film which has almost the same composition as the target material. As the growth process occurs from a state which is not in thermodynamic equilibrium, it is sensitive to several factors, like the kinetic energy of the plasma species, the instantaneous deposition rate, the substrate temperature and the mobility of the adatoms on the substrate surface. The mobility of the adatoms on the substrate surface largely depends on its temperature, roughness, chemical composition and crystallographic orientation. The crystallographic orientation of the substrate also gives rise to the preferential crystallographic orientation of the film. In the following, we discuss several growth modes that concern the depositions of complex oxides.

**Frank-van der Merwe growth mode.** In this mode, as shown in Figure 3.1a, a monolayer first covers the substrate surface, and the second monolayer forms only upon the completion of the first one. This requires a stronger bonding between the substrate and the adatoms than the bonding between the adatoms. Such a *layer-by-layer* growth mode generally occurs when the in-plane lattice parameters of the target material and the substrate are very similar. In this mode, one can control the film thickness with sub-unit-cell resolution.

**Volmer-Weber growth mode.** The Volmer-Weber or the three-dimensional (3D) growth mode is typically a result of stronger adhesion between the adatoms than their bonding with the substrate. This gives rise to the nucleation of small clusters which grow in the vertical direction and form 3D islands, as shown in Figure 3.1b. Typically, a large lattice mismatch between the substrate and the film influences the film growth in this direction. A wrong choice of PLD growth parameters, such as very high or low substrate temperature, high background gas pressure and rapid deposition promotes this type of growth. For deposition of a good superlattice, one should avoid this growth mode.

**Stranski-Krastanov growth mode.** In this growth mode, a combination of *layer-by-layer* and 3D islands growths dominates the deposition, as displayed in Figure 3.1c. The film

starts to grow in a *layer-by-layer* fashion, but as the film thickness increases, 3D islands begin to form. A film deposited in this mode appears to have discrete 3D islands on top of a 2D flat film surface.

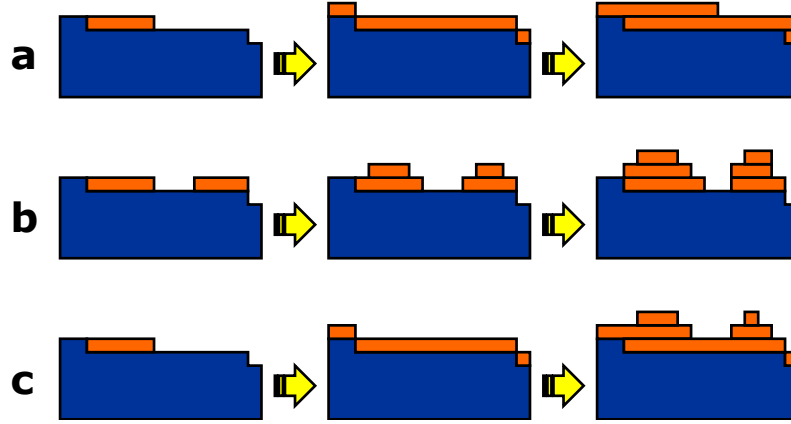


Figure 3.1: A schematic representation of the different PLD growth modes. (a) Frank-van der Merwe growth, (b) Volmer-Weber growth and (c) Stranski-Krastanov growth. The image is taken from Ref. [58].

### 3.1.2 Monitoring the film growth

The real-time PLD growth of a film can be monitored with the *in-situ* reflection high energy electron diffraction (RHEED) technique. A collimated monochromatic electron beam (with a kinetic energy of 30 keV) illuminates the substrate or film surface at a grazing incidence, and the diffracted beam falls on a phosphorus screen as shown in Figure 3.2a. Due to the grazing incidence, the RHEED signal is very sensitive to the surface morphology of the substrate or film. The reciprocal lattice space of a 2D lattice consists of periodic lattice rods which are elongated along the surface normal. These lattice rods intersect with the Ewald sphere in reciprocal space, and thus satisfy the condition of constructive interference. As a result, the phosphorus screen shows a set of diffraction maxima which lay on a semicircular ring, known as the ‘Laue ring’. The spacing between these spots is inversely proportional to the in-plane lattice constant. If the surface is ideally 2D, the diffraction spots are points-like. However, in reality, a film surface is disordered and contains defects. Consequently, the diffraction spots are vertically (in the direction of the surface normal) elongated and broadened in the horizontal direction.

During the deposition of a film, one can use the RHEED technique to continuously track the surface morphology, and obtain the growth rate. In the *layer-by-layer* growth mode, the intensity of 0-th order Bragg reflex exhibits oscillations with time. The RHEED intensity is inversely proportional to the number of step-edges which form during the deposition. The maximum intensity is obtained when the number of step-edges is minimal, i.e., when a layer is completed. The reverse holds for the half completed layer. Hence, one can control the thickness of a film with the resolution of a sub-unit-cell.

### 3.1.3 PLD setup

Figure 3.2b displays a schematic diagram of a PLD setup with *in-situ* RHEED option. For the deposition of films and heterostructures, we used a custom built PLD chamber which was designed by SURFACE GmbH [60]. It is equipped with an excimer laser which produces laser pulses with a duration of 25 ns. The wavelength of the laser is 248 nm, and its energy can be varied in the range of 100-800 mJ. A rectangular mask is used to select a homogeneous part of the laser beam. The selected laser beam is then guided through an optical assembly

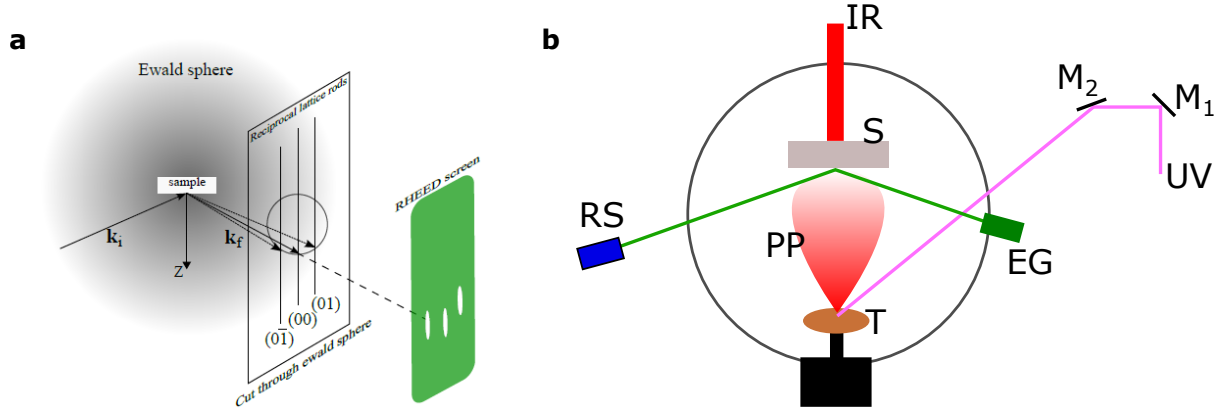


Figure 3.2: (a) An Ewald sphere construction illustrating a set of RHEED diffraction maxima for a two dimensional lattice. In reciprocal space a two dimensional lattice transforms into a set of infinite lattice rods which are aligned in the direction perpendicular to the sample surface. The image is taken from Ref. [59]. (b) A schematic diagram describing a basic pulsed laser deposition setup. UV: An ultraviolet laser beam for ablating the target.  $M_1$ ,  $M_2$ : a set of mirrors guiding the UV laser beam to the target. T: a target. PP: a plasma plume. S: a hot substrate. IR: an infrared laser beam is heating the substrate from its back. EG: an electron gun generating the high energy electron beam which is shining the substrate at grazing incidence. RS: a phosphorus screen by which the electron diffraction pattern can be monitored.

onto a plano-convex lens with a focal length of 40 cm. The final incidence angle of the laser beam onto the target is  $45^\circ$  and the spot size is about  $3.1 \text{ mm}^2$ . The *in-situ* high pressure RHEED consists of an electron gun which produces a collimated electron beam with an energy of 30 keV. The aperture size of the electron gun is about 0.5 mm. The PLD chamber is capable of holding five different disk-shaped targets in a carrousel. The targets can be rotated and toggled with a set of computerized motors. The substrate is placed normal to the target surface, which is glued on its backside with silver paste on a stainless steel made Omicron plate. The omicron plate is heated from the back with an infra-red laser beam with a spot size of 4 mm. The temperature of the substrate holder is monitored with a pyrometer from its back. During the deposition, a uniform pressure is achieved by allowing a gas flow into the chamber with a flow control valve and the continuous pumping through a bypass line attached to a turbo molecular pump.

### 3.2 Rutherford backscattering spectrometry

Rutherford backscattering spectrometry (RBS) is an analytical technique which can be used to determine the stoichiometry of a thin film. The technique is based on the elastic collision of high energetic projectile particles with the stationary target atoms in the film. In the following, we discuss the basic principle of the experiment.

Figure 3.3 demonstrates an elastic scattering process and illustrates the underlying concept of RBS. A high energetic, collimated beam of alpha particles ( $\text{He}^{2+}$ ) with energy  $E_0$  and mass  $M_1$  is projected onto a thin film. This leads to an elastic collision between the alpha particles and the stationary atoms in the film, which is governed by the strong Coulomb repulsion between the participating nuclei. As a result of this scattering, the scattered projectile acquires the energy  $E_1$  and a scattering angle  $\theta$ . The stationary target particle (mass,  $M_2$ ) gains the kinetic energy  $E_2$  and gets deflected at an angle  $\phi$ . From the conservation of momentum and energy, one can calculate the so-called kinematic factor,  $k$  which is [61]:

$$k = \frac{E_1}{E_0} = \left( \frac{M_1 \cos \theta \pm \sqrt{M_2^2 - M_1^2 \sin^2 \theta}}{M_1 + M_2} \right) \quad (3.1)$$

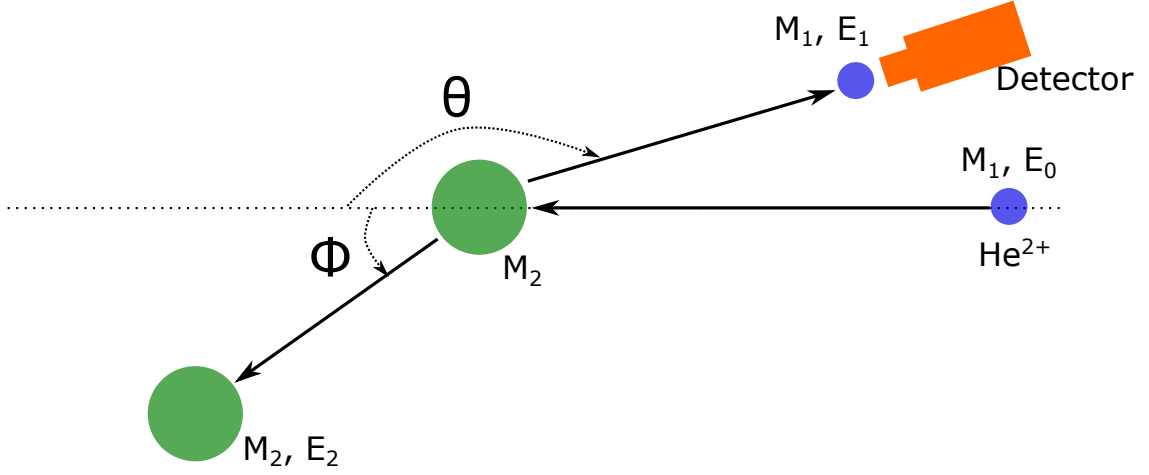


Figure 3.3: Schematic representation of elastic scattering in a RBS experiment. An alpha particle with mass  $M_1$  and initial energy  $E_0$  collides with a stationary target element of mass  $M_2$ . As a result of the collision, the alpha particle gets scattered with the energy  $E_1$  at an angle  $\theta$  and detected by a detector. The target particle gains the energy of  $E_2$  and has a deflection angle  $\phi$ . The whole scattering process conserves the total momentum and energy.

The ‘+’-symbol is taken when  $M_1$  is less than  $M_2$ . This equation suggests that the energy of the projectile at a particular scattering angle is a function of the mass of the stationary target element in the film. This characterizes the element sensitivity in the RBS experiment. The maximum energy resolution can be achieved if  $\theta$  is set to  $180^\circ$ .

The number of detected scattered projectiles ( $N_d$ ) at a particular energy and at a particular angle  $\theta$  is proportional to the number of incident projectiles ( $N_p$ ), the number of specific target elements ( $N_t$ ) and the related scattering cross section ( $\sigma(\theta)$ ), and can be expressed as:

$$N_d = N_p \times N_t \times \sigma(\theta) \times \omega \quad (3.2)$$

where  $\omega$  is the solid angle of the detector. The cross section  $\sigma$  is defined as:

$$\sigma = \int \frac{d\sigma}{d\omega} d\omega = \int \left( \frac{Z_1 Z_2 e^2}{4E_0} \right)^2 \frac{1}{\sin^4(\theta/2)} d\omega \quad (3.3)$$

where  $Z_1$  and  $Z_2$  are the atomic numbers of the incident alpha particle and the target element, respectively, and  $e$  is the electronic charge. Equation (3.3) shows that the RBS technique is most sensitive to the heavier elements with large atomic number. Performing RBS measurement, one finds the number of specific target elements of a given volume. The volume is defined by the thickness of the film and the area of the incident beam spot.

### 3.3 Resistance and magnetization measurements

The resistance measurements were carried out with a Physical Properties Measurement System made by Quantum Design (QD-PPMS). The temperature in the setup can be varied between 1.8-400 K and the available maximum field is 9 T. For resistance measurements, the conventional four-probe method was used with a DC excitation current of  $10 \mu\text{A}$ . For a highly resistive sample, an external Keithley source-meter was used. The current-voltage characteristics were measured with the Keithley source-meter as well. For consistent magneto-resistance measurements at different field directions, the applied current path was always perpendicular to the field direction.

The Vibrating Sample Magnetometer (VSM) option in the QD-PPMS was used to measure the magnetization of a sample. In this setup, the sample vibrates in an applied magnetic field with a frequency of 40 Hz inside a pickup coil. This vibration of a magnetic sample generates

an AC voltage in the pickup coil, which is later processed with a lock-in technique. The amplitude of the processed signal corresponds to the magnetic moment of the sample.

### 3.4 Ellipsometry

Ellipsometry is an optical spectroscopy technique which uses electromagnetic radiation to obtain the complex dielectric function of a material. The technique is based on the analysis of the polarization state of light after the reflection from a sample surface. The complex frequency dependent dielectric function is defined as:

$$\epsilon(\omega) = \epsilon_1(\omega) + i\epsilon_2(\omega) \quad (3.4)$$

where  $\omega$  is the frequency of electromagnetic radiation,  $\epsilon_1$  and  $\epsilon_2$  are the real and imaginary parts of the complex dielectric function, respectively. The complex optical conductivity ( $\sigma(\omega)$ ) is directly related to  $\epsilon(\omega)$  according to:

$$\sigma(\omega) = -i\omega(\epsilon(\omega) - 1)\epsilon_0 \quad (3.5)$$

where  $\epsilon_0$  corresponds to the permittivity in vacuum. In the following, we discuss how ellipsometry measures the complex dielectric constant, and thereby the optical conductivity.

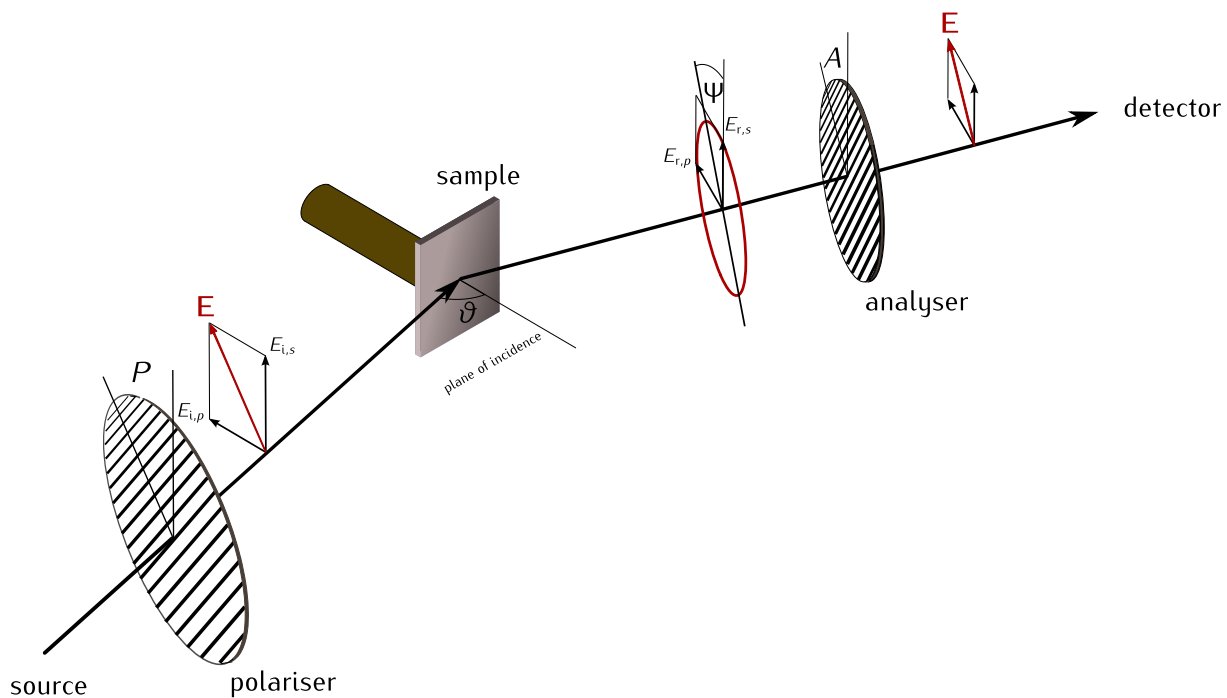


Figure 3.4: A schematic diagram of an ellipsometry setup. A linear polarizer, with an angle  $P$ , selects the direction of the electric field vector of the incoming radiation. The linearly polarized light is reflected from the sample surface at an angle  $\vartheta$  and becomes elliptically polarized. A rotating analyzer is placed after the sample to probe the polarization state of the reflected light. Finally, a detector records the intensity of the reflected light at various angles ( $A$ ) of the analyzer. Figure is taken from Ref. [62].

Figure 3.4 schematically shows a basic ellipsometry setup with a rotating analyzer. At first, a linear polarizer, which is set at a fixed angle  $P$  with respect to its transmission axis, polarizes the incoming light. Consequently, the incoming radiation can be decomposed into two components  $E_{i,p}$  and  $E_{i,s}$  that are parallel and perpendicular to the plane of incidence, respectively. This light is reflected from the sample surface at an angle  $\vartheta$ . This reflected light from the sample is generally elliptically polarized. With a second linear polarizer, the so-called

analyzer, the polarization state of the reflected light is probed. By rotating the analyzer in equidistant steps, one records the intensity of the transmitted light with a detector which is polarization insensitive.

The polarization state of the reflected light can be described in terms of the ellipsometric angles and the amplitudes of the electric fields  $E_p$  and  $E_s$ . This yields:

$$\frac{E_p^2}{E_0^2} + \tan^2\Psi \frac{E_s^2}{E_0^2} - 2\tan\Psi \frac{E_p}{E_0} \frac{E_s}{E_0} \cos\Delta = \sin^2\Psi \sin^2\Delta \quad (3.6)$$

Equation (3.6) represents the polarization state in the  $E_p$  and  $E_s$  coordinate system, as

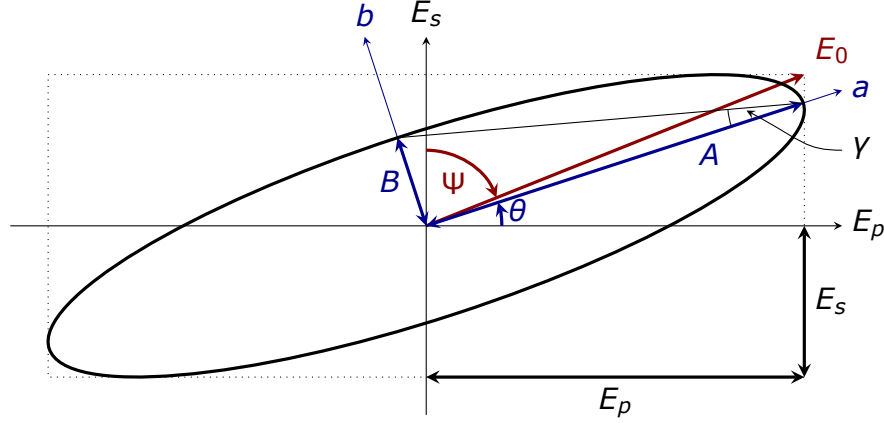


Figure 3.5: An example of a polarization ellipse whose main axes rotated by an angle  $\theta$ . The amplitude  $E_0$  and the corresponding ellipsometric angle  $\Psi$ .  $\gamma$  is the ellipticity angle which contains information of the phase shift ( $\Delta$ ) of the reflected light wave. Figure is taken from Ref. [62].

shown in Figure 3.5. The tilting angle of the polarization ellipse,  $\Psi$ , is defined as  $\Psi = \frac{E_p}{E_s}$ . The phase difference,  $\Delta$ , is contained in the eccentricity of the polarization ellipse. With the ellipsometry technique, we measure these two quantities  $\Psi$  and  $\Delta$  directly. The measurement involves recording the intensity ( $I$ ) at every wavelength of the reflected light by varying the analyzer angle ( $A$ ). One can fit this intensity modulation  $I(A)$  with the following equation:

$$I(A) = \frac{I(P)|r_s|^2 \cos^2 P}{2(\tan^2\Psi + \tan^2 P)} (1 + \alpha_2 \cos(2A) + \beta_2 \sin(2A)) \quad (3.7)$$

where  $r_s$  is the amplitude reflection coefficient for s-polarized light (when electric field vector of incoming electromagnetic radiation is parallel to the sample surface),  $\alpha_2$  and  $\beta_2$  are the Fourier coefficients. These coefficients are defined as:

$$\alpha_2 = \frac{\tan^2\Psi - \tan^2 P}{\tan^2\Psi + \tan^2 P} \quad (3.8a)$$

$$\beta_2 = \frac{2\tan\Psi \tan P \cos\Delta}{\tan^2\Psi + \tan^2 P} \quad (3.8b)$$

The ellipsometric angles  $\Psi$  and  $\Delta$  are obtained from  $\alpha_2$  and  $\beta_2$ , as the the absolute intensity  $I(P)$  is generally unknown. Finally, the so-called ellipsometric ratio reads:

$$\rho = \tan\Psi \exp(-i\Delta) = \frac{1 + \alpha_2}{\beta_2 \pm i\sqrt{1 - \alpha_2^2} - \beta_2} \frac{\tan P}{1 - \tan P} \quad (3.9)$$

The dielectric function  $\epsilon(\omega)$  is directly related to  $\rho$  according to the following equation:

$$\epsilon(\omega) = \sin^2(\vartheta) \left( 1 + \tan^2\vartheta \left[ \frac{1 - \rho}{1 + \rho} \right]^2 \right) \quad (3.10)$$

Using Equations (3.5) and (3.10), the real part of optical conductivity ( $\sigma_1$ ) can be expressed as:

$$\sigma_1(\omega) = \epsilon_0 \epsilon_2 \omega \quad (3.11)$$

The real part of the optical conductivity of the investigated samples was calculated following Equation (3.11).

### 3.5 Polarized neutron reflectometry

In this thesis, polarized neutron reflectometry (PNR) was used to study the structural and magnetic depth profiles of YBCO/LCMO superlattices in the direction of the growth. As the neutrons strongly scatter from the atomic nuclei, one can obtain structural parameters, like the scattering length density, thickness and roughness of a multilayer by using neutrons of an appropriate wavelength. Importantly, the neutron spin interacts with the magnetic moments of the sample, which allows one to obtain their magnitude and direction. In the following, we discuss the theory on how the PNR technique provides the structural and magnetic properties of a superlattice.

#### 3.5.1 Interaction of neutron with matter

In an interaction of neutrons with matter, the related scattering potential arises from the strong interaction of the neutrons with the atomic nuclei and the coupling of the neutron spin with the magnetic induction of the sample. The effective nuclear potential of a solid,  $V_n$ , is defined [63] as:

$$V_n = \frac{2\pi\hbar^2}{m_n} \sum_i N_i b_i = \frac{2\pi\hbar^2}{m_n} \rho_n \quad (3.12)$$

where  $m_n = 1.6749 \times 10^{-27}$  kg is the mass of a neutron,  $N_i$  is the number density of a particular atomic nuclei or isotope and  $b_i$  is the corresponding scattering length. The summation runs over the various atoms and isotopes in the solid. The parameter  $\rho_n = \sum_i N_i b_i$  represents the total scattering length density of a compound. The parameter  $b_i$  has both real and imaginary parts; the real part accounts for the scattering probability, whereas the imaginary part is responsible for neutron absorption. The imaginary part of  $b_i$  can be neglected for the PNR experiment in this thesis, as it has been carried out with cold neutrons of energy  $E < 0.025$  eV. Regardless, one can calculate  $\rho_n$  of a given compound from the  $b_i$  of individual elements as tabulated in Ref. [64], given that the stoichiometry of the compound is known.

The magnetic part of the neutron potential,  $V_m$ , which according to Zeeman energy reads:

$$V_m = -\boldsymbol{\mu} \cdot \mathbf{B} \quad (3.13)$$

where  $\boldsymbol{\mu}$  and  $\mathbf{B}$  are the magnetic moment of the neutron and the magnetic induction in the solid, respectively. The neutron moment can be expressed as  $\boldsymbol{\mu} = -\mu_n \boldsymbol{\sigma}$ ; where  $\mu_n$  and  $\boldsymbol{\sigma}$  correspond to the magnitude of the moment and the Pauli spin matrices, respectively. The magnetic induction,  $\mathbf{B}$ , of Equation (3.13) contains contributions from the applied magnetic field ( $\mathbf{H}$ ) and the sample magnetization ( $\mathbf{M}$ ), according to:

$$V_m = \mu_n \mu_0 \boldsymbol{\sigma} \cdot (\mathbf{H} + \mathbf{M}) \quad (3.14)$$

where  $\mu_0$  is the magnetic permeability in free space. If the sample is a superlattice that consists of two different materials, the PNR measurement is governed by the contrast of their contributions to the potential. As the applied magnetic field,  $\mathbf{H}$ , is the same in both materials, the PNR will be sensitive to the magnetization of the individual layers. Related to this, the so-called magnetic scattering length density is defined as:

$$\rho_m = \frac{\mu_0 \mu_n m_n}{2\pi\hbar^2} M \quad (3.15)$$

Equation (3.15) demonstrates that the scattering probability is proportional to the sample magnetization.

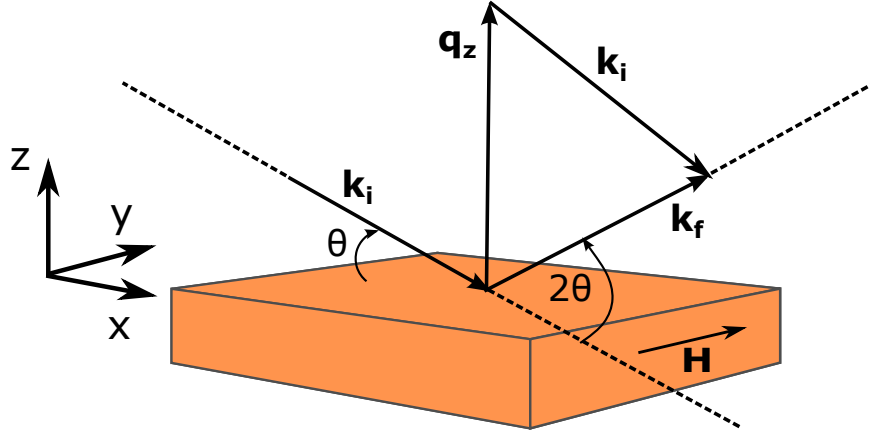


Figure 3.6: Schematic diagram of a polarized neutron reflectometry experiment in specular geometry. The neutron propagation direction is along the  $x$ -axis. The angle  $\theta$  corresponds to the incident and the reflected angles. The  $\mathbf{k}_i$  and  $\mathbf{k}_f$  are the incident and the reflected wave vectors. The momentum transfer ( $\mathbf{q}_z$ ) vector is directed to the  $z$ -axis. The applied magnetic field ( $\mathbf{H}$ ) and the neutron spin quantization axis are along the  $y$ -axis. The PNR experiment is sensitive only to the magnetization components which are within the  $xy$ -plane.

### 3.5.2 Specular reflectivity

The description of the PNR technique is restricted to the specular reflectivity for the non-spin-flip scattering. In specular geometry, the incident and the reflected angles are identical, and therefore, the momentum transfer vector is restricted to the direction of the sample normal. Figure 3.6 illustrates a scattering geometry for such a specular PNR experiment. The sample surface is within the  $xy$ -plane. The  $xz$ -plane is the scattering plane, containing the incident ( $\mathbf{k}_i$ ) and reflected ( $\mathbf{k}_f$ ) wave vectors, and the momentum transfer vector ( $\mathbf{q}_z$ ). The  $y$ -direction corresponds to the neutron spin quantization axis and the applied field direction. As the incident and the reflected angles are the same,  $q_z$  can be written as:

$$q_z = 2k \sin \theta = \frac{4\pi}{\lambda} \sin \theta \quad (3.16)$$

where  $k = \frac{2\pi}{\lambda}$  corresponds to the magnitude of the incident and reflected neutron wave vectors.

For a perfectly homogeneous sample surface, the kinetic energy of the neutron ( $\frac{\hbar^2 k_x^2}{2m_n}$ ) along its propagation direction ( $x$ -axis) does not change. Only the  $z$ -component of the kinetic energy changes as a result of the refraction. Therefore, the whole problem becomes very similar to the one of a particle in a one dimensional box potential ( $V = V_n + V_m$ ) with the kinetic energy,  $\frac{\hbar^2 k_z^2}{2m_n} = \frac{\hbar^2 q_z^2}{8m_n}$ . The value of  $k_z = \frac{q_z}{2}$  defines the  $z$ -component of the wave vector. For a semi-infinite slab with a potential step of  $V(z) = V$ , the so-called Fresnel reflectivity can be written as:

$$R(q_z) = \left| \frac{q_z - \sqrt{q_z^2 - \frac{8m_n V}{\hbar^2}}}{q_z + \sqrt{q_z^2 - \frac{8m_n V}{\hbar^2}}} \right|^2 \quad (3.17)$$

When the neutron energy  $\frac{\hbar^2 q_z^2}{8m_n} < V$ , the square roots in Equation (3.17) yield imaginary numbers, and the denominator becomes the complex conjugate of the numerator. This results in the reflectivity of one, which is the so-called total reflection. Finite transmission occurs when the neutron wave vector is larger than the critical value,  $q_c = \sqrt{\frac{8m_n V}{\hbar^2}}$ . This is known as the total reflection edge. For  $q_z \gg q_c$ , the value of  $R(q_z)$  is approximately equal to  $\frac{|2m_n V|^2}{q_z^4 \hbar^4}$ , which gives rise to the quick reduction of  $R(q_z)$  beyond the total reflection edge.

For a superlattice, the transmitted neutron wave from the first layer suffers multiple reflections and transmissions at every interface of the multilayers. The resulting reflectivity

curve is therefore the superposition of all these reflections and transmissions. Consequently, the periodicity of the superlattice, i.e., the bilayer repetitions lead to peaks which are known as the superlattice Bragg peaks (SLBP). The recursive Parratt's method for such multilayer system yields the reflectance ( $\mathcal{R}_j$ ) at the layer  $j$ , which is:

$$\mathcal{R}_j = \frac{k_j - k_{j+1}}{k_j + k_{j+1}} \quad (3.18)$$

where  $k_j$  and  $k_{j+1}$  are the wave vectors in the  $j$  and  $j + 1$  layers, respectively. In Equation (3.18), an important assumption is that the reflected amplitude in the  $(j + 1)$  layer is zero. The wave vectors  $k_j$  for spin-up and spin-down neutrons are defined by the following equations.

$$k_j = \sqrt{k_z^2 - 4\pi(\rho_{n,j} + \rho_{m,j})} \quad : \text{ For spin-up neutrons} \quad (3.19a)$$

$$k_j = \sqrt{k_z^2 - 4\pi(\rho_{n,j} - \rho_{m,j})} \quad : \text{ For spin-down neutrons} \quad (3.19b)$$

The sign of  $\mathcal{R}_j$  in Equation (3.18) depends on the magnitude of the wave vectors in the consecutive layers. If the scattering length density of the layer  $j$  is larger than the one of the following layer, the reflectance is negative. The negative sign corresponds to a  $\pi$ -phase difference between the incoming and the reflected waves at the interface. For a superlattice with symmetric layer thicknesses, this  $\pi$ -phase difference gives rise to the suppression of the even order SLBPs.

### 3.5.3 Impact of roughness on reflectivity profile

We have so far discussed the case of samples which have flat surfaces and sharp interfaces, where the potential was assumed as a step-potential. In reality, the thickness of the layers in a superlattice changes along the lateral direction. This is known as roughness. By considering such roughness, with the help of Equation (3.18), the reflectivity at the  $j$  interface reads:

$$R_j = |\mathcal{R}_j|^2 = \left| \frac{k_j - k_{j+1}}{k_j + k_{j+1}} \right|^2 e^{-2k_j k_{j+1} \sigma_j^2} = R_j^{\text{flat}} e^{-2k_j k_{j+1} \sigma_j^2} \quad (3.20)$$

where  $\sigma_j$  accounts for the roughness of the layer  $j$ . Due to the presence of the surface roughness, the reflectivity of the flat surface ( $R_j^{\text{flat}}$ ) is modified by the so-called Nevot-Croce factor  $e^{-2k_j k_{j+1} \sigma_j^2}$ . This leads to the additional decay of the reflectivity profile. As  $k_j$  and  $k_{j+1}$  increase, the reduction of the reflectivity profile gets stronger. For this reason, the roughness effect is prominent at high  $q_z$ . Figure 3.7a displays a set of reflectivity profiles for a symmetric YBCO/LCMO multilayers with 10 bilayer repetitions with zero and finite roughness of the layers. It illustrates that the finite roughness of 10 Å leads to the faster decay of the reflectivity profile.

### 3.5.4 Impact of instrumental resolution on reflectivity profile

In Parratt's formalism, the value of  $q_z$  is well defined. However, in an experiment, an uncertainty in the determination of  $q_z$  arises from the measurement of the incident ( $\theta_i$ ) and the reflected ( $\theta_f$ ) angles, and the wavelength ( $\lambda$ ) distribution of the incident neutrons. The momentum transfer vector along  $z$ -axis can be written as:

$$q_z = \frac{2\pi}{\lambda} (\sin\theta_i + \sin\theta_f) \quad (3.21)$$

The maximum proportional error in the determination of  $q_z$  reads:

$$\Delta q_z = \frac{2\pi}{\lambda} \sqrt{(\cos\theta_i \Delta\theta_i)^2 + (\cos\theta_f \Delta\theta_f)^2 + (\sin\theta_i + \sin\theta_f)^2 \left( \frac{\Delta\lambda}{\lambda} \right)^2} \quad (3.22)$$

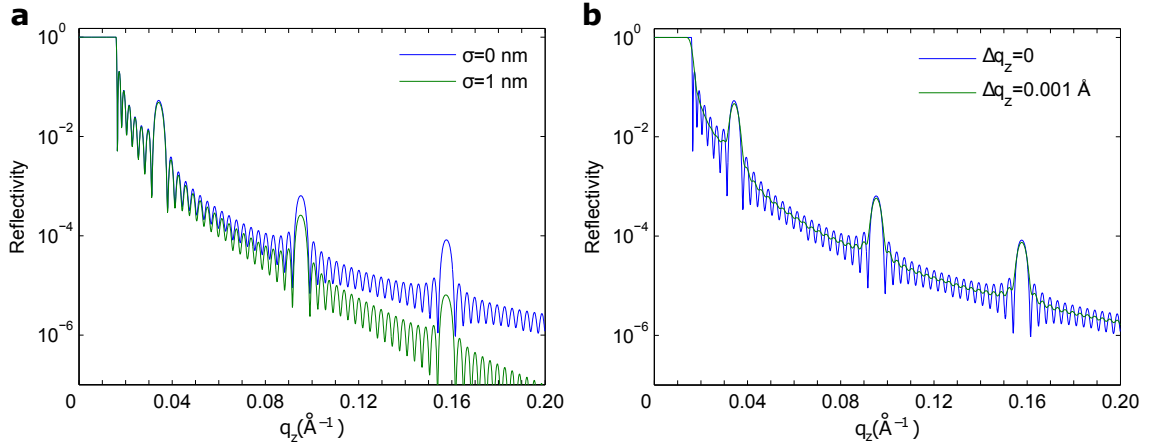


Figure 3.7: A set of simulated reflectivity profiles for a symmetric YBCO/LCMO multilayers with 10 bilayer repetitions for (a) zero and finite roughness, and (b) perfect and finite instrumental resolution.

In an angle dispersive experiment, the  $\left(\frac{\Delta\lambda}{\lambda}\right)$  is about 1%, as the neutron beams are selected with a monochromator. Therefore, the angular divergence of  $\theta_i$  and  $\theta_r$  mainly contributes to  $\Delta q_z$ . The  $\Delta\theta_{i,r}$  are governed by a set of slits before and after the sample, and the selection of specular region on 2D detector.

Figure 3.7b demonstrates that the fast oscillations are well resolved in the case of perfect resolution. However, for the finite  $\Delta q_z$ , the fast oscillations are averaged out. To incorporate  $\Delta q_z$  in the calculation, the reflectivity with perfect resolution is determined first. Then the obtained reflectivity is convoluted with a Gaussian function of width  $\Delta q_z(q_z)$ .

### 3.5.5 Setting up a PNR experiment

We performed the PNR experiment at the NREX beamline of the FRMII reactor in Garching, Germany. We used a monochromatic neutron beam of wavelength 4.28 Å with a wavelength resolution ( $\Delta\lambda/\lambda$ ) of 1-2%. To obtain the reflectivity curve against  $q_z$ , we varied the angle of incidence of the incoming neutron beam on the sample and the detector to satisfy the specular condition. The sample was mounted in a vertical closed cycle cryostat equipped with an electromagnet of maximum field of 0.45 T. The base temperature of the cryostat is about 4 K. We rotated the sample stage in order to vary the angle of incidence. A transmittance supermirror with polarizing efficiency of 99% was used to get the neutrons with different spins. A 2D detector with an area of 200×200 mm<sup>2</sup> was placed at 246.5 cm away from the sample to capture the reflected signal which consists of both the specular and the off-specular parts. The details about the instrument can be found in Ref. [65].

## 3.6 X-ray absorption spectroscopy

In this section, we discuss the concepts underlying the x-ray magnetic circular dichroism (XMCD) and x-ray linear dichroism (XLD) techniques which are used in this work to obtain the element specific information on magnetism and orbital occupancy.

### 3.6.1 Interaction of x-ray on the atomic scale

When an atom is illuminated with x-rays, its charge and magnetic moment interacts with the electromagnetic field of the x-rays. Such electromagnetic radiation can be represented in terms of the vector potential:

$$\mathbf{A}(\mathbf{r}) = \sum_{\mathbf{k},\alpha} A_0(e_{\mathbf{k},\alpha} b_{\mathbf{k},\alpha} e^{i\mathbf{k}\cdot\mathbf{r}} + e_{\mathbf{k},\alpha}^* b_{\mathbf{k},\alpha}^\dagger e^{-i\mathbf{k}\cdot\mathbf{r}}) \quad (3.23)$$

where  $\mathbf{r}$  represents the space coordinate,  $A_0$  is a factor that determines the magnitude,  $\mathbf{e}_{\mathbf{k},\alpha}$  is a polarization vector for the photon with wave vector  $\mathbf{k}$  and polarization  $\alpha$ ,  $b_{\mathbf{k},\alpha}$  is a photon annihilation operator and  $b_{\mathbf{k},\alpha}^\dagger$  is a photon creation operator.

The Hamiltonian is dominated by the electronic part of the atom. The first order terms of the interaction Hamiltonian ( $H_{int}$ ) are:

$$H_{int} = \frac{e}{mc} \sum_j \mathbf{p}_j \cdot \mathbf{A}(\mathbf{r}_j) + \frac{e}{2mc} \sum_j \sigma_j \cdot \nabla \times \mathbf{A}(\mathbf{r}_j) \quad (3.24)$$

where  $\mathbf{r}_j$ ,  $\mathbf{p}_j$  and  $\sigma_j$  are the position, momentum and spin of the  $j^{th}$  electron in the atom, respectively. The first term of  $H_{int}$  accounts for the interaction of the electron moment with the electric field of the incident x-ray radiation. The second term describes the magnetic field,  $\mathbf{B} = \nabla \times \mathbf{A}$ , acting on the spin of the electron. In core-valence electron spectroscopy, the electron spin does not have any significant role. Therefore, we can neglect the second term of the Hamiltonian. In case of photon absorption, only the photon annihilation part of Equation (3.23) concerns the Hamiltonian. Hence, the equation for  $H_{int}$  becomes:

$$H_{int} = \frac{eA_0}{mc} \sum_j \sum_{\mathbf{k},\alpha} \mathbf{p}_j \cdot \mathbf{e}_{\mathbf{k},\alpha} b_{\mathbf{k},\alpha} e^{i\mathbf{k} \cdot \mathbf{r}} \quad (3.25)$$

The Taylor expansion of  $e^{i\mathbf{k} \cdot \mathbf{r}}$  yields the first order approximation  $1 + i\mathbf{k} \cdot \mathbf{r} + \dots$ . For the soft x-ray absorption, it is commonly assumed that  $\mathbf{k} \cdot \mathbf{r} \ll 1$ , such that the second term can be neglected. This is known as the dipole approximation which yields:

$$H_{int} \approx \frac{eA_0}{mc} \sum_j \sum_{\mathbf{k},\alpha} \mathbf{p}_j \cdot \mathbf{e}_{\mathbf{k},\alpha} b_{\mathbf{k},\alpha} \quad (3.26)$$

According to Fermi's Golden rule, the transition probability ( $W_{fi}$ ) per unit time from an initial state  $|\psi_i\rangle$  to a final state  $|\psi_f\rangle$  by absorbing a photon with an energy of  $\hbar\omega$  is:

$$W_{fi} \propto |\langle \psi_f | T | \psi_i \rangle|^2 \rho(E_f) \delta(E_f - E_i - \hbar\omega) \quad (3.27)$$

where  $E_f$  and  $E_i$  are the final and initial state energies, respectively, and  $\rho(E_f)$  accounts for the density of the empty states with energy  $E_f$ .  $T$  represents the transition operator which according to first order approximation almost equals to  $H_{int}$ . Using Equation (3.26) and Equation (3.27), this yields:

$$W_{fi} \propto \sum_j \sum_{\alpha} |\langle \psi_f | \mathbf{p}_j \cdot \mathbf{e}_{\alpha} | \psi_i \rangle|^2 \rho(E_f) \delta(E_f - E_i - \hbar\omega) \quad (3.28)$$

The delta function indicates that the transition is possible only when the energy of the absorbed photon equals the energy difference between the final and initial states. The term  $\langle \psi_f | b_{\alpha} | \psi_i \rangle \propto \sqrt{I_0}$  is related to the incident photon intensity  $I_0$ . Using the Heisenberg relation,  $[\mathbf{r}_j, H] = (i\hbar/m)\mathbf{p}_j$ , one can convert Equation (3.28) into Equation (3.29).

$$W_{fi} \propto \sum_j \sum_{\alpha} |\langle \psi_f | \mathbf{r}_j \cdot \mathbf{e}_{\alpha} | \psi_i \rangle|^2 \rho(E_f) \delta(E_f - E_i - \hbar\omega) \quad (3.29)$$

After the absorption of a photon, a hole is created in a core state and an unoccupied valence state is filled with an electron. Assuming the core-hole pair does not modify the wave functions for the initial and final states, the  $W_{fi}$  can be written in terms of the single particle transition probabilities [66]:

$$T_{fi} \propto \sum_{\alpha} |\langle \phi_f | \mathbf{r}_j \cdot \mathbf{e}_{\alpha} | \phi_i \rangle|^2 \rho(E_f) \delta(E_f - E_i - \hbar\omega) \quad (3.30)$$

where  $T_{fi}$  is the probability for an electron to be excited from the initial single particle state  $|\phi_i\rangle$  to the final single particle state  $|\phi_f\rangle$  by absorbing a photon with energy  $\hbar\omega$ . Finally,

the x-ray absorption coefficient is proportional to the summation over all possible  $|\phi_i\rangle \rightarrow |\phi_f\rangle$  transition probabilities, i.e.,  $\sum_{i,f} T_{i,f}$ . The matrix elements of  $\mathbf{r}_j \cdot \mathbf{e}_\alpha$  for given initial and final states account for the photon polarization dependent absorption, which is known as ‘search light effect’ [67]. As the x-ray absorption process is governed by the electric dipole transition, the core level electrons preferably get excited in the direction of the electric field vector  $\vec{E}$ . Therefore, the transition probability to an empty state is sensitive to the projection of its wave function along the electric field vector.

In addition, as the x-ray photons carry momentum, the absorption process must satisfy the conservation of the total momentum. For the absorption of x-ray photons with angular momentum,  $l_p = \pm 1$ , the orbital angular momentum quantum number ( $l$ ) of the final state should be either  $l + 1$  or  $l - 1$ . This gives rise to the selection rule:

$$\Delta l = \pm 1 \quad (3.31)$$

The projection of the photon angular momentum along the quantization direction, i.e., the beam propagation direction, gives  $m_{l_p} = \pm 1, 0$ . Therefore, the orbital magnetic quantum numbers of the initial and the final states must satisfy the following equation:

$$\Delta m_l = 0, \pm 1 \quad (3.32)$$

As the photon does not carry any spin, the spins of the initial and the final states must be the same. This spin conservation gives rise to

$$\Delta s = 0 \quad (3.33)$$

and

$$\Delta m_s = 0 \quad (3.34)$$

### 3.6.2 X-ray magnetic circular dichroism

In a x-ray magnetic circular dichroism (XMCD) experiment, one measures the x-ray absorption spectra (XAS) for the circularly polarized x-rays with positive and negative helicities. The difference between the two XAS curves, i.e., the XMCD signal, contains the information about the magnetism of an element. The following discussion addresses the origin of such a XMCD signal and its relationship with the magnetic properties.

The XMCD experiment can be understood in terms of a two-step model that was coined by J. Stöhr [67]. Figure 3.8a schematically summarizes the model for a transition metal ion like Cu or Mn. The magnetization ( $\mathbf{M}$ ) direction of the sample has been chosen along the up direction, which is also the direction of the x-ray propagation vector ( $\mathbf{k}$ ). In a first step, the circularly polarized x-ray with positive or negative helicity excites the core-level electrons from the  $2p$  to  $3d$  states. This process involves a change of the angular momentum of the excited electrons by  $+\hbar$  or  $-\hbar$ . As mentioned earlier, the electron spin does not interact with the electric field vector,  $\vec{E}$ . Therefore, in the absence of spin-orbital (s-o) coupling, the photon angular momentum is transferred to the orbital part of the excited electron. However, as a result of the s-o coupling of the  $2p$  electrons for Cu and Mn, the photon angular momentum is transferred to both the orbital ( $l$ ) and the spin ( $s$ ) parts of the electronic angular momentum. At the  $L_3$ -edge ( $2p_{3/2} \rightarrow 3d$  transition), the x-ray that carries  $+\hbar$  momentum, mainly excites the spin-up electrons. This is because the  $l$  and  $s$  are parallel at the  $2p_{3/2}$ -level. The reverse holds for the x-ray with negative helicity. At the  $2p_{1/2}$ -level, the coupling between  $l$  and  $s$  are antiparallel. Consequently, the x-rays with positive (negative) helicity excite more spin-down (spin-up) electrons for the  $L_2$ -edge ( $2p_{1/2} \rightarrow 3d$  transition).

In the second step, one considers that the empty states of the  $3d$ -band determine the intensity of the absorption profiles at the two edges. As the magnetization is pointing up, the number of spin-down electrons is larger than the number of spin-up electrons, giving rise to more empty states (or holes) in the spin-up band. Due to the larger number of holes in the spin-up band, more spin-up electrons can be excited from the  $2p_{3/2}$ -level by the x-ray

with positive helicity. At the  $L_3$ -edge, the intensity for the absorption of x-ray photons with positive helicity ( $\mu_+$ ) is therefore larger than the one for negative helicity ( $\mu_-$ ), as shown in Figure 3.8b (upper panel). The inverse trend is observed at the  $L_2$ -edge for which the electrons are excited from the  $2p_{1/2}$ -level. Hence, the difference spectra ( $\mu_+ - \mu_-$ ), as shown in the lower panel of Figure 3.8b, contains the information about the magnetic state of the sample. If the empty states in the  $3d$ -valence band have an imbalance in the number of the magnetic orbital quantum numbers,  $m_l$ , with  $\sum m_l \neq 0$ , the orbital moment also contributes to the XMCD signal. This arises in case of sizable s-o coupling in the  $3d$ -level. If the distribution of spins in the  $3d$ -band is anisotropic, the so-called magnetic dipole operator gives rise to an additional contribution to the XMCD signal. This arises if the transition probabilities from a given  $m_l$  state to the final states with  $m_l + 1$  and  $m_l - 1$  are different, as a result of the ‘search light effect’.

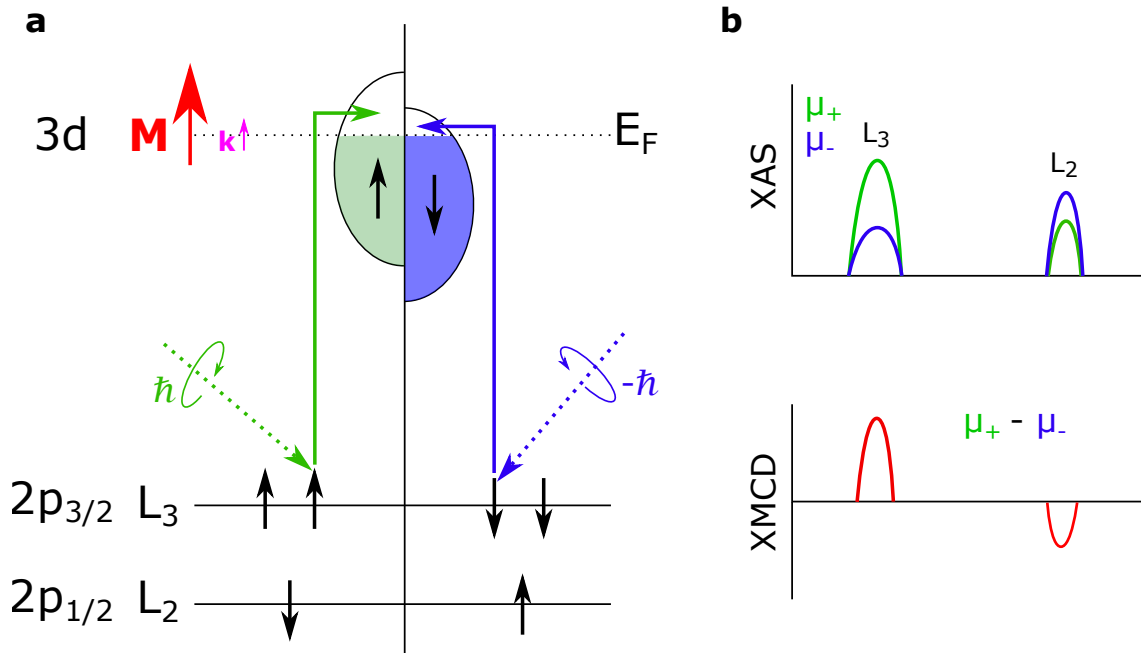


Figure 3.8: (a) A schematic representation of the x-ray magnetic circular dichroism effect for transition metal ion. The magnetization ( $\mathbf{M}$ ) is chosen to point up and to be parallel to the x-ray propagation vector ( $\mathbf{k}$ ). The spin magnetic moment ( $M_s$ ) of an electron is defined as  $M_s = -2\mu_B m_s$ . The transition arises from the core levels ( $2p_{3/2}$  and  $2p_{1/2}$ ) to the empty  $3d$ -states above the Fermi level ( $E_F$ ). (b) Upper panel: Absorption curves for positive and negative helicities of x-ray photons,  $\mu_+$  and  $\mu_-$ , respectively. The relative intensities of the x-ray absorption spectra (XAS) are determined by the selective excitations of the core-level spin-up and spin-down electrons, and the empty states of the  $3d$ -spin-up and  $3d$ -spin-down bands. Lower panel: Calculated XMCD signal ( $\mu_+ - \mu_-$ ) which reflects the the magnetic state of the particular ion.

### Calculation of the transition probability

Here, we present the method to calculate the percentage of excited spin-up and spin-down electrons by the left and right circularly polarized x-rays from the  $2p_{3/2}$  and  $2p_{1/2}$  levels. For this purpose, we express the  $2p$ - and  $3d$ -electron states in the basis of the magnetic orbital ( $m_l$ ) and spin ( $m_s$ ) quantum numbers, i.e.,  $|m_l, m_s\rangle$ . Due to the strong s-o coupling, the basis of  $|j, m_j\rangle$  represents the  $2p$ -electron states better, where  $j$  and  $m_j$  are the total angular momentum and total magnetic angular momentum quantum numbers, respectively. Following Equation (3.35), one can evaluate the Clebsch-Gordan coefficients ( $C_{CG}$ ) to express  $|j, m_j\rangle$  in the basis of  $|l, s, m_l, m_s\rangle$ . The matrix in Equation (3.35) represents the so-called Wigner  $3j$ -symbol which yields a number. The  $m_j = m_l + m_s$  relationship determines the possible  $|m_l, m_s\rangle$  states.

$$\langle l, s, m_l, m_s | j, m_j \rangle = (-1)^{-l+s-m} \sqrt{2j+1} \begin{bmatrix} l & s & j \\ m_l & m_s & -m_j \end{bmatrix} \quad (3.35)$$

The transition from one  $|l, s, m_l, m_s\rangle$  state to another, after absorbing a photon of  $m_{lp}$ , is determined by the selection rules, as described in Equations (3.31) to (3.34). The probability ( $T_{fi}$ ) of such a transition must be calculated from Equation (3.30). Finally, the contribution of each transition to the absorption intensity is given by the multiplication of  $T_{fi}$  and the probability of finding an electron in a core  $|m_l, m_s\rangle$  state. The latter is the square of the related  $C_{CG}$  coefficient. Below, we show the calculation for  $T_{fi}$ .

In Cartesian coordinate system, the polarization vectors for the positive and negative helicities of x-ray are:

$$\begin{aligned} \mathbf{e}_1 &= \frac{1}{\sqrt{2}}(-\hat{x} + i\hat{y}) && : \text{positive helicity} \\ \mathbf{e}_2 &= \frac{1}{\sqrt{2}}(\hat{x} + i\hat{y}) && : \text{negative helicity} \end{aligned}$$

For the transition with the x-rays of positive helicity, the  $\mathbf{r}_j \cdot \mathbf{e}_\alpha$  term in Equation (3.30) can be written with the help of spherical harmonics as:

$$\mathbf{r} = x\hat{x} + y\hat{y} + z\hat{z} \quad (3.36a)$$

$$\mathbf{r} \cdot \mathbf{e}_1 = \frac{1}{\sqrt{2}}(-x + iy) = -\sqrt{\frac{4\pi}{3}} r Y_{1,-1} \quad (3.36b)$$

According to Equation (3.36b), the probability for the transition from  $|l, m_l\rangle$  to  $|l', m'_l\rangle$  by absorbing a photon of positive helicity reads:

$$T_{fi} \propto |\langle l', m'_l | Y_{1,-1} | l, m_l \rangle|^2 \quad (3.37)$$

Using the Wigner  $3j$ -symbol one obtains:

$$\langle l', m'_l | Y_{1,-1} | l, m_l \rangle = R(-1)^{l-m_l} \sqrt{l+1} \begin{bmatrix} l' & 1 & l \\ -m'_l & -1 & m_l \end{bmatrix} \quad (3.38)$$

where  $R$  corresponds to the radial part which is approximately the same for all the possible transitions. Therefore, it does not influence the relative probability calculations for all the transitions.

Figure 3.9 summarizes all possible  $2p \rightarrow 3d$  transitions including their percentage contributions to the total absorption intensity for the x-ray photons of positive helicity. At the  $2p_{3/2}$ -level, the photon with  $\hbar$  angular momentum excites 62.5 % spin-up electrons and 37.5 % spin-down electrons. Whereas, at the  $2p_{1/2}$ -level, they are 25 % and 75 %, respectively.

### 3.6.3 X-ray linear dichroism

With x-ray linear dichroism (XLD), one studies the variation of the XAS signal as a function of the polarization direction of the linearly polarized x-rays. From this experiment, one can deduce the density of holes in the band at the Fermi level and determine whether they predominantly occupy in-plane or out-of-plane orbitals. The origin of the XLD effect can be understood in terms of the ‘search light effect’, that was mentioned earlier. The electrons are preferentially excited into the orbitals which are extended along the direction of the field vector,  $\vec{E}$ . In the following, we discuss the linear polarization dependent absorption for the  $2p \rightarrow 3d$  transition.

For  $2p \rightarrow 3d$  transition, the initial states are defined as  $|2p_{j,m_j}\rangle$ . By neglecting the s-o coupling in the  $3d$ -level, the final states can be described by five different  $m_l$  values of the  $3d$ -orbitals. The combinations of these five levels yield a set of wave functions that represent

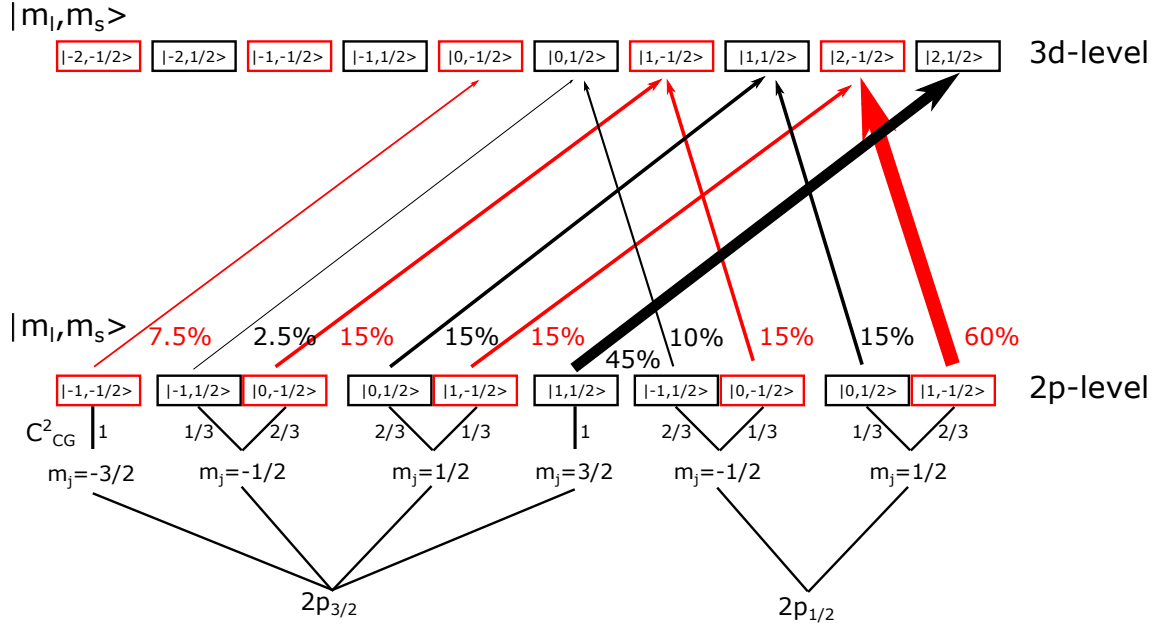


Figure 3.9: A schematic representation of the possible  $2p \rightarrow 3d$  transitions for circularly polarized x-rays carrying the angular momentum of  $+\hbar$ . The electron states are presented in the basis of  $|m_l, m_s\rangle$ . Spin-orbit coupling is neglected for the  $3d$ -band, but it is prominent in case of the  $2p$ -band. The square of the Clebsch-Gordan coefficient ( $C_{CG}^2$ ) determines the probability of finding an electron in a  $|m_l, m_s\rangle$  state for a given  $m_j$ . The red and black boxes are the states with spin-down and spin-up electrons, respectively. Transitions obey the selection rules  $\Delta m_l = 1$  and  $\Delta m_s = 0$ . All the states in the  $3d$ -level are assumed to be empty. The allowed transitions are marked by arrows. The width of the arrows are proportional to the corresponding contributions to the absorption intensity at the  $L_3$  and  $L_2$  edges. Additionally, the respective contributions are expressed in terms of a percentage. The red and black arrows present the excitations of spin-down and spin-up electrons, respectively. The figure is adapted from Ref. [68].

the  $3d_{x^2-y^2}$ ,  $3d_{3z^2-r^2}$ ,  $3d_{xy}$ ,  $3d_{xz}$  and  $3d_{yz}$  orbitals which are labeled as  $|3d_i\rangle$ . Following Equation (3.30), we can calculate the total absorption as:

$$\int_{L_j} \mu_\alpha(\omega) d\omega \propto \sum_i \sum_{m_j} |\langle 2p_{j,m_j} | \mathbf{r} \cdot \mathbf{e}_\alpha | 3d_i \rangle|^2 \underline{n}_i \propto \sum_i P_{i,\alpha} \underline{n}_i \quad (3.39)$$

where  $L_j$  denotes the transition edges  $L_3$  and  $L_2$ ,  $\underline{n}_i$  is the hole density in each  $3d$ -orbital and  $P_{i,\alpha}$  represents the transition probability for a given polarization,  $\alpha$ . These transition probabilities have been quantified for linear polarizations along the  $x$ ,  $y$  and  $z$  axes in Refs. [67, 69]. Using these values of  $P_{i,\alpha}$ , Equation (3.39) yields the so-called charge distribution sum-rules:

$$\int_{L_3+L_2} \mu_x d\omega = C[6(\underline{n}_{xy} + \underline{n}_{xz} + \underline{n}_{x^2-y^2}) + 2\underline{n}_{3z^2-r^2}] \quad (3.40a)$$

$$\int_{L_3+L_2} \mu_y d\omega = C[6(\underline{n}_{xy} + \underline{n}_{yz} + \underline{n}_{x^2-y^2}) + 2\underline{n}_{3z^2-r^2}] \quad (3.40b)$$

$$\int_{L_3+L_2} \mu_z d\omega = C[6(\underline{n}_{xz} + \underline{n}_{yz}) + 8\underline{n}_{3z^2-r^2}] \quad (3.40c)$$

where  $C$  is a proportionality constant. As can be seen, from Equations (3.40), the hole occupancy of each  $3d$ -orbital contributes to the linear polarization dependent XAS. However, if the sample is magnetic, the XAS is subject to further modifications, which is known as the x-ray magnetic linear dichroism. This is due to the magnetism induced time-reversal symmetry breaking of the Kramers doublets, as discussed in Ref. [70].

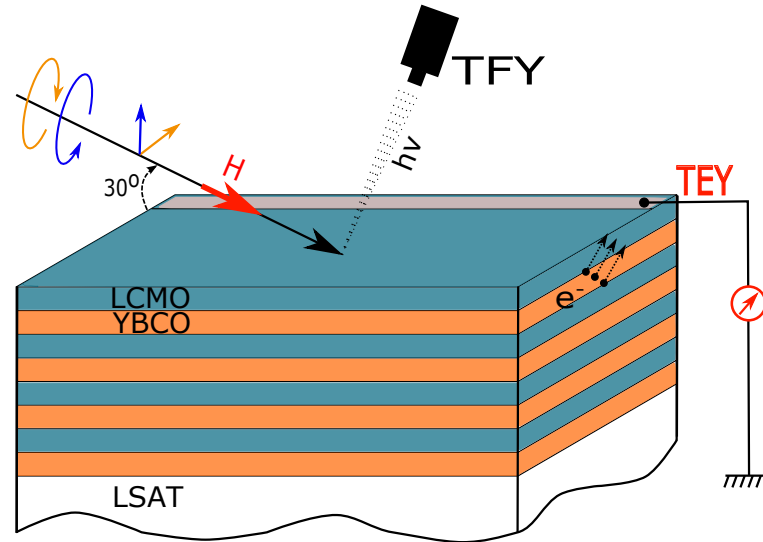


Figure 3.10: Sketch showing a YBCO/LCMO multilayers and a basic setup for XMCD and XLD experiments in TEY and TFY modes. The magnetic field, as marked by a red arrow, is applied along the x-ray propagation vector which is at  $30^\circ$  grazing incidence with respect to the sample surface. The fluorescence detector is placed on the scattering plane at  $90^\circ$  angle with respect to the x-ray propagation vector. The sample is grounded via a current meter which detects the TEY signal.

### 3.6.4 Setting up a XAS experiment

The XAS measurements have been performed at the XTtreme beamline of the Swiss Light Source at the Paul Scherrer Institute in Switzerland. Figure 3.10 illustrates a basic XAS experiment with linear and circular polarized x-rays. The x-ray absorption profiles were measured indirectly by probing the decay process of the excited ions. In the decay process, an excited electron from the valence state returns to the empty core level by releasing its excess energy. This excess energy either ejects an Auger electron from the atom or emits a photon via a fluorescence process. In practice both processes happen simultaneously.

The Auger electrons inelastically scatter in the sample and generate a cascade of secondary electrons. If the excited ion sits close to the sample surface, the secondary electrons may just have sufficient kinetic energy to leave the sample. Subsequently, the sample gets positively charged. If the sample is grounded, the net electron flow to the sample gives rise to a measurable electric current which is usually in the range of pico-ampere. The intensity of the current is proportional to the number of excited ions per unit time. This mode of measuring the x-ray absorption profiles is known as the so-called total electron yield (TEY). As the secondary electrons strongly scatter with the lattice, their escape probability drops exponentially with the depth from the sample surface. Therefore, the TEY mode is rather surface sensitive.

Simultaneously, one can detect the emitted fluorescence photons by placing a diode close to the sample. This method of recording absorption profiles is known as the total fluorescence yield (TFY). Since the scattering cross section of photons with the lattice is significantly smaller, the fluorescence photons can escape from the depth of the sample. The TFY mode thus serves as a bulk-sensitive probe.

## Chapter 4

# Magnetic proximity effect in YBCO/LCMO multilayers

In this chapter, we discuss about how the magnetic exchange interaction between the interfacial Cu and Mn moments in  $\text{YBa}_2\text{Cu}_3\text{O}_7/\text{La}_{2/3}\text{Ca}_{1/3}\text{MnO}_3$  (YBCO/LCMO) multilayers (MLs) can be modified. Section 4.1 describes the pulsed laser deposition of YBCO/LCMO MLs under three different growth conditions. These different types of MLs are labeled as YL\_1, YL\_2 and YL\_3. The MLs for YL\_1 and YL\_2 contain ten repetitions of the YBCO/LCMO bilayer. The type YL\_3 consists of a single bilayer. Section 4.2 details their structural characterization using x-ray diffraction. It confirms the impurity-free epitaxial growth of these MLs that are grown on (001)-oriented  $\text{Sr}_{0.7}\text{La}_{0.3}\text{Al}_{0.65}\text{Ta}_{0.35}\text{O}_3$  (LSAT) substrates. Scanning transmission electron microscopy and electron energy loss spectroscopy studies of YL\_2 are discussed in section 4.3. Rutherford backscattering studies which quantify the stoichiometry of the LCMO layers are summarized in section 4.4. Section 4.5 details the transport and magnetic properties of the samples, especially with respect to the different conductivities of the LCMO layers in YL\_1 and YL\_2 and the weakly ferromagnetic properties of YL\_3. The analysis of the optical data in section 4.6 provides evidence for the formation of orbital polarons in YL\_2. Section 4.7 summarizes the polarized neutron reflectometry study of YL\_2 ML which shows that, unlike in YL\_1, the ferromagnetic order of the Mn moments near the interfaces is weakly suppressed. Section 4.8 details the x-ray linear dichroism and x-ray magnetic circular dichroism studies on the Cu and Mn ions. From the former we determine the  $3d$ -orbital occupancy of the ions, and from the latter the magnetism of the ions. Finally, we discuss and interpret the various experimental results in section 4.9.

### 4.1 Growth parameters

Three different kinds of YBCO/LCMO MLs (YL\_1-3) have been grown on (001)-oriented LSAT substrates using pulsed laser deposition (PLD). The *layer-by-layer* growth mode and the overall layer thickness have been monitored with *in-situ* reflection high energy electron diffraction (RHEED) as described in Ref. [71]. The growth and the annealing conditions have been chosen to obtain a fully oxygenated state and thus a reasonably high superconducting critical temperature of the YBCO layers, but to alter the stoichiometry and the oxygen content of the LCMO layers.

For all samples, we preheated the LSAT substrates to  $825^\circ\text{C}$  in 0.34 mbar of  $\text{O}_2$  for 30 minutes prior to the depositions in order to cure the mechanically polished surface.

The YL\_1 sample with 10 bilayers has been grown following a similar procedure as described in Ref. [71]. The YBCO(9.7 nm) and LCMO(9.4 nm) layers were grown with  $P_{\text{O}_2} = 0.34$  mbar, a laser fluence of  $2.4 \text{ J/cm}^2$ , and a repetition rate of 7 Hz. After deposition, it was cooled to  $700^\circ\text{C}$  at a rate of  $10^\circ\text{C/min}$  while the oxygen partial pressure was gradually increased to 1 bar. Subsequently, the sample was cooled to  $485^\circ\text{C}$  at a rate of  $30^\circ\text{C/min}$  where it was kept for one hour. The temperature was then slowly decreased to room temperature before it

was removed from the PLD chamber. To ensure a full oxygenation of the YBCO layers, we performed an *ex-situ* annealing at 485 °C in a continuous flow of O<sub>2</sub> for 12 hours.

The samples of type YL<sub>2</sub> have been grown with 1, 6 and 10 bilayer for which the thicknesses of the YBCO and LCMO layers are 9.5 nm and 9.1 nm, respectively. These samples have been protected with a capping layer of about 1.5 nm of LaAlO<sub>3</sub> (LAO). Different O<sub>2</sub> partial pressures of 0.34 mbar and 0.12 mbar have been used during the growth of the YBCO and LCMO layers, respectively. The laser fluence was kept at 2.0 J/cm<sup>2</sup> and the repetition rate at 2 Hz. The *in-situ* cooling and annealing procedure was the same as for YL<sub>1</sub>, except for a lower cooling rate of only 10 °C/min (instead of 30 °C/min for YL<sub>1</sub>) to 485 °C. No post annealing was performed as the YBCO layers grown at this lower laser repetition rate were already fully oxygenated. Though, the YL<sub>2</sub> type MLs were grown with 1, 6 or 10 bilayer repetitions, but in the following data are only shown for the ML with 10 bilayer repetitions.

Sample YL<sub>3</sub> consists of a single bilayer with about 19 nm of YBCO and 5 nm of LCMO. It is protected with a LAO capping layer of 1.5 nm thickness. It was grown with the same PLD parameters as YL<sub>2</sub>. The only difference concerns the *in-situ* annealing procedure for which the cooling from 700 °C to 485 °C was done at a faster rate of 30 °C/min. No *ex-situ* annealing was performed for this sample.

## 4.2 Structural characterization

The structural characterization of the samples has been performed with the x-ray diffraction technique. The measurements were carried out using a Rigaku SmartLab triple-axis diffractometer with a 9 kW Cu-K<sub>α</sub> ( $\lambda = 1.54 \text{ \AA}$ ) radiation source. Figure 4.1 displays typical diffraction patterns and reciprocal space maps of YL<sub>2</sub> and YL<sub>3</sub>. Details about the structural characterization of YL<sub>1</sub> can be found in section 3.1 of Ref. [69]. The diffraction patterns in Figure 4.1a were obtained using a symmetric scan mode, i.e., by maintaining  $2\theta = 2\omega$  such that the momentum transfer is along the surface normal of the sample. The presence of only (00N) peaks indicates that the samples are epitaxial with the c-axis perpendicular to the surface. We did not identify any signal from other phases or impurities. In the diffraction pattern of YL<sub>2</sub>, an intensity oscillation can be found around the highly intense Bragg's peaks. This is due to the interference of the reflected waves from the surface and substrate of the ML. From the period of these intensity oscillations one can deduce the total thickness of these ML samples. It also testifies the high quality of the interfaces and their low roughness. This type of oscillation is also present, but less prominent in YL<sub>3</sub> for which larger thickness (19 nm) of YBCO gives rise to larger interface roughness. For all the samples, we are not able to isolate the LCMO (00N) peaks from the (00N) peaks of LSAT. This is because the lattice mismatch between the pseudocubic lattice parameters of bulk LSAT and LCMO is only 0.1 %. The calculated c-axis lattice parameter of YBCO for both samples is 11.71(7) Å. The c-axis lattice parameter of YBCO in YL<sub>1</sub> is also 11.71(2) Å [69]. The measured c-axis lattice parameter is slightly larger than the reported value (11.6757(4) Å) for bulk YBCO [51]. Such an elongation of the c-axis lattice parameter can be understood in terms of slightly compressive strain from the LSAT substrate (and the LCMO layers).

All the YBCO, LCMO and LSAT (01N) peaks in the reciprocal space maps are almost symmetric around the white lines ( $k=1$ ). This finding confirms the almost fully strained epitaxial growth of the MLs YL<sub>2</sub> and YL<sub>3</sub>. Thus, the components of the MLs achieve similar in-plane lattice parameter. Due to very similar pseudocubic lattice parameters of LSAT and LCMO, their (013) peaks are hardly separable. The calculated in-plane lattice parameter of YBCO is 3.8491(15) Å and 3.8595(10) Å, respectively, for YL<sub>2</sub> and YL<sub>3</sub>. For YL<sub>1</sub>, it is 3.867(5) Å. The reported value of in-plane lattice parameter for bulk YBCO is 3.8851 Å [51]. It indicates a slight compression of the in-plane lattice parameter of YBCO in these MLs, and thus explains the elongation of the c-axis lattice parameter. As marked by the black arrows in Figure 4.1b, the intensity modulation along  $Q_z$  is observed around the LSAT(013) peak for YL<sub>2</sub>.

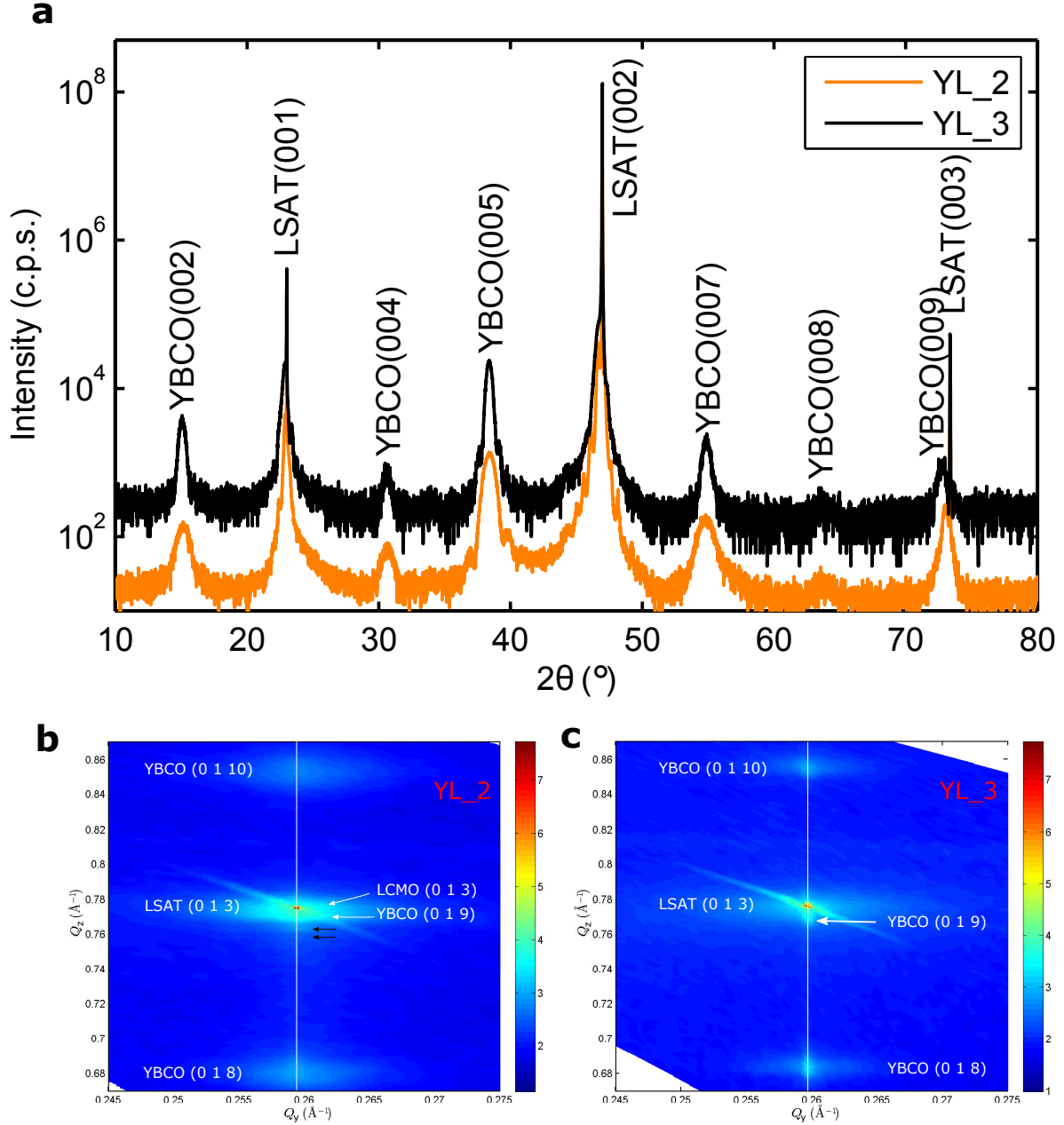


Figure 4.1: (a) Symmetric  $\theta$ - $2\theta$  x-ray diffraction patterns of YL\_2 and YL\_3 along the [00L] direction. Reciprocal space maps of (b) YL\_2 and (c) YL\_3 around the (013) Bragg peak of the pseudocubic LSAT substrate. The black arrows in (b) indicate the intensity oscillation which is related to the total thickness of the multilayer.

### 4.3 Scanning transmission electron microscopy

Cross-section high-resolution scanning transmission electron microscopy (STEM) observations of a YL<sub>2</sub> type sample were carried out in an aberration-corrected JEOL JEM-ARM200cF, operated at 200 kV and equipped with a cold field emission gun and a Gatan quantum electron energy-loss spectrometer (EELS). The convergence semi-angle was around 35 mrad, while the collection semi-angle was 28 mrad, approximately. The specimens were prepared by conventional methods of grinding and Ar-ion milling. Random noise in the EELS data was removed by means of principal component analysis [72]. EELS elemental mapping was performed by integrating the signals under the characteristic elemental edges after background subtraction using a power law. The integration windows were typically around 20-30 eV wide.

STEM-EELS images show coherent, epitaxial interfaces (see Figure 4.2, left panel). Occasional defects are present such as double CuO chain layers or one unit cell interface steps giving rise to anti phase boundaries, all of these being typical defects observed in YBCO. The CuO chain layers are easily identifiable in the high resolution Z-contrast images due to their slightly darker contrast [32, 73]. In most cases, the interfaces are found to be symmetric. Regardless of top or bottom relative positions, the dominant atomic plane stacking found is such that a manganite MnO<sub>2</sub> plane faces a cuprate BaO plane, as shown by the EELS profiles such as the ones in Figure 4.2 (right panel).

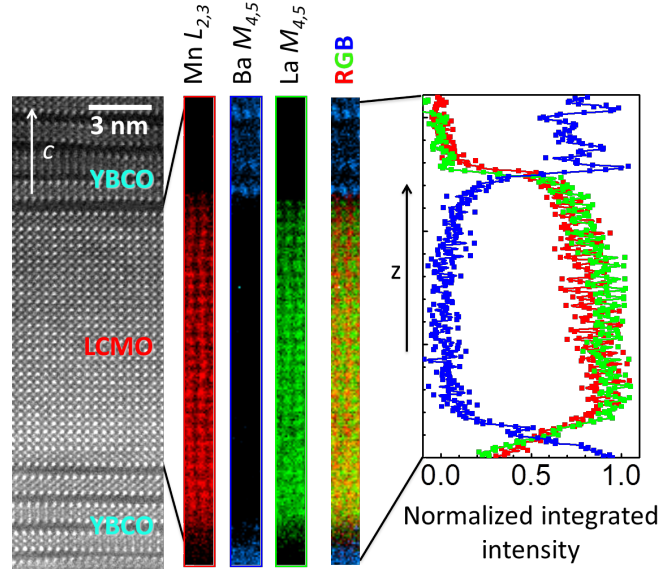


Figure 4.2: Left panel: Atomic resolution, Z-contrast high angle annular dark field image of the YBCO/LCMO/YBCO stacking in a YL<sub>2</sub> type sample. Right panel: Elemental maps obtained from the analysis of the Mn  $L_{2,3}$  (red), Ba  $M_{4,5}$  (blue) and La  $M_{4,5}$  (green) absorption edges). An RGB overlay of the three maps, along with a line profile on a matching color scale of the normalized integrated intensities is also shown. Some spatial drift is visible.

### 4.4 Rutherford backscattering

Rutherford backscattering (RBS) measurements were performed to determine the stoichiometry of the LCMO layers in YL<sub>1</sub> and YL<sub>2</sub> MLs. The experiment was carried out at the 6 MV tandem accelerator of the Laboratory of Ion Beam Physics at ETH Zurich using a 2 MeV <sup>4</sup>He beam and a silicon PIN diode detector under a backscattering angle of 168° [74]. We measured two different types of LCMO films that were grown under the same conditions as the LCMO layers of MLs YL<sub>1</sub> and YL<sub>2</sub>. To be most suitable for the RBS measurements, these LCMO films are 100 nm thick and grown on (001)-oriented MgO substrates. We chose MgO substrate because it contains only light elements for which the RBS signal does not overlap

with the one from the film (except for the oxygen signal). The experimental data, displayed in Figure 4.3 have been analyzed with the RUMP code [75]. The obtained stoichiometry of the LCMO samples is listed in Table 4.1.

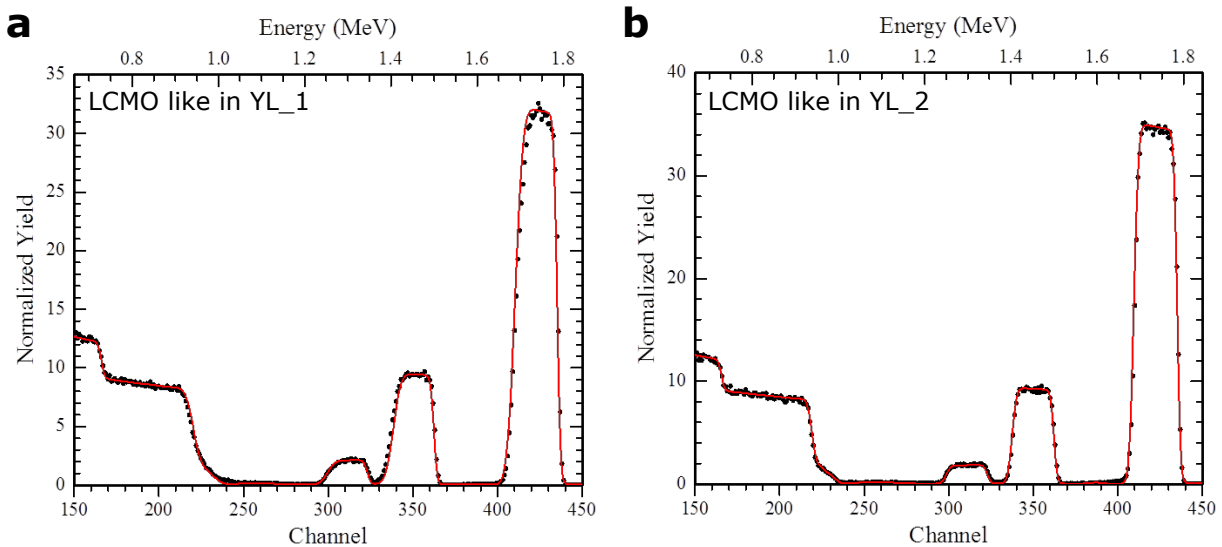


Figure 4.3: RBS spectra (symbols) for the LCMO samples grown under the same conditions as in (a) YL.1 and (b) YL.2. The red lines show the best fits to the spectra.

Samples	La	Ca	Mn	O
LCMO like in YL.1	0.66	0.34	0.98	3.05
LCMO like in YL.2	0.71	0.29	0.95	2.95

Table 4.1: Stoichiometry of 100 nm thick LCMO films grown under the same conditions as in YL.1 and YL.2.

The results indicate that the LCMO of type YL.2 has a significant deficiency of Ca, Mn and O. Subsequently, the Ca and O deficiency results in a reduced hole content in the LCMO layers of YL.2 as compared to the more or less stoichiometric LCMO layers of type YL.1. The reduced hole content and the Mn deficiency both can diminish the conductivity of the LCMO layers [54] as is indeed found in section 4.5. Note that the uncertainty of the content of the heavier elements, like La, Ca, and Mn, is 1-3%, whereas for oxygen it is up to 5%.

## 4.5 Transport and magnetization

We have determined the transport properties of the samples by measuring their resistance and magneto-resistance (MR) with a Physical Properties Measurement System from Quantum Design (QD-PPMS). We used a four probe method with the wires glued with silver paint to the corners of the sample surface. We applied a current of  $10 \mu\text{A}$  and recorded the voltage at different temperatures and/or fields. Figure 4.4a depicts the resistance vs. temperature (R-T) characteristics. The resistance has been normalized with respect to the corresponding value at 300 K. In all cases, we recorded the voltage while cooling down in zero field from 300 K to 10 K at a rate of 2 K/min. For all three samples, the onset of the superconducting transition around 85 K is evident from a sharp drop of the resistance. The resistances become zero below about 70-75 K which in the following is quoted as the superconducting transition temperature ( $T_C$ ). The high  $T_C$  values and reasonably sharp transitions in the thin film heterostructures indicate that the doping of the YBCO layers is rather closed to the optimum level. Since they are connected in parallel, both the YBCO and the LCMO layers contribute to the in-plane resistance. The measured resistance is therefore dominated by the layer that is more metallic

(or even superconducting). In this context, it is an interesting observation that a kink in the R-T curve around the ferromagnetic transition of the LCMO layers is only seen for YL\_1 (around 215 K) but not for YL\_2. This kink arises from the insulator-to-metal crossover in LCMO that accompanies its paramagnet-to-ferromagnet transition. Its absence in YL\_2 is therefore a clear indication that the conductivity of the LCMO layers is significantly lower than the one of the YBCO layers. For YL\_3, the thick ( $\approx 19$  nm) YBCO layer dominates the transport data due to its high metallicity. As the LCMO layer in this bilayer is only 5 nm thick, we do not expect to see insulator-to-metal transition. Additional information about the different metallic properties of the LCMO layers can be obtained from the MR measurements of YL\_1 and YL\_2 as shown in Figure 4.4b. The resistances were measured while sweeping the field (parallel to the ab-plane) from +9 T to -9 T at 150 K with 100 Oe/sec rate. The much smaller MR of YL\_2 confirms that its LCMO layers are less conducting than the ones in YL\_1.

The corresponding magnetic properties have been determined with temperature and field dependent magnetization measurements (M-T and M-H curves) using the Vibrating Sample Magnetometer option of the QD-PPMS. Figure 4.5a displays the MT data of the samples YL\_1-3. The data were acquired during field cooling at a rate of 2 K/min in 0.1 T applied parallel to the sample surface. For YL\_1, a high Curie temperature of  $T^{Curie}=215$  K is observed that agrees with the value that has been deduced from the kink in the resistance (see above). The estimated value of the low temperature magnetization of the sample amounts to about  $2.0 \mu_B/\text{Mn-ion}$ . For YL\_2 the magnetic transition is somewhat lower at  $T^{Curie}=180$  K. On the other hand, the low temperature magnetization value is somewhat higher with  $2.5 \mu_B/\text{Mn-ion}$ . Finally, for YL\_3, there is no clear ferromagnetic transition discernible from the M-T curve. The rather small low temperature value of the magnetization of about  $0.25 \mu_B/\text{Mn}$  suggests that the LCMO in this bilayer is hardly ferromagnetic. To confirm that the suppression of the ferromagnetic order is due to the reduced LCMO layer thickness, we grew a bilayer with a 10 nm thick LCMO layer under identical conditions and found that it has an average magnetization comparable to the one of YL\_1 and YL\_2, albeit with a reduced value of  $T^{Curie} \approx 150$  K. A similar threshold effect of the ferromagnetic properties depending on the thickness of the manganite layers has been reported in Ref. [76].

For the M-H loops depicted in Figure 4.5b, the data were recorded at 80 K after cooling the samples in a field of 9 T that was applied along the ab-plane of the samples. The shape of the M-H loops of YL\_1 and YL\_2 confirms the presence of a strong ferromagnetic order in the LCMO layers. To the contrary, for YL\_3, the M-H loop has an unusual shape with no sign of saturation at high fields and a very large range of the hysteresis. This may be understood in terms of ferromagnetic regions (clusters) that are embedded into an antiferromagnetic matrix. The interaction between these two phases results in spin frustration and a glassy state that can account for the observed hysteresis effects up to 0.3 T.

## 4.6 Optical spectroscopy and ferromagnetic polarons

The optical conductivity of the MLs YL\_1 and YL\_2 have been measured to access the dynamical response of the free charge carriers, and especially, their conduction mechanism in the ferromagnetic (FM) LCMO layers. The measurements were performed using spectroscopic ellipsometry technique. The data in the near-infrared to ultraviolet (0.5-6.5 eV) range were obtained with a commercial ellipsometer (Woollam VASE) equipped with an ultra-high vacuum liquid He-flow cryostat. For the far-infrared and mid-infrared regions, a home-built setup [77] attached to a Bruker 13 v FTIR spectrometer was used. The substrate contribution was corrected with the Woollam VASE software [78].

Figure 4.6 shows the spectra of the real part of the optical conductivity,  $\sigma_1$  of YL\_1, YL\_2 and a corresponding ML with  $\text{LaMnO}_{3+\delta}$  (LMO), that were measured at 10 K and near  $T^{Curie}$  of the individual MLs. From these spectra, we derived the the temperature difference spectra,  $\Delta\sigma_1(\omega)$  that is displayed in Figure 4.7. The detail growth and characterization of the YBCO/LMO ML are described in Ref. [27]. The LMO layers of this ML are weakly doped

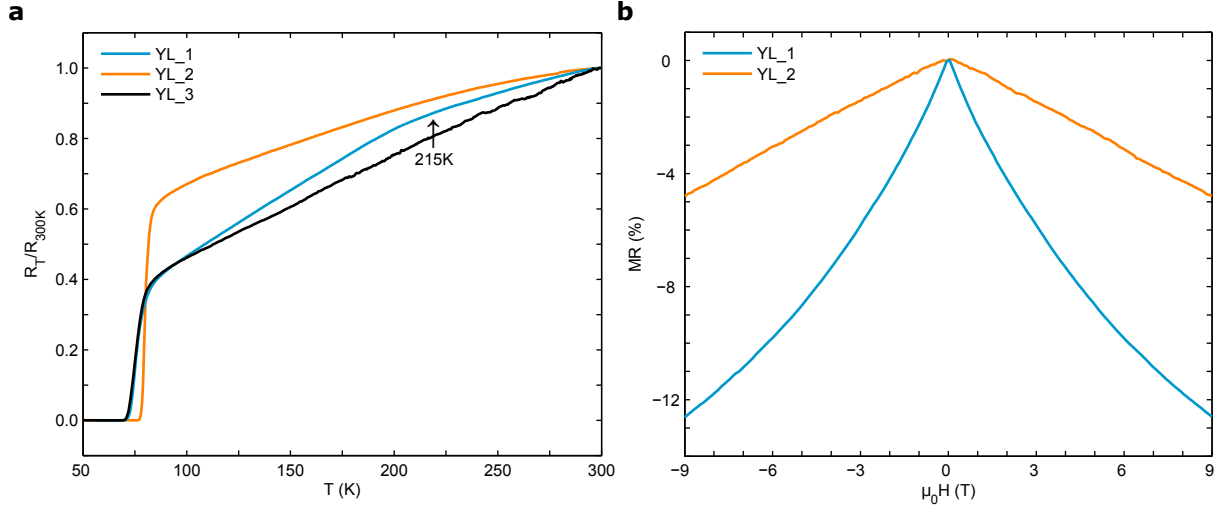


Figure 4.4: (a) In-plane resistance vs. temperature curves of the samples YL\_1-3 in zero field. (b) Magneto-resistance,  $\frac{R(H)-R(0)}{R(0)}$  characteristics of YL\_1 and YL\_2 at 150K.

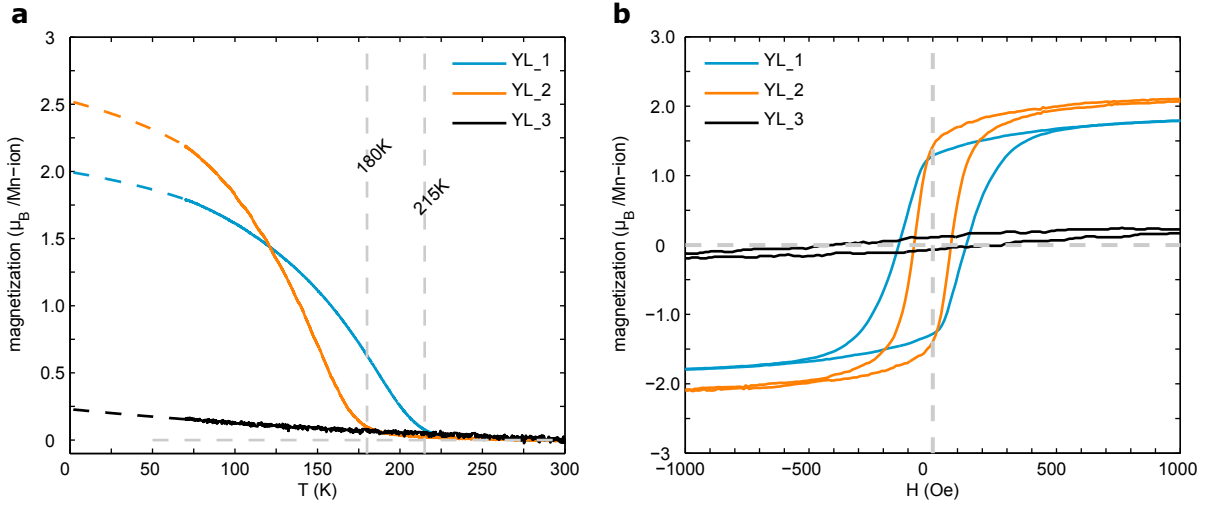


Figure 4.5: (a) Temperature dependence of the field cooled magnetization in 0.1 T for MLs YL\_1-3. The data below about 70 K have been omitted since they are strongly affected by vortex pinning and related avalanche effects that lead to a macroscopic inhomogeneity of the magnetization. Instead, we extrapolated the magnetization curves according to  $M = M_S \left( \frac{T^{Curie} - T}{T^{Curie}} \right)^\gamma$  as shown by the dashed lines. (b) M-H loops for samples YL\_1-3 at 80 K measured after field cooling at 9 T

by cation and oxygen vacancies, and thus are in the insulating ferromagnetic (I-FM) state. For YL\_1, it is evident that the ferromagnetic transition gives rise to a large increase of the Drude response that is centered at zero-frequency in the difference spectra. This characteristic change is a hallmark of the concomitant insulator-to-metal and paramagnet-to-FM transition of LCMO [79]. In YL\_2 this increase of the Drude-response below  $T^{Curie}$  is significantly weaker. This underlines the finding from the transport data, that the LCMO layers in YL\_2 are less metallic than the ones in YL\_1. More interestingly, for YL\_2, a significant fraction of the spectral weight accumulates in a mid-infrared (MIR) band (shown by a blue rectangular box in Figure 4.7). Such an effect is well known from the bulk manganites in the underdoped regime close to the I-FM state where the charge carriers start to form FM polarons [79]. The emerging MIR band in YL\_2 is thus a fingerprint of such FM polarons.

According to R. Killian *et al.* [56], a FM polaron is associated with a local orbital order [56] with an alternating occupation of the  $3d-e_g$  orbitals ( $|3z^2 - r^2\rangle$ ,  $|3x^2 - r^2\rangle$ , and  $|3y^2 - r^2\rangle$ ) of the  $Mn^{3+}$  ions, as shown in Figure 4.8a. According to this orbital arrangement, electrons can hop between the  $Mn^{3+}$  and  $Mn^{4+}$  ions via  $90^\circ$ -superexchange mechanism and thus satisfy the condition of double exchange interaction [55]. In this way, the orbital polaron order gives rise to a FM state. As in an ordered polaron lattice, the electrons can not migrate from one polaron to another, this leads toward an insulating state. A sketch of the orbital order due to such a polaron lattice is shown in Figure 4.8b.

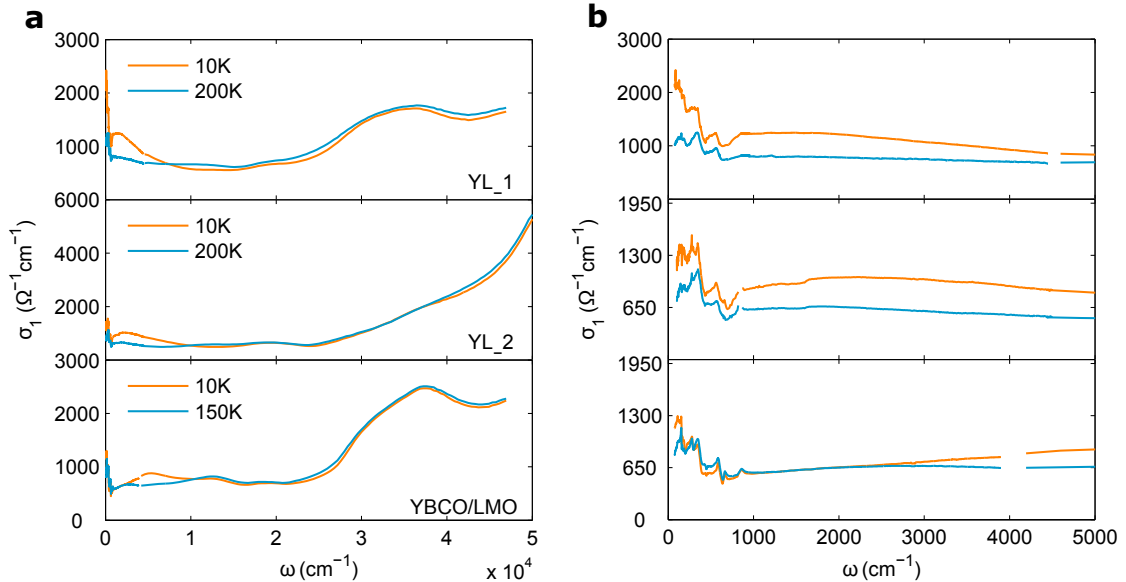


Figure 4.6: (a) Spectra of the real part of the optical conductivity of the MLs YL\_1, YL\_2 and YBCO/LMO. (b) Magnification of the low-energy part of  $\sigma_1$ .

## 4.7 Polarized neutron reflectometry

In this section, we discuss the polarized neutron reflectometry (PNR) measurements on YL\_2.

### 4.7.1 Structural depth profile

First, we have analyzed the neutron reflectometry data acquired at room temperature (RT) to obtain the structural parameters of the ML. Since the sample is not ferromagnetic at 300 K, the reflectivity curve only depends on the nuclear potential of the sample. Figure 4.9 displays the RT reflectivity curve. It contains a set of superlattice Bragg peaks (SLBPs), and Kiessig fringes between the total reflection edge and the 1st order SLBP. The Kiessig fringes arise from the interference of the reflected neutron waves from the substrate surface and the topmost

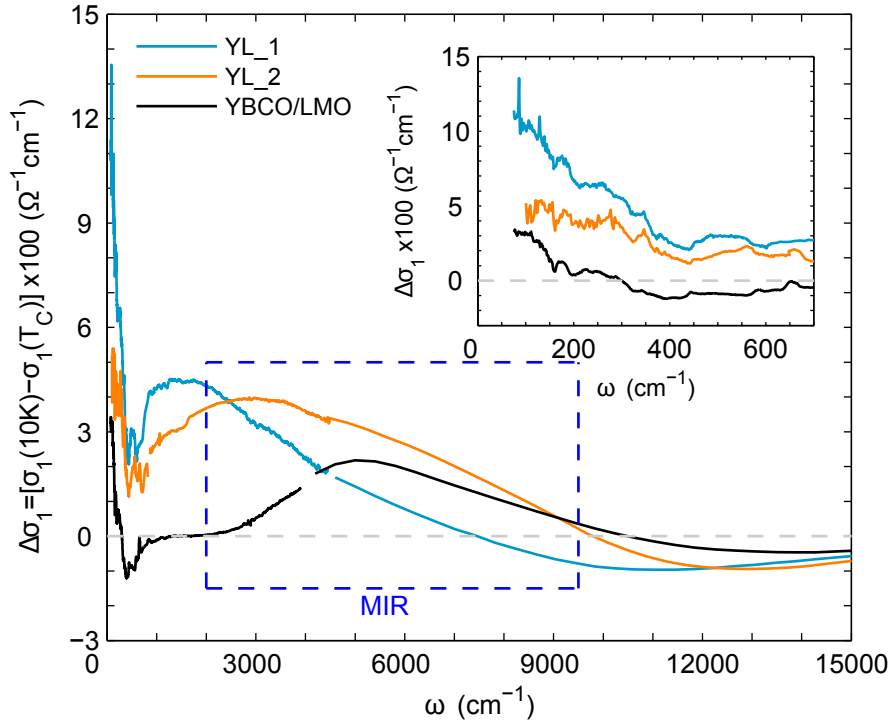


Figure 4.7: Difference spectra of the optical conductivity,  $\Delta\sigma_1(\omega) = \sigma_1(\omega, 10K) - \sigma_1(\omega, T \approx T^{Curie})$  of the MLs YL\_1, YL\_2 and YBCO/LMO. For the latter the strongly pinned orbital polarons give rise to a pronounced MIR band with a maximum around 5000  $\text{cm}^{-1}$ . The inset magnifies the low energy part of  $\Delta\sigma_1$ .

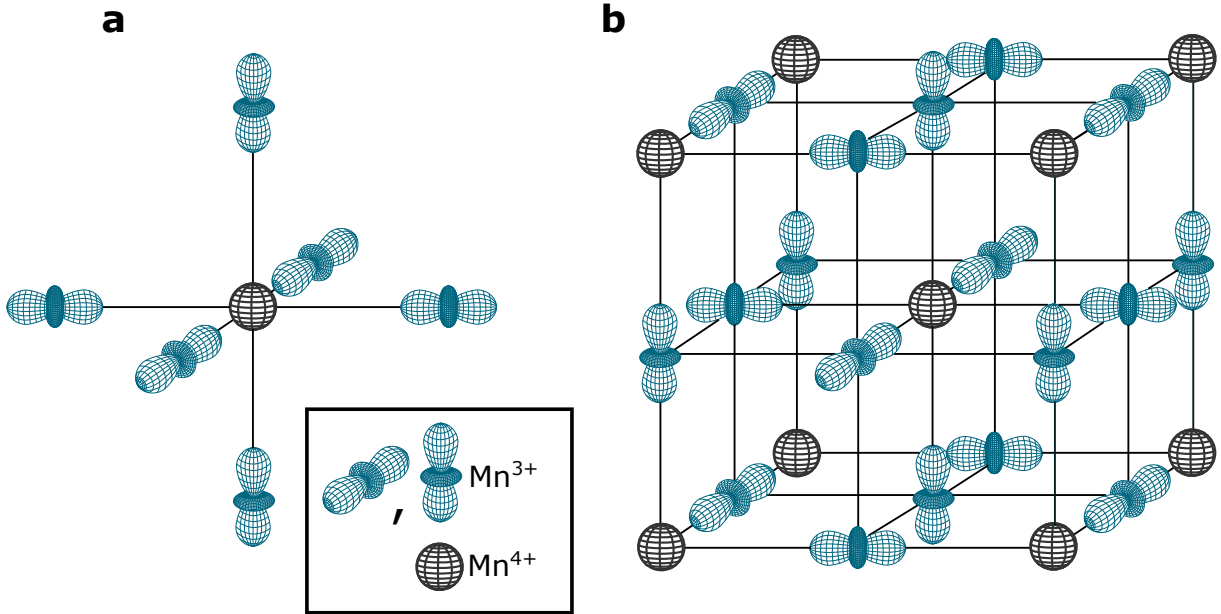


Figure 4.8: (a) Sketch of an orbital polaron showing alternately occupied  $e_g$ -orbitals ( $|3z^2 - r^2\rangle$ ,  $|3x^2 - r^2\rangle$ , and  $|3y^2 - r^2\rangle$ ) of  $\text{Mn}^{3+}$  ions with a  $\text{Mn}^{4+}$  ion at the center. (b) Schematic diagram of an orbital polaron lattice with 25% doping, i.e.,  $\text{La}_{1.75}\text{Ca}_{0.25}\text{MnO}_3$ .

film surface of the ML, i.e., the interface between the LAO capping layer and the ambient. Therefore, it contains the information about the total thickness of the ML. The total thickness of the film thus can be deduced from the period of the oscillation according to:

$$d_{tot} = \frac{2\pi}{\Delta q_{z,kiessig}} \quad (4.1)$$

where  $d_{tot}$  and  $\Delta q_{z,kiessig}$  are the total thickness of the ML and the period of the Kiessig oscillation, respectively. The SLBPs arise from the constructive interference of the neutron waves reflected from every interface of the ML. According to the Bragg's condition, it has the following relationship with the thickness of the YBCO/LCMO bilayers:

$$2d_{bl} \sin \theta = n\lambda \quad (4.2)$$

where  $d_{bl}$  is the thickness of a bilayer,  $\theta$  the angle of incidence,  $n$  an integral number which determines the order of the SLBPs and  $\lambda$  the wavelength of the neutrons. One can deduce the bilayer thickness from the separation of two consecutive SLBPs in  $q_z$ . Additionally, the intensity and the width of the SLBPs contain the information about the contrast between the nuclear potential of the individual layers and about the variation of the thickness of the individual YBCO and LCMO layers. The strong suppression of the intensity at the 2nd order SLBP position indicates that the YBCO and LCMO layers have similar thicknesses; this is true for all even order SLBPs. This can be understood in terms of a destructive interference effect due to the  $\pi$ -*phase* shift between the neutron waves that are reflected from the YBCO/LCMO and LCMO/YBCO interfaces. The  $\pi$ -*phase* shift arises because step-like changes of the potential have opposite signs at these two interfaces. This phase shift is independent of the optical path traversed by the neutron waves. In an ideal case where the thicknesses of the YBCO and LCMO layers are identical, the path difference between the interfered neutron waves from the YBCO/LCMO and LCMO/YBCO interfaces at the 2nd or any even order SLBP is exactly  $\lambda$ . This results in a phase difference of  $2\pi$  in addition to the aforementioned  $\pi$ -*phase* shift [80]. The total  $3\pi$  phase difference gives rise to the destructive interference of the neutron waves, and thus the absence of the 2nd or even order SLBPs. Any deviation from the ideal case can cause a non-vanishing intensity at the even order SLBP positions. Additional information about the roughness of the sample can be obtained from the decay profile of the reflectivity curve over  $q_z$ . The roughness leads to a decay that is faster than the usual  $q_z^{-4}$  law.

To know the values of the structural parameters in detail, we fitted the RT neutron and x-ray reflectivity curves simultaneously using the GenX software [81]. We performed a simultaneous fitting of the neutron and x-ray reflectivity curves to reduce the uncertainty in the values of the structural parameters. To decrease the number of free parameters in fitting, we have assumed that all the YBCO and LCMO layers are identical. The thickness, roughness and density (formula unit/unit cell volume) of the layers were used as common parameters for both reflectivity curves; but the instrumental parameters like resolution, background, offset, etc. were independent. The best fits are shown by the solid lines in Figure 4.9 which describes the experimental data (symbols) rather well. The summary of the obtained values of the nuclear scattering length density, thickness and roughness of the individual layer is listed in Table 4.2. The thicknesses correspond to approximately 8 and 23 unit cells of YBCO and LCMO, respectively. The calculated roughness of the YBCO/LCMO and LCMO/YBCO interfaces are quite similar to the roughness of the corresponding monolayers that were grown on bare LSAT substrates, respectively.

### 4.7.2 Magnetic depth profile

The polarized neutron reflectivity (PNR) curves have been measured at 5 K with a magnetic field of 0.1 T applied along the ab-plane of the sample. At  $5 \text{ K} \ll T^{Curie} = 180 \text{ K}$ , LCMO layers are strongly ferromagnetic, and in 0.1 T they are almost fully magnetized as can be seen

	$\rho_n(10^{14} \text{ m}^{-2})$	$d$ (nm)	$\sigma$ (nm)
YBCO	4.74(8)	9.47(10)	1.40(10)
LCMO	3.90(6)	9.06(10)	0.50(10)
LAO	6.48(11)	1.50(20)	1.00(10)
LSAT	5.25(2)	-	-

Table 4.2: Nuclear scattering length density ( $\rho_n$ ), thickness ( $d$ ) and roughness ( $\sigma$ ) of the YBCO, LCMO and LAO layers as obtained from the simultaneous fitting of the neutron and x-ray reflectivity curves at room temperature. For the substrate (LSAT), no roughness was considered.

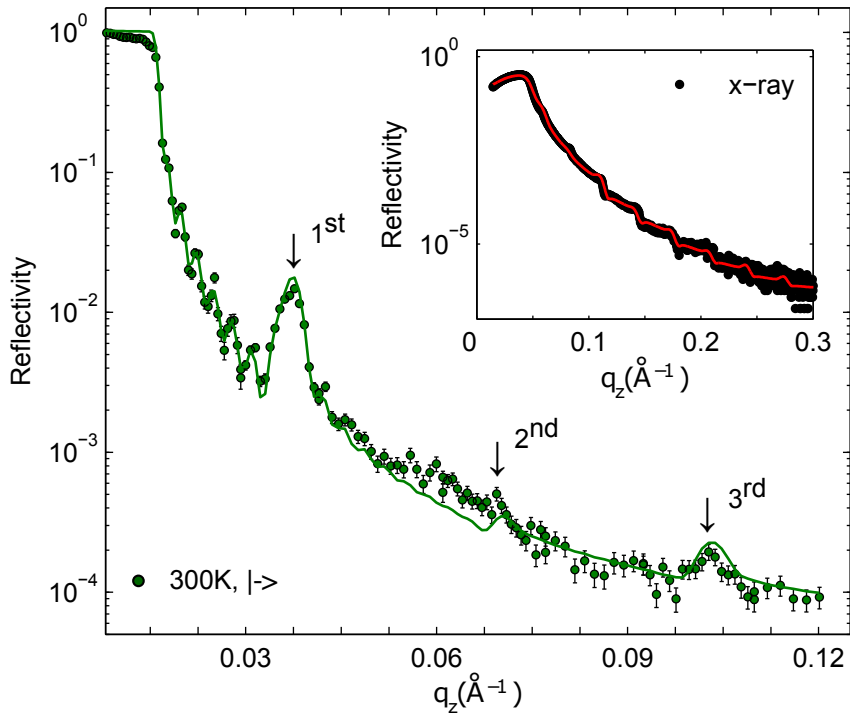


Figure 4.9: Room temperature neutron reflectivity curve vs.  $q_z$  for YL<sub>2</sub>. The arrows indicate the position of the superlattice Bragg peaks. The solid line is the best fit to the data. The inset depicts the x-ray reflectivity curve vs.  $q_z$  of the same sample. The solid red line represents the best fit to the data.

from the magnetization vs. field loop displayed in Figure 4.5b. In addition to the nuclear potential, neutrons now feel the magnetic potential which arises from the ferromagnetism of the LCMO layers. Depending on the relative orientation of the neutron spins with respect to the magnetization direction, the magnetic potential changes its sign. This results in different reflectivity profiles for spin up ( $|+\rangle$ ) and spin down ( $|-\rangle$ ) neutrons as shown in Figure 4.10. It is evident that the intensity of the reflectivity for spin down neutrons is relatively large. This is because the total (nuclear + magnetic) scattering length density for LCMO decreases (increases) for spin down (up) neutrons, and thus increases (decreases) the contrast between the YBCO and LCMO layers. Furthermore, the 2nd order SLBP gains significant intensity at low temperature, while it was almost absent at room temperature. This is a clear indication that the symmetry of the magnetic potential is reduced as compared to the one of the nuclear potential [22]. The phenomenon had been previously observed in YL<sub>1</sub>. The low temperature PNR data of YL<sub>1</sub> had been modeled using a so-called ‘depleted layer’ model which assumes a suppression of the ferromagnetic order of the Mn moments in the vicinity of the interfaces to YBCO [3, 29]. For YL<sub>2</sub>, we adapted the same model to fit the data.

As in Ref. [3, 29], we used a simple model of block-like potentials with a finite magnetization in the core of the LCMO layers and zero magnetization next to the interfaces. To fit the data, we used the structural parameters obtained from the fitting of the 300 K data and kept them

	$t^{depl}$ (nm) at Y/L	$t^{depl}$ (nm) at L/Y
YL_1	1.32(7)	1.10(7)
YL_2	0.83(10)	0.66(10)
YBCO/LMO	0.43(7)	0.36(7)

Table 4.3: ‘Depleted layer’ thicknesses ( $t^{depl}$ ) at the YBCO/LCMO or YBCO/LMO (Y/L) and LCMO/YBCO or LMO/YBCO (L/Y) interfaces for the MLs YL\_1 [3, 29], YL\_2 and YBCO/LMO [3].

constant while varying only the magnetic parameters, like the average magnetization and ‘depleted layer’ thicknesses ( $t^{depl}$ ). It is noteworthy that the topmost LCMO layer has only one interface with the YBCO. Therefore, we considered that the ‘depleted layer’ only exists in that particular interface. In the other interface with the LAO capping layer, the average magnetization was assumed to be the same as the one of the core. It is known that the LAO layer does not change any oxidation state of the Mn ions at the interface, but protects the LCMO layer from the ambient [82]. We have shown the result of the best fit by the solid lines in Figure 4.10a. The corresponding nuclear and magnetic depth profiles have been displayed in Figure 4.10b. The obtained values of the ‘depleted layer’ thickness,  $t^{depl}$  are 0.8 and 0.7 nm at the YBCO/LCMO and LCMO/YBCO interfaces, respectively. The average magnetization of the core of the buried and topmost LCMO layers turn out to be very similar, i.e.,  $2.65(5) \mu_B/\text{Mn ion}$ .

### 4.7.3 Summary

The PNR measurements on YL\_2 clearly show the presence of a so-called ‘depleted layer’ where the ferromagnetic order of the Mn moments is strongly suppressed. The phenomenon is quite similar to the one that was previously observed in YL\_1 [3, 29], but the magnitude of the effect is a bit weaker for the present YL\_2 sample. A summary of the values of  $t^{depl}$  for YL\_1 and YL\_2 is given in Table 4.3.

Though we have assumed zero magnetization at the interfaces of the LCMO layers, in reality a small but finite magnetization may exist. This is indeed suggested for YL\_1 from a recent x-ray resonant magnetic reflectometry study [30]. The neutron reflectivity measurement, however, is not sensitive to the small moment within the  $q_z$ -range of our measurement. In the present model, a thicker ‘depleted layer’ thus means a stronger suppression of the ferromagnetic order of the Mn moments. By comparing the values of  $t^{depl}$ , we can say that the strongest suppression of the ferromagnetic order occurs in YL\_1 where the LCMO layers are highly conducting as found from the transport measurements and its optical conductivity. On the other hand, the weakest suppression has been observed for the YBCO/LMO ML for which the LMO layers are in the insulating ferromagnetic state [3]. The conductivity of the LCMO layers in YL\_2 stays in between, and so the value of  $t^{depl}$ . This trend clearly suggests that the suppression of the ferromagnetic order in LCMO near to the interfaces depends on the electronic property of the layer.

## 4.8 X-ray absorption spectroscopy

### 4.8.1 Experimental details

We performed the x-ray absorption spectroscopy (XAS) on the samples YL\_1-3 at the XTreme beamline of the Swiss Light Source at the Paul Scherrer Institute at Villigen, Switzerland. Prior to the measurements, the samples were field cooled to 2 K in 6 T applied along the propagation direction of the beam which was at an angle of incidence of  $30^\circ$  with respect to the sample surface.

We measured the x-ray linear dichroism (XLD) at the Cu and Mn  $L_{3,2}$ -edges by switching the linear polarization (in-plane or out-of-plane) of the incoming x-rays. Multiple measurements for each polarization were made to enhance the signal to noise ratio and to check

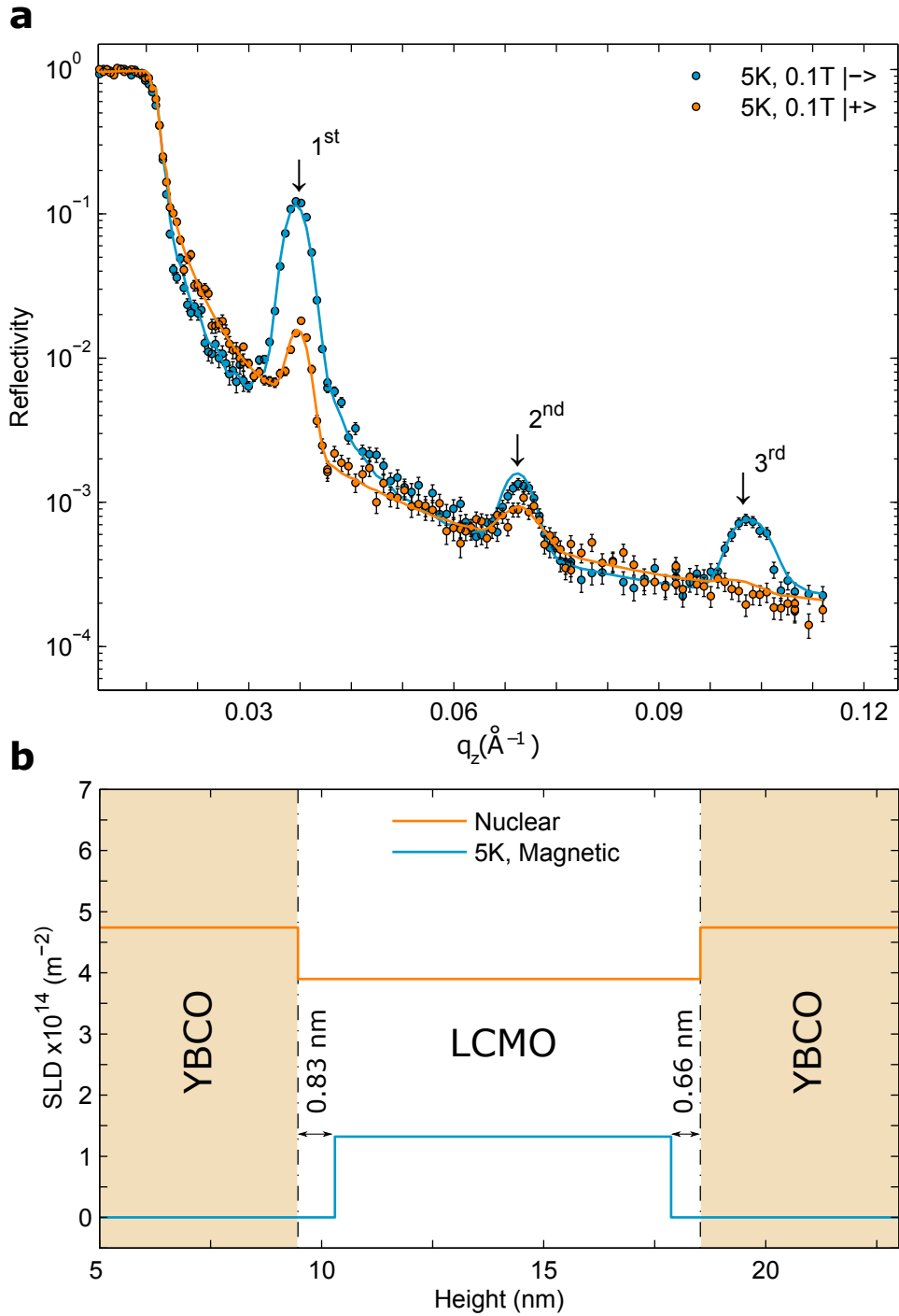


Figure 4.10: (a) Low temperature neutron reflectivity curves (symbols) vs.  $q_z$  for spin up (|+>) and spin down (|->) neutrons. The arrows indicate the position of the superlattice Bragg peaks. The solid lines are the best fits to the data. (b) The obtained depth profiles of the nuclear and magnetic scattering length density in the growth direction of the ML.

the reproducibility. The electric field vectors for the linearly polarized x-rays were oriented along the vertical ( $\sigma$ -polarization) and horizontal ( $\pi$ -polarization) direction with respect to the plane of incidence. In this geometry, the absorption for in-plane polarization ( $\mu_{ab}$ ) equals to the absorption for  $\sigma$ -polarization ( $\mu_{\sigma}$ ). The absorption for out-of-plane polarization ( $\mu_c$ ) can be calculated according to equation (4.4).

$$\mu_{ab} = \mu_{\sigma} \quad (4.3)$$

$$\mu_c = \sec^2 \theta \mu_{\pi} - \tan^2 \theta \mu_{\sigma} \quad (4.4)$$

where,  $\theta$  and  $\mu_{\pi}$  represent the angle of incidence and the absorption for  $\pi$ -polarization, respectively. The XLD is the difference between  $\mu_{ab}$  and  $\mu_c$ . It contains important information about the element specific orbital occupancy of the unoccupied states in the vicinity of the Fermi-level. The presented XLD spectra are normalized with respect to the corresponding maximum of  $\frac{1}{3}(2\mu_{ab} + \mu_c)$ . They are expressed in terms of a percentage to enable a direct comparison of the magnitudes of the XLD signals from different samples.

From the x-ray magnetic circular dichroism (XMCD) measurements at the  $L_{3,2}$ -edges of Cu and Mn ions we deduced the information about the magnetic properties. The XMCD represents the difference in the absorptions for left and right circularly polarized x-rays with angular momentum parallel ( $\mu_+$ ) and antiparallel ( $\mu_-$ ) to the applied magnetic field ( $H_{ext}$ ). It was measured by changing both the circular polarization (left and right) of the incoming x-rays and the direction of  $H_{ext}$ . The representative XMCD spectra are averaged over multiple sets of such measurements. To compare the XMCD signals from the different samples at different  $H_{ext}$ , we have normalized the XMCD spectra with respect to the maximum of  $\frac{1}{2}(\mu_+ + \mu_-)$ , and expressed it in percentage.

For both the XLD and XMCD experiments, we used total fluorescence yield (TFY) and total electron yield (TEY) modes. As photons have a small scattering cross section with the lattice, they do not get scattered strongly from the lattice. As a result, the detected photons originate from almost the entire sample and serves as a probe for the bulk Cu and Mn ions. On the other hand, the photo-electrons scatter strongly with the lattice. As a consequence, only photo-electrons near to the surface of the sample have enough kinetic energy to escape from the sample surface and contribute to the TEY signal. The sensitivity in TEY thus drops exponentially from the sample surface with a characteristic probe depth of several nanometers. In all our samples, the top layers are either LCMO or LAO capped LCMO. Therefore in TEY mode, we thus probe mainly the Mn ions of the topmost LCMO layer, and the interfacial Cu ions in the YBCO which is just beneath the former.

Below, we discuss the results from the XLD and XMCD experiments at the Cu and Mn  $L_{3,2}$ -edges at 2K. The method of the background subtraction and the normalization of the raw XAS data are detailed in Appendix A.1.

### 4.8.2 X-ray linear dichroism at Cu $L_{3,2}$ -edges

The Cu XLD data for YL1 and YL2 have been acquired at 0.5T, the ones for YL3 in zero field. Figure 4.11 displays the absorption profiles and the normalized XLD signals for all the samples. Each spectrum contains two resonant edges, namely  $L_3$  and  $L_2$ . These are electric dipole allowed transitions of the excited electrons from the core  $2p_{3/2}$  and  $2p_{1/2}$  levels to the empty  $3d$ -states, respectively. The spin orbit coupling at the  $2p$  level determines the separation of the two absorption edges, which is about 19.7 eV in the case of Cu. The 2 : 1 ratio of the intensity of the  $L_3$  and  $L_2$  edges arises since the  $2p_{3/2}$  and  $2p_{1/2}$  configuration consists of four and two  $m_j$  states, respectively. The intensity of  $\mu_{ab}$  and  $\mu_c$  is proportional to the number of holes in the  $3d_{x^2-y^2}$  and  $3d_{3z^2-r^2}$  orbitals, respectively. Below, it is used to deduce the relative orbital occupancy of the  $3d-e_g$  orbitals of the bulk and interfacial Cu ions.

For all samples in TFY mode, the intensity of  $\mu_{ab}$  is larger than the one of  $\mu_c$ . It indicates that for the Cu ions in the bulk of the YBCO layers, the holes mostly reside in the  $3d_{x^2-y^2}$  orbitals. This strong orbital polarization is related to the strong Jahn-Teller effect of the

$\text{Cu}^{2+}$  ions ( $3d^9$ ), which lowers the energy of the  $3d_{3z^2-r^2}$  states and increases their electron occupancy. The shoulders at the high energy side of the  $L_3$  and  $L_2$  edges originate from the Zhang-Rice singlets (ZRS) which arise from the antiferromagnetic coupling of the Cu-3d hole with the doped holes at the surrounding O ions (ligands) [83]. The transitions to the ZRS state are designated to the transition from the  $2p^6 2d^9 \underline{L}$  ground state to the  $2p^5 2d^{10} \underline{L}$  excited state, where  $\underline{L}$  represents a ligand hole. The Coulomb interaction between the core hole that is created by the photon absorption and the ligand hole enhances the energy that is required to excite an electron from the core level to the empty states of the 3d-band. Thus, the transition to the ZRS states occurs at slightly higher energy [84].

On the other hand, in TEY mode, where one probes the interfacial Cu ions at the topmost YBCO/LCMO interface, the intensity of the  $\mu_c$  absorption is strongly increased and the normalized XLD signal thus is reduced. This signals that the concentration holes in the  $3d_{3z^2-r^2}$  orbitals is significantly higher for the interfacial Cu ions than for the bulk-like Cu ions.

The following describes the method that was used to distinguish between the hole distribution in the  $3d-e_g$  orbitals of the interfacial and bulk Cu ions.

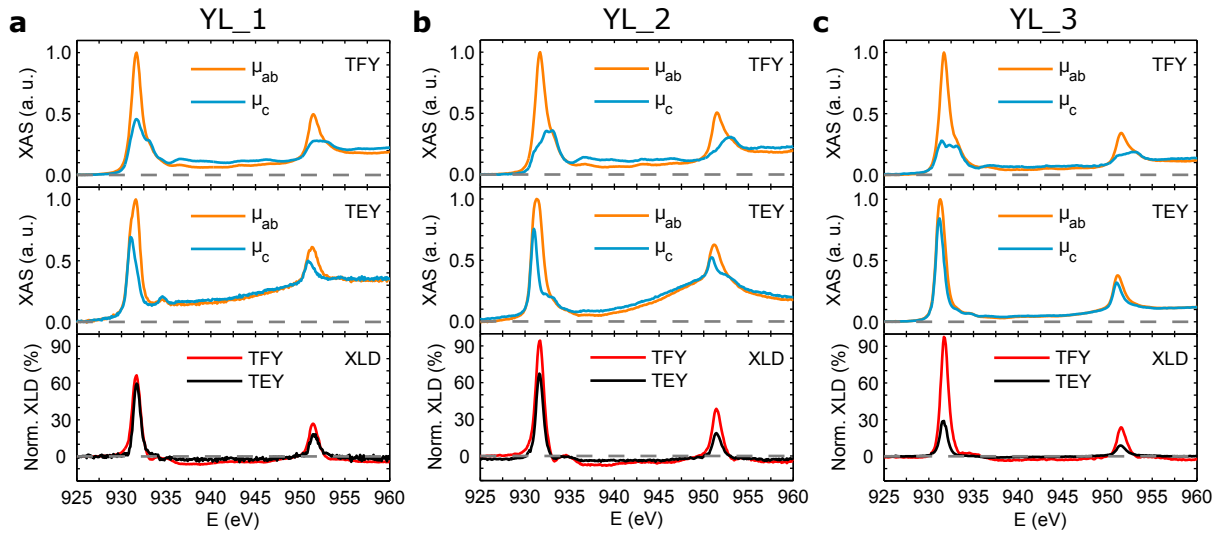


Figure 4.11: The Cu XLD data acquired at 2K for (a) YL\_1, (b) YL\_2 in 0.5 T and (c) YL\_3 in 0 T. The top and middle panels show the absorption for in-plane ( $\mu_{ab}$ ) and out-of-plane ( $\mu_c$ ) polarization in TFY and TEY modes, respectively. The bottom panels show the normalized XLD spectra in TFY and TEY modes.

**Multi-peak fitting of the XAS curves at the  $L_3$ -edge** From the middle panels of Figure 4.11, it is clear that the maxima in the spectra of  $\mu_{ab}$  and  $\mu_c$  are not located at the same energy. A similar effect was previously reported in Ref. [5] where this energy shift was attributed to a electron transfer across the interface from LCMO to YBCO. Alternatively, such a shift may be explained in terms of a modified crystal field at the interfacial Cu ions as compared to the bulk. In both cases, the charge distribution around the Cu ions changes. For a quantification of the above described effects, we performed a fitting of the XAS curves near the  $L_3$ -edges both in TFY and TEY modes with four Lorentzian profiles. More details on this fitting procedure can be found in Appendix A.2. The four Lorentzian profiles can be associated with the four possible transitions of the various Cu ions: (a) and (b) the  $2p^6 3d^9 \rightarrow 2p^5 3d^{10}$  transitions of the interfacial and the bulk  $\text{Cu}^{2+}$  ions, respectively, and (c) and (d) the  $2p^6 3d^9 \underline{L} \rightarrow 2p^5 3d^{10} \underline{L}$  transitions related to the ZRS of bulk Cu ions in the  $\text{CuO}_2$  planes and CuO chains, respectively.

Figure 4.12 displays the fitting of the XAS curves near the  $L_3$ -edge which has yielded four peaks at 930.4, 931.0, 931.7 and 932.6 eV for both YL\_1 and YL\_2. The corresponding

peak positions for YL\_3 bilayer are located at 930.5, 931.0, 931.5 and 932.4 eV. The energies are listed in the same order as the transitions (a)-(d) described above. The corresponding weights have been summarized in Table 4.4. The procedure how they have been calculated is described in Appendix A.2. The peak at 930.4 eV arises from the interfacial Cu ions. This is evident from the observation that its weight is very small in TFY mode whereas it becomes rather large in TEY mode. For the main peak centered at 931 eV, the absorptions for in-plane polarization ( $\mu_{ab}$ ) has a much larger intensity than for the out-of-plane polarization ( $\mu_c$ ). This indicates the holes in the bulk-like Cu ions have mainly  $3d_{x^2-y^2}$  character. A clearly different behavior is observed for the interfacial peaks at 930.4 eV for which the intensity of ( $\mu_c$ ) is almost equal to the one of  $\mu_{ab}$ . This indicates a redistribution of a significant amount of holes from the  $3d_{x^2-y^2}$  orbitals toward the  $3d_{3z^2-r^2}$  orbitals. This so-called ‘orbital reconstruction’ of the interfacial Cu ions [5] is most likely the consequence of the modified crystal field and/or a covalent bonding between the  $3d_{3z^2-r^2}$  orbital level of the Cu and Mn ions at the interface.

The two peaks at 931.5 and 932.6 eV are assigned to the ZRS states in the  $\text{CuO}_2$  planes and the CuO chains, respectively. the latter correspond to the transition related to the CuO chains. Since the holes in the CuO chains have mainly  $3d_{z^2-y^2}$  character, the absorption signal for the out-of-plane polarization is more intense than the one for the in-plane polarization.

	Peak 1		Peak 2		Peak 3		Peak 4	
	TFY	TEY	TFY	TEY	TFY	TEY	TFY	TEY
YL_1	4.3(2)	31.8(6)	66.2(3)	64.0(10)	15.8(5)	1.4(6)	13.6(7)	2.9(4)
YL_2	4.2(2)	46.0(0)	51.6(4)	33.5(1)	20.5(6)	6.7(1)	23.7(6)	13.9(2)
YL_3	4.9(2)	65.6(1)	44.5(2)	27.2(4)	16.2(3)	2.9(2)	34.4(7)	4.2(3)

Table 4.4: Calculated weights of the different transitions (described in the text) from the fitting of the XAS  $L_3$ -edge curves for YL\_1-3. Details on the fitting procedure are given in Appendix A.2. The error bar represents the maximum proportional error calculated from the standard errors of the least square fitting.

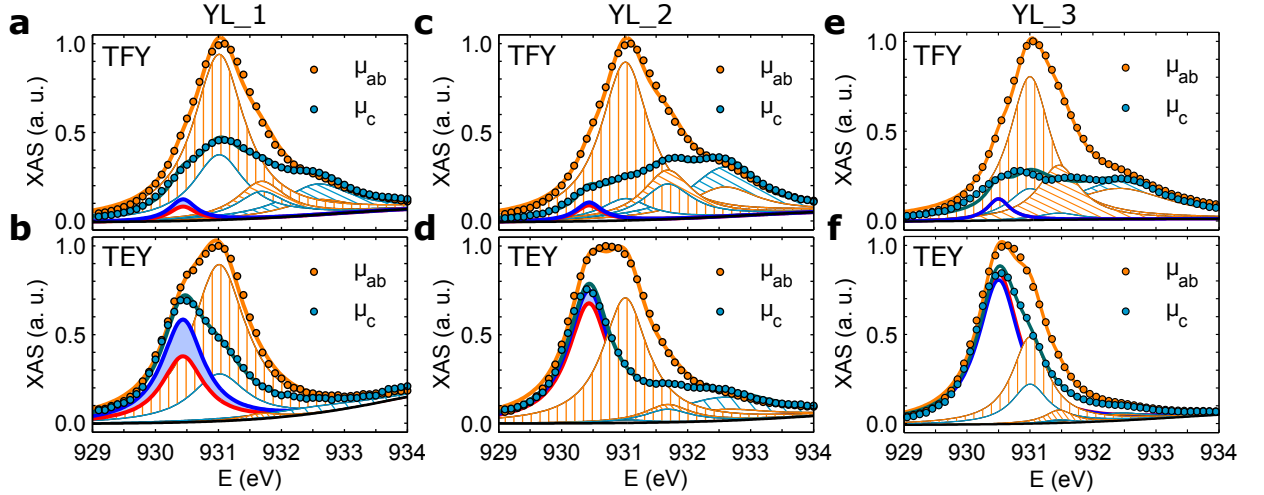


Figure 4.12: The fitting of the XAS curves near the  $L_3$ -edges in TFY and TEY modes. (a) and (b) for YL\_1; (c) and (d) for YL\_2; (e) and (f) for YL\_3.

### 4.8.3 X-ray linear dichroism at the Mn $L_{3,2}$ -edges

The Mn XLD was measured at 0.5 T for YL\_1 and YL\_2 and in zero field for any field for YL\_3. Figure 4.13 depicts the obtained absorption profiles and the normalized XLD signals in TEY mode. The two absorption edges centered around 642 and 653 eV correspond to the  $L_3$  and  $L_2$  edges, respectively. Compared to the Cu  $L_{3,2}$ -edges, the Mn edges are significantly

broad with a full width half maximum (FWHM) of about 4.3 eV. The latter arises because the XAS signal now contains contribution from both the  $t_{2g}$  and the  $e_g$  levels. Furthermore,  $\text{La}_{2/3}\text{Ca}_{1/3}\text{MnO}_3$  contains  $\text{Mn}^{3+}$  and  $\text{Mn}^{4+}$  ions which have four and three electrons in their  $3d$ -orbitals, respectively. Moreover, a finite overlap between the wavefunctions of the  $2p$  core hole that is created via x-ray absorption, and the holes in the  $3d$ -orbitals occurs in transition elements like Mn [85, 86].

In the following only the XAS data in TEY mode will be discussed. The curves in TFY mode are heavily distorted due to ‘self-absorption effects’ that are especially pronounced near the  $L_3$ -edge. An exemplary TFY XAS curve for YL\_2 is shown in Figure 4.14. In this case, the TFY absorption is no longer proportional to the absorption cross section of Mn, rather it strongly depends on the background absorption. The combination of the TFY signals from the self-absorbed fluorescence photons and the background results in dips in the XAS curves [87]. In the TEY signals, these effects are much weaker and can essentially be neglected.

As LCMO is the topmost layer for all the samples either covered by a thin LAO capping layer (for YL\_2 and YL\_3) or exposed to the ambient (for YL\_1), the TEY mode is mainly sensitive to the bulk-like Mn ions. The positive value of the integrated XLD signals ( $A_{XLD}$ ) for all the samples indicates a preferential hole occupancy of the  $3d_{x^2-y^2}$  orbital. Such a finite value of  $A_{XLD}$  is not expected for the Mn ions in bulk  $\text{La}_{2/3}\text{Ca}_{1/3}\text{MnO}_3$  crystal where the  $3d_{x^2-y^2}$  and  $3d_{3z^2-r^2}$  orbitals are usually found to be degenerate [88]. However, a similar finite orbital polarization has been previously reported for  $\text{La}_{2/3}\text{Sr}_{1/3}\text{MnO}_3$  films grown on LSAT substrates. These data have been explained the data in terms of the symmetry breaking at the surface, i.e., the missing apical oxygen at the ambient-film interface which breaks the symmetry of  $\text{MnO}_6$  octahedra and lowers the energy of the  $3d_{3z^2-r^2}$  orbital [89]. The present case is more complicated, since in YL\_2 and YL\_3, the LCMO layers are covered with additional LAO cap layer. An additional contribution to this non-degeneracy of the  $e_g$  levels of Mn may arise from strain effects. The compressive strain due to the 0.1% mismatch of the in-plane lattice parameters of LCMO and LSAT, may indeed play a crucial role in lifting the degeneracy of the  $3d-e_g$  levels. Table 4.5 summarizes the values of the obtained electron orbital polarizations,  $P_{e_g}$ . The details about the calculation can be found in Appendix A.4. The  $P_{e_g}$  is defined according to:

$$P_{e_g} = \frac{n_{3z^2-r^2} - n_{x^2-y^2}}{n_{3z^2-r^2} + n_{x^2-y^2}} \quad (4.5)$$

where  $n_{3z^2-r^2}$  and  $n_{x^2-y^2}$  are the number of electrons in the  $3d_{3z^2-r^2}$  and  $3d_{x^2-y^2}$  orbitals, respectively.

It is evident from Figure 4.13 a, b that the the XLD signals of YL\_1 and YL\_2 contain several substructures. Such features are typically observed in the presence of an antiferromagnetic order. In the present samples they may arise from the antiferromagnetic (AF) clusters which may be located in the vicinity of the interfaces where the ferromagnetic moment is strongly reduced (according to the PNR data shown in section 4.7). These features are indeed only visible for YL\_1 and YL\_2 for which the measurements were performed in 0.5 T and they are absent in YL\_3 which was measured in zero field. It should be mentioned that this magnetic contribution does not hamper the calculation of  $P_{e_g}$  which is based on the the total area under the XLD curve. This solely depends on the relative orbital occupation of the  $3d-e_g$  levels which do not change with temperature or magnetic field.

	YL_1	YL_2	YL_3
$P_{e_g}$ (%)	14.3(14)	2.7(3)	15.4(15)

Table 4.5: Calculated electron orbital polarization ( $P_{e_g}$ ) from the TEY XLD data for YL\_1-3. Details of the calculation and related error are discussed in Appendix A.4.

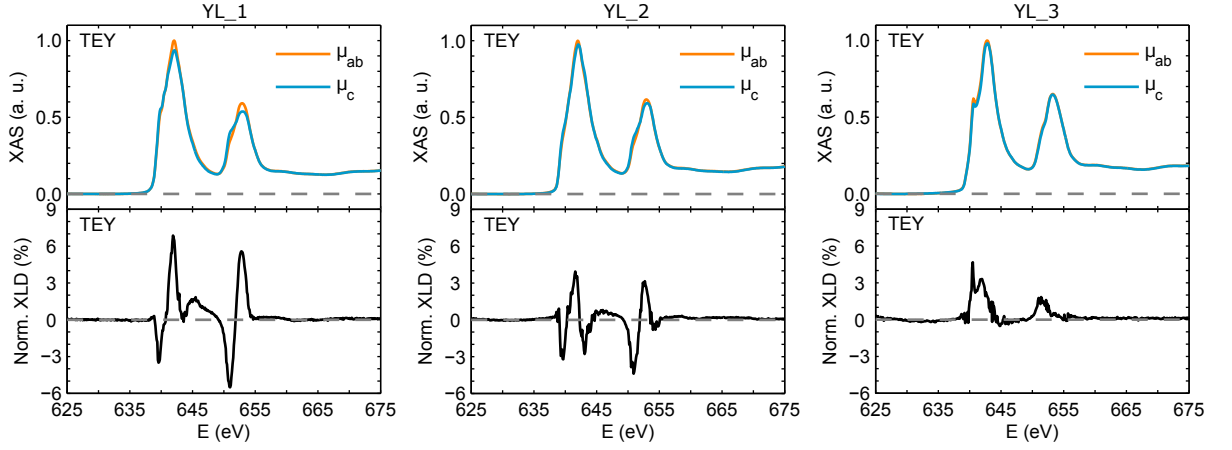


Figure 4.13: Mn XLD data acquired at 2 K for (a) YL\_1, (b) YL\_2 at 0.5 T and (c) YL\_3 at 0 T. The top panels show the absorptions for in-plane ( $\mu_{ab}$ ) and out-of-plane ( $\mu_c$ ) polarization in TEY mode. The bottom panels show the normalized XLD spectra in TEY mode.

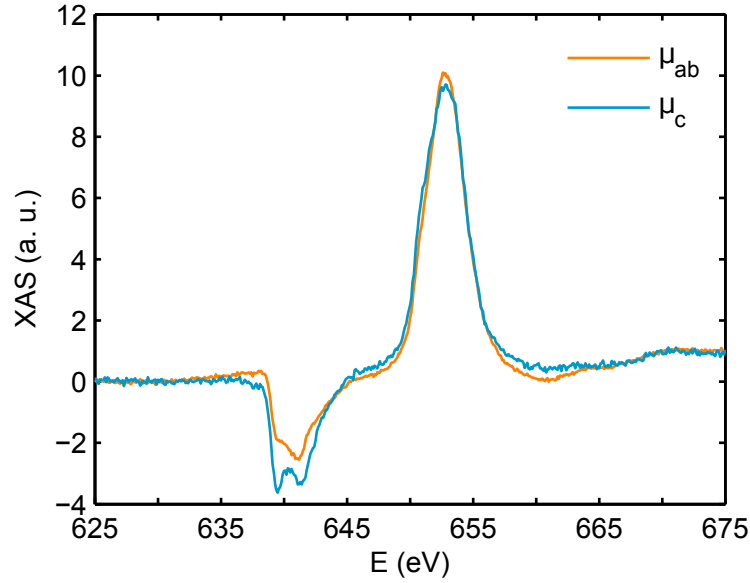


Figure 4.14: The Mn XAS data of YL\_2 acquired in TFY mode for linear polarizations along ab-plane and c-axis of the sample.

#### 4.8.4 XMCD at the Cu $L_{3,2}$ -edges

Figure 4.15a displays the Cu XMCD spectra of YL\_1-3 in TEY mode that were measured at field of 0.5 T and 5/6 T field, respectively. The XMCD curves at 0.5 T were obtained by switching both the magnetic field direction and the helicity of the incoming x-ray photons. During the switching of the field, it was always temporarily increased to  $\pm 5$  T to ensure the saturation of the ferromagnetic moment in the respective direction. The measurements in  $+5$  T or  $+6$  T were done only by changing the helicity of the incoming photons. Since the XMCD spectra in TFY mode show a very small signal that is within the noise level, we discuss only the TEY data.

In the presented Figure 4.15a, the positive and negative sign of the XMCD signals indicates the alignment of the Cu moments parallel and antiparallel to the applied field,  $H_{ext}$ , respectively. For YL\_1, the Cu moments are always antiparallel to  $H_{ext}$ , irrespective of the strength of  $H_{ext}$ . The Cu moments of YL\_2 are antiparallel in 0.5 T, whereas at 5 T they have switched their direction such that they are parallel to the field. In case of YL\_3, the Cu

moments are always parallel to the direction of  $H_{ext}$ . The magnitude of the maximal XMCD signal is similar for YL\_1 and YL\_2 where it amounts to about 5-8% of the total XAS signal. In YL\_3, the XMCD signal appears to be even a bit larger.

A More complete picture about the field dependence of the XMCD signal is shown in Figure 4.15b in terms of the field scans at a fixed energy near the maximum of the XMCD curves. Specifically, absorption for each helicity has been measured for each field (with a spacing of 0.1 T) at the energy position of the maximum XMCD signal and at a lower energy which is well inside the background region. We verified that the difference between these two absorption signals represents the XMCD signal very well. To increase the statistics, we show the average of the two XMCD branches between  $\pm 5/6$  T. These XMCD field scans have been scaled with respect to the XMCD signal of the corresponding high field measurement. We can see from Figure 4.15b that the magnitude of the antiparallel Cu moment for YL\_1 increases in the low field region up to 1 T. Toward higher fields it saturates. In case of YL\_2, the Cu moments are also antiparallel up to a field of about 1 T as for YL\_1. However, at larger field the Cu moment shows paramagnetic-like behavior. This leads to a sign change of the XMCD signal 3 T. This sign change is also evident from the corresponding high field XMCD spectrum at 6 T in Figure 4.15a. Whereas in YL\_1 the orientation of the Cu moment is always antiparallel to  $H_{ext}$ , in YL\_2 it changes the direction and becomes parallel at  $H_{ext} > 3$  T. Finally, in YL\_3, the Cu moment exhibits a kind of ‘super-paramagnetic’ response. The Cu moment gradually increases with the applied field and is parallel to  $H_{ext}$ . The saturation field seems to be larger than the maximum field of 5 T.

These observations raise the question whether the paramagnetic part of the signal of YL\_2 and the related sign change of the XMCD signal arises from the bulk-like or the interfacial Cu-ions. The TEY mode is most sensitive to the interfacial Cu ions, but it also contains a sizeable contribution from the bulk-like Cu-ions. It was previously shown from a similar XMCD study on bulk YBCO that a positive Cu XMCD signal can be induced by a large magnetic field [90]. This paramagnetic behavior of the bulk-like Cu ions has been interpreted in terms of the Dzyaloshinskii-Moriya interaction within  $\text{CuO}_2$  planes which also gives rise to a canting of the antiferromagnetically coupled  $\text{Cu}^{2+}$  spins. We have therefore performed a multi-peak fitting of the XAS curves in order to distinguish the XMCD signal of the bulk-like Cu ions from the one of the interfacial Cu ions. This analysis is shown in the following.

#### Multi-peak fitting of the XMCD XAS curves in TEY mode at the Cu $L_3$ -edge

Figure 4.16 shows the results of the XMCD multi-peak fitting (solid lines) of the TEY XAS and XMCD signals (symbols) near the  $L_3$ -edge at 0.5 and 5 T for YL\_1-3. As discussed in Appendix A.2, and in subsection 4.8.2, the lowest energy peak at 930.4 eV represents the contribution from the interfacial Cu ions. The peaks at higher energy arise from the bulk-like Cu ions. For YL\_1, it is evident that the negative XMCD signals at both low and high fields comes from the low energy peak at 930.4 eV and thus arises from the interfacial Cu ions. This suggests that the ferromagnetic Cu signal originates from the interfacial Cu ions. These Cu moments are antiparallel to  $H_{ext}$  at 0.5 T and 5 T. For YL\_2, major part of the XMCD signal arises also from the interfacial Cu ions. Notably, this applies for the antiparallel moments at 0.5 T as much as for the parallel moment at 6 T. As reported by G. M. De Luca *et al.* [90, 91], in the high field curves, we have also identified a smaller but well resolved positive XMCD signal from the bulk-like Cu ions. The multi-peak fitting for YL\_3 clearly indicates that the positive XMCD signals both in low and high fields originates at the from the interfacial Cu ions.

In conclusion, both the positive and negative XMCD signals in all samples are predominantly due to the interfacial Cu ions.

**Effective spin magnetic moment from TEY XMCD** We have calculated the effective spin magnetic moment ( $m_{s,eff}$ ) of the Cu ions from the TEY XMCD signal using conventional sum-rules [92–94]. Details are outlined in Appendix A.3. The obtained  $m_{s,eff}$  per Cu ion

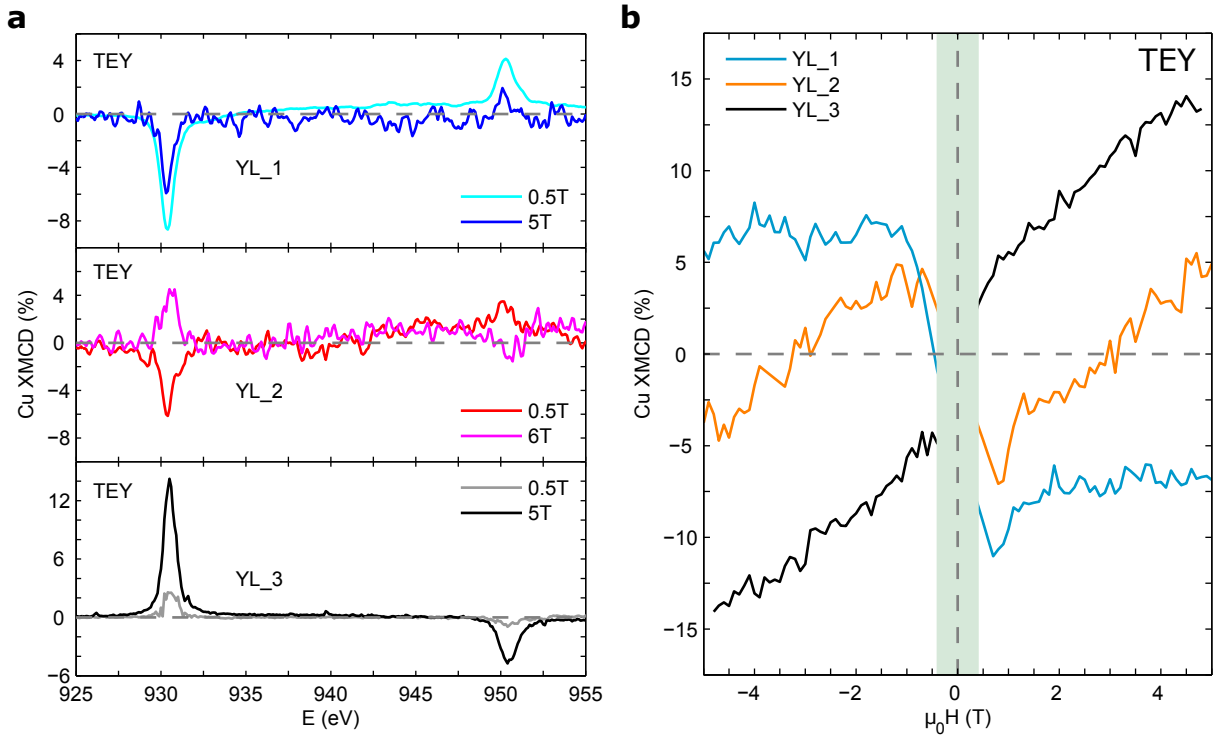


Figure 4.15: (a) The Cu XMCD spectra of YL\_1-3 in TEY mode measured at 2K in low and high magnetic fields. (b) Magnetic field scans of the Cu XMCD signal at the  $L_3$ -edge in TEY mode. The shaded area marks the region below  $\pm 0.4$  T where the remanence of the superconducting magnet inhibits reliable measurements.

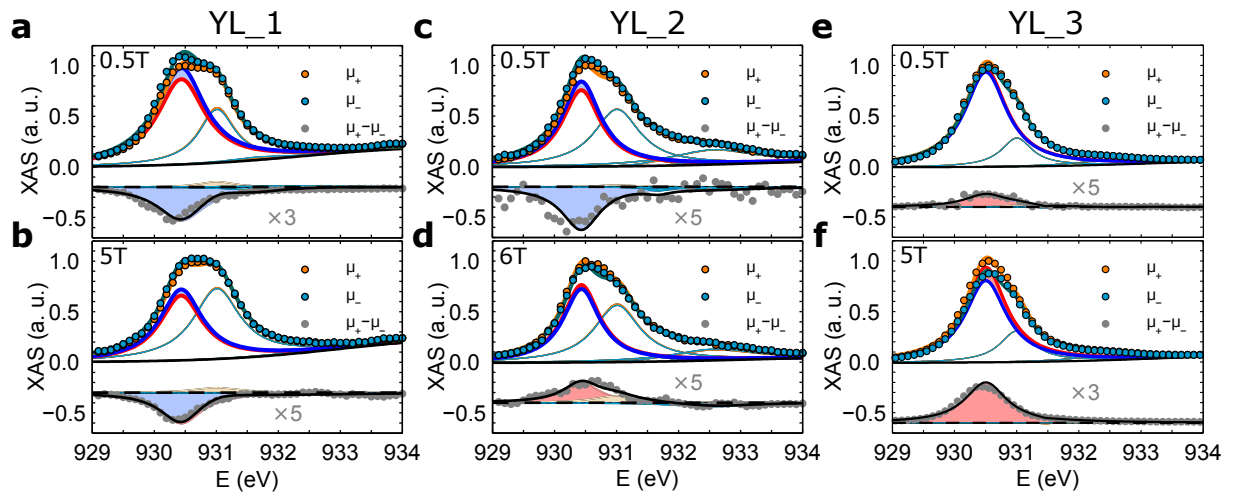


Figure 4.16: Multi-peak fitting (solid lines) of the TEY XAS curves ( $\mu_+$  and  $\mu_-$ ) around the Cu  $L_3$ -edge. The upper and bottom panels show the total XAS and the resulting XMCD signals, respectively. The bright red and blue solid lines show the contribution of the interfacial Cu ions for  $\mu_+$  and  $\mu_-$ , respectively. The orange and the light blue solid lines from the signals from the bulk-like Cu ions. (a) and (b) for YL\_1; (c) and (d) for YL\_2; (e) and (f) for YL\_3.

for YL\_1-3 are listed in Table 4.6. The negative and positive sign of  $m_{s,eff}$  represents the antiparallel and parallel alignment of the Cu moments with respect to the applied magnetic field.

	YL_1		YL_2		YL_3	
	0.5 T	5 T	0.5 T	6 T	0.5 T	5 T
$m_{s,eff}$ ( $\mu_B/\text{Cu}$ )	-0.07(1)	-0.06(2)	-0.05(2)	0.06(2)	0.03(1)	0.14(3)

Table 4.6: Effective spin magnetic moment of the Cu ions as derived from the XMCD signal in TEY mode by using the sum-rules. The calculations are detailed in Appendix A.3.

The values of  $m_{s,eff}$  as mentioned above, are normalized with respect to the total number of the Cu ions that are probed in TEY mode. We have already seen from the multi-peak fitting that the TEY XAS curves not only contain the contribution from the interfacial Cu ions, but also a significant amount from the bulk Cu ions and the Zhang-Rice singlets. The multi-peak fitting has however shown that only the interfacial Cu ions give rise to the XMCD signal. Accordingly, we have normalized the Cu moment with respect to the weight of the interface peak as derived from the XLD curves in TEY mode. This weight represents the fraction of interfacial Cu ions that contribute to the corresponding transition. The resulting moments per interfacial Cu ion are listed in Table 4.7.

	YL_1		YL_2		YL_3	
	0.5 T	5 T	0.5 T	6 T	0.5 T	5 T
$m_{s,eff}$ ( $\mu_B/\text{Cu}^{int}$ )	-0.22(3)	-0.19(3)	-0.11(4)	0.13(4)	0.05(2)	0.24(4)

Table 4.7: Effective spin magnetic moment per interfacial Cu ion.

#### 4.8.5 X-ray magnetic circular dichroism at Mn $L_{3,2}$ -edges

The Mn XMCD signals of YL\_1-3 at the  $L_{3,2}$ -edges have been measured in TEY and TFY modes. The data were taken in high and low fields by following the same strategy as for the Cu XMCD experiments. As LCMO is the topmost layer in all samples, the TEY mode is most sensitive to properties of the Mn ions at the interface of LCMO with the ambient or the LAO capping layer. Due to the ‘self-absorption effects’, the XAS curves at the  $L_3$ -edge are severely distorted (similar to Figure 4.14). The properties of the buried LCMO layers thus are not accessible from these data. Figure 4.17a depicts the XMCD spectra for all three samples as measured in 0.5 and 5/6 T. Very strong XMCD signals of about 40-50 % have been observed for YL\_1 and YL\_2. In agreement with the dc magnetisation data shown in section 4.5, the XMCD signal is slightly larger for YL\_2 than for YL\_1. On the other hand, the XMCD signal for YL\_3 is only about 1 % at 0.5 T. In a high field of 5 T, it increase to about 10 %. This indicates that the 5 nm thick LCMO layer of YL\_3 is hardly ferromagnetic.

In addition, the magnetic field scans of the maximum XMCD signals have been measured as shown in Figure 4.17b. Saturation of the XMCD signals is observed in the high field region for YL\_1 and YL\_2, as expected for ferromagnetic LCMO. However, even in the saturation, there is a slight increment of the moment. A behavior has been reported for polycrystalline LCMO film [95], where it has been explained in terms of the alignment of spins in magnetically disordered regions near the grain boundaries. The high field leads to a canting of these spins, and thus the slight increase of the average magnetization. In the present case, the disorder in the topmost LCMO layer may arise from the interface to the ambient or the LAO cap layer. Furthermore, the coupling between the Cu and Mn ions at the YBCO/LCMO interface may also give rise to a canting of the Mn moments. For YL\_3, remanent magnetization in the field scan is very small and resembles a super-paramagnetic behavior. Whereas the Mn XMCD signal increases as a function of  $H_{ext}$ , and it still remains well below the one found in YL\_1 and YL\_2. This indicates the ferromagnetism in this sample is strongly suppressed.

By applying the sum-rules, the effective spin magnetic moment of the Mn ions in the topmost LCMO layers have been calculated for YL\_1-3 (details can be found in Appendix A.3) as shown Table 4.8.

	YL_1		YL_2		YL_3	
	0.5 T	5 T	0.5 T	6 T	0.5 T	5 T
$m_{s,eff}$ ( $\mu_B/\text{Mn}$ )	1.79(18)	2.00(20)	2.28(23)	2.56(26)	0.27(3)	0.75(8)

Table 4.8: Effective spin magnetic moment per Mn ion as derived from the XMCD signal in TEY mode by using the sum rules. Please visit Appendix A.3 for details about the calculations and the errorbars.

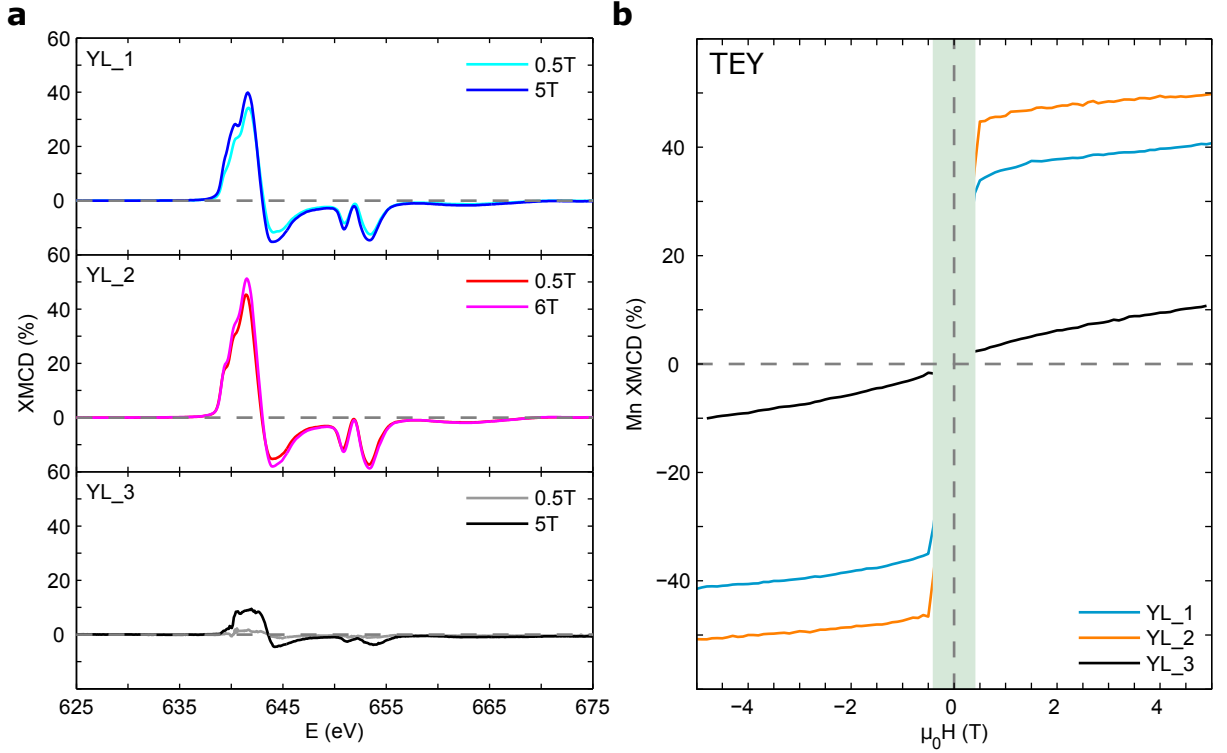


Figure 4.17: (a) The Mn XMCD spectra of YL\_1-3 in TEY mode measured at 2 K in both high and low magnetic field. (b) Magnetic field scans of Mn XMCD signals at the  $L_3$ -edge in TEY mode. The shaded area marks the low-field region (below  $\pm 0.4$  T) where the remanence of the superconducting magnet inhibits reliable measurements.

#### 4.8.6 Summary

The Cu XLD data and the corresponding multi-peak analysis have shown that the Cu ions near the interface undergo an orbital reconstruction. For the bulk-like Cu ions, the  $3d_{3z^2-r^2}$  orbitals are almost fully occupied. Whereas, for the interfacial Cu ions, they acquire a significant amount of holes such that their filling becomes comparable to the one of the  $3d_{x^2-y^2}$  orbital. The XMCD data and the related multi-peak analysis revealed that the magnetic Cu moments originates mostly from these orbitally reconstructed, interfacial Cu ions. For YL\_1, the Cu XMCD signal is always negative at small as well as well as very large fields. This indicates a strong antiferromagnetic exchange interaction (AEI) between the interfacial Cu and Mn moments. On the other hand in YL\_2, the direction of the interfacial Cu moments depends on the strength of the external field. It is negative at first, but becomes positive for high fields above 3 T. The observed behavior is suggestive of a very weak antiferromagnetic (AF) coupling between the interfacial Cu and Mn moments that can be overcome by a large magnetic field.

Strikingly similar XMCD field scans have indeed been observed in a molecular system with a weak antiferromagnetic coupling between Cr and Dy moments [96]. Finally, in YL\_3, there are sizeable Cu moments that are always aligned along  $H_{ext}$ . This indicates that the AEI is essentially absent. Despite the very different field dependence of the XMCD signals in these samples, the deduced effective spin magnetic moments per interfacial Cu ion have rather similar values of 0.11-0.24  $\mu_B$  that agree well with the one of previous reports [1, 3, 4].

The Mn XMCD data confirm that the LCMO layer in YL\_3 is hardly ferromagnetic. To the contrary, for YL\_1 and YL\_2 they reveal a strong ferromagnetic order of the Mn moments. In addition, for all three samples, we find non-zero Mn XLD signals which suggest a weak orbital polarization ( $P_{eg}$ ) of the Mn ions of about 14-15 % in YL\_1 and YL\_3, and 3-4 % in YL\_2.

## 4.9 Discussion and concluding remarks

The investigated multilayers of type YL\_1 to YL\_3 were grown on (001)-oriented LSAT substrates using the PLD technique. The XRD studies confirmed the epitaxial growth of each component of these MLs with the c-axis of the YBCO layer along the surface normal. STEM and EELS studies revealed the interfacial stacking of CuO<sub>2</sub>-BaO-MnO<sub>2</sub> at both YBCO/LCMO and LCMO/YBCO interfaces. The same interface termination was also reported for YL\_1 in Ref. [71], which gives rise to a straight Cu-O<sub>apical</sub>-Mn bond.

RBS studies found that the LCMO layers in YL\_1 are fully stoichiometric, while in YL\_2, they are strongly Mn and O deficient and thus less hole doped than in YL\_1. This has a clear impact on the electronic and magnetic properties of LCMO as shown with the dc transport and optical measurements which reveal that the LCMO layers in YL\_2 are less conductive than the ones in YL\_1. On the other hand, the ferromagnetic properties of the LCMO layers in YL\_1 and YL\_2 are rather comparable. The Curie temperatures are 215 and 180 K in YL\_1 and YL\_2, respectively. Both samples have sizeable saturation values of the dc magnetisation of 2.0 and 2.5  $\mu_B$  per Mn, respectively. To the contrary, in YL\_3, the ferromagnetic order in the very thin (5 nm) LCMO layer is strongly suppressed, and the average magnetization yields a small values of only 0.25  $\mu_B$  per Mn.

The optical data confirm the poor conductivity of the LCMO layers in YL\_2 as compared to YL\_1. In addition they show that a mid-infrared band, which is characteristic of the formation of FM polarons, is more pronounced in YL\_2.

The PNR study of YL\_2 reveals that the suppression of the FM order of the Mn moments near the interfaces is significantly weaker than the one that was previously reported for YL\_1 in Refs. [3, 29]. It is also found that the FM order of the Mn moments is hardly suppressed at the interfaces of a YBCO/LMO ML for which the LMO layers are insulating ferromagnetic state [3]. This suggests that the suppression of the FM order of the Mn moments at the interfaces (so-called ‘depleted layer’ effect) is closely linked to the conducting properties of the manganite layer. This can be understood in terms of a scenario for which the insulating ferromagnetic state is composed of orbital polarons. This polaronic state is only poorly conducting (or even insulating) but its FM order is less susceptible to the detrimental effect of strain and defects that may arise near the interface of YBCO. Thus, the ferromagnetic order is more robust and the ‘depleted layer’ thickness is smaller when the polaron order is strong and long range in nature as in the cases of the MLs YBCO/LMO and YL\_2.

The XLD studies revealed that the interfacial Cu ions samples undergo an orbital reconstruction. This is the case in all three types of samples, which suggests that it is quite a robust phenomenon that occurs independent of the details of the hole doping or the defects in the LCMO layers. It has previously been shown that this orbital reconstruction is related to a particular layer stacking at the interface for which the Cu and Mn ions are directly connected via the apical oxygen [4]. The resulting strong covalent bonding between the  $3d_{3z^2-r^2}$  orbitals of the interfacial Cu and Mn ions gives rise to a redistribution of charge and also to a redistribution of the electrons between the Cu  $3d_{3z^2-r^2}$  and the  $3d_{x^2-y^2}$  orbitals. As a result, the

hole density on the Cu  $3d_{3z^2-r^2}$  orbitals is about equal to the one on the Cu  $3d_{x^2-y^2}$  orbitals. These orbitally reconstructed Cu ions appear to be the source of the ferromagnetic Cu moments, irrespective of whether these moments are weakly coupled (YL\_2) or strongly coupled (YL\_1) to the Mn moments. They are even present if the Mn moments are absent (YL\_3). Independent of the strength of the AEI, effective spin magnetic moments per interfacial Cu ion are in the range of 0.11-0.24  $\mu_B$ . In the following, we discuss the mechanism which controls the strength of the AEI.

Since the growth direction of the epitaxial MLs is along (001)-axis, the AEI across the interface is governed by the hybridization of the Cu  $3d_{3z^2-r^2}$  and Mn  $3d_{3z^2-r^2}$  orbitals. Depending on the occupancy of the Mn  $e_g$ -orbitals, two coupling schemes are possible as depicted in Figure 4.18a (which shows the extreme cases of either an electron in the  $|x^2 - y^2\rangle$  or an electron in the  $|3z^2 - r^2\rangle$  orbital). When in-plane orbital of Mn is occupied with the electron, according to the Mn on-site Hund's coupling, the electron hopping from Cu to Mn requires a FM coupling. On the other hand, when the electron resides in the Mn  $3d_{3z^2-r^2}$  orbital, only a spin down electron can be shared due to Pauli's exclusion principle which results in anti-ferromagnetic (AF) coupling. The strong AEI in YL\_1 thus can be understood in terms of a preferred occupation of the Mn  $3d_{3z^2-r^2}$  orbitals. Such a polarization of the Mn  $e_g$ -orbitals is indeed suggested by the TEY Mn XLD data in Figure 4.13a which yield an electron polarization of the  $e_g$ -orbitals of  $P_{e_g} \approx +14.3\%$ . The sketch in Figure 4.18b shows how the presence of the FM polarons in YL\_2 reduces the strength of the AEI. It displays the spatial arrangement of the occupied Cu and Mn  $e_g$ -orbitals close to the interface for a FM polaron lattice at a hole doping level of  $x=0.25$  (a lower hole doping requires a correspondingly larger unit cell). Notably, this polaron lattice involves an alternation of the in-plane and out-of-plane polarization of the occupied Mn  $e_g$ -orbitals along the lateral direction. According to the sketch in Figure 4.18a, such an alternating occupancy of the Mn  $e_g$ -orbitals results a corresponding sign change of the interfacial exchange interaction and thus a strong reduction of the effective AEI. In line with this orbital polaron scenario, for which the average polarization of the Mn  $e_g$ -levels should vanish (for deduction see in Appendix B), the Mn XLD signal of YL\_2 in Figure 4.13b is reduced to  $P_{e_g} \approx +2.7\%$ . For the explanation of the weak AEI in YL\_2, we have considered a FM polaron order as it exists in the bulk of underdoped LCMO in the insulating ferromagnetic part of the doping phase diagram. It is reasonable to assume that this kind of FM polaron order also persists at the interface with YBCO. This is justified as we have seen for YL\_2 that the ferromagnetic order of the Mn moments at the interface is weakly suppressed than in YL\_1, i.e., the 'depleted layer' in YL\_2 is thinner than the one in YL\_1.

Another important aspect involves the circumstance that a sizeable Cu moment is observed even without the FM order of the Mn moments, i.e., in YL\_3. This suggests that the Cu moments are intrinsic to the interfacial  $\text{CuO}_2$  planes, i.e., they are not induced by the AEI with the FM moments. The  $\text{CuO}_2$  plane next to the interface is indeed expected to be strongly underdoped due to the electron transfer from the LCMO to YBCO and a missing CuO chain layer which serves as a charge reservoir [71, 97]. Also, due to the orbital reconstruction, the Cu ions next to the interface have a pronounced hole occupation in the  $3d_{3z^2-r^2}$  levels. As discussed in Appendix C, this weakens the intra-planar AF exchange interaction between the Cu moments and may even give rise to a weak FM coupling.

In summary, the antiferromagnetic exchange interaction (AEI) between the interfacial Cu and Mn moments in YBCO/LCMO multilayers can be strongly suppressed, whereas the magnetic moment of the interfacial Cu ions remains sizeable. This suggests that this Cu moment is not induced by the AEI with Mn, but it is an intrinsic feature due to their orbital reconstruction.

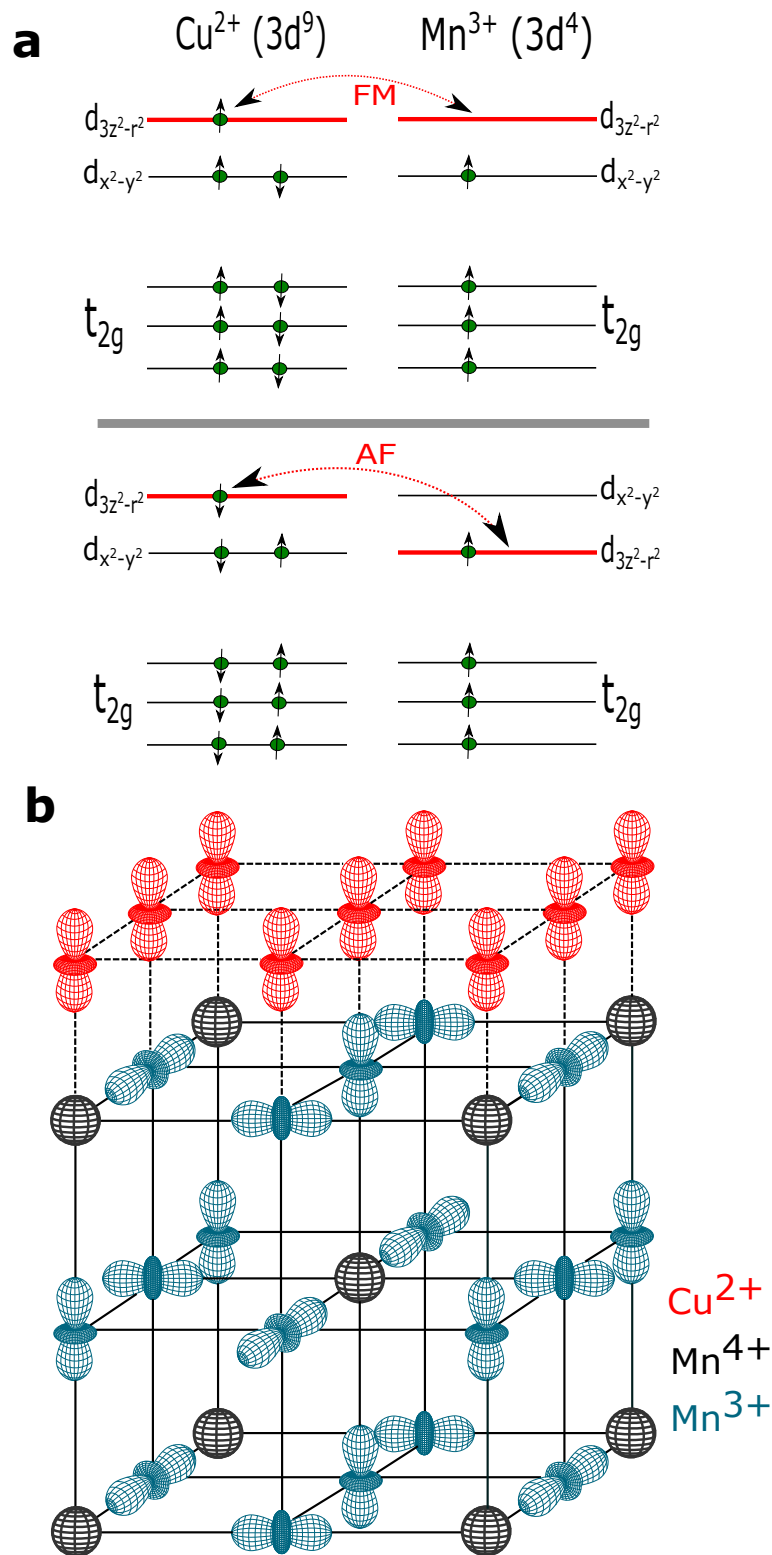


Figure 4.18: (a) Level scheme for the interfacial Cu-3d and Mn-3d showing the change of the magnetic exchange interaction from FM (upper panel) to AF (lower panel) as the polarization of the occupied Mn- $e_g$  orbitals changes from the in-plane to the out-of-plane one. Shown is the idealized case of a 100 % orbital polarization due to the orbital reconstruction on the Cu-side. (b) Sketch of the LCMO/YBCO interface for a lattice of the orbital polarons (in a FM state at 25 % hole doping). For YBCO only the  $3d_{3z^2-r^2}$  orbitals are shown which participate in the exchange interaction.

## Chapter 5

# Superconductivity and charge localization in ultrathin $\text{La}_{1.85}\text{Sr}_{0.15}\text{CuO}_4$

This chapter is concerned with the superconducting properties and the charge localization in ultrathin films of  $\text{La}_{1.85}\text{Sr}_{0.15}\text{CuO}_4$ , and in heterostructures of  $\text{La}_{1.85}\text{Sr}_{0.15}\text{CuO}_4/\text{La}_2\text{CuO}_4$  (LSCO/LCO),  $\text{La}_{1.85}\text{Sr}_{0.15}\text{CuO}_4/\text{La}_{2/3}\text{Ca}_{1/3}\text{MnO}_3$  (LSCO/LCMO) and LSCO/LCO/LCMO. The pulsed laser deposition of the thin films and heterostructures is described in section 5.1. The structural characterization of the samples is summarized in section 5.2. The transport and magnetic properties of the thin films of LSCO, LCO and LCMO are discussed in section 5.3. The suppression of superconductivity due to ferromagnetism in LSCO/LCMO bilayers is shown in section 5.4. The transport properties of LSCO/LCO/LCMO trilayers are reported in section 5.5. A strong localization of the charge carriers has been observed in a LSCO/LCO bilayer in which the LCO layer is seven unit cells thick. The origin of such charge localization is discussed in section 5.6. We verified that the charge localization phenomena are reproducible, as presented in section 5.7. Finally, we outline the main findings in section 5.8.

### 5.1 Pulsed laser deposition of thin films and heterostructures

In the following, we discuss the pulsed laser deposition (PLD) of thin films of  $\text{La}_{1.85}\text{Sr}_{0.15}\text{CuO}_4$  (LSCO),  $\text{La}_2\text{CuO}_4$  (LCO) and  $\text{La}_{2/3}\text{Ca}_{1/3}\text{MnO}_3$  (LCMO), and their heterostructures on (001)-oriented  $\text{SrLaAlO}_4$  (SLAO) substrates. This section is divided into two subsections. The first one outlines the depositions of the thin films and the heterostructures using pure  $\text{N}_2\text{O}$  gas following the recipe described in Ref. [98]. The latter presents a further development in the growth of the LSCO and the LCO films using a mixture of pure  $\text{N}_2\text{O}$  and  $\text{O}_2$  gases.

#### 5.1.1 Growth

##### Thin films

All depositions were made on commercially available  $5 \times 5 \times 0.5 \text{ mm}^3$  (001)-oriented SLAO substrates from the companies MTI Corporation [99] and Crystal GmbH [100]. We chose the SLAO substrate since it is almost lattice matched with  $\text{La}_{2-x}\text{Sr}_x\text{CuO}_4$  and is not twinned. The in-plane lattice parameters ( $a$ ) for tetragonal SLAO, LSCO and LCO are 3.7560, 3.7736 and 3.8006 Å, respectively [101, 102]. For LSCO and LCO, this yields a relatively small lattice mismatch of -0.5 and -1.2%, respectively, which gives rise to a weakly compressive strain. For LCMO, the lattice mismatch of -3% gives rise to a much larger compressive strain.

The deposition according to procedure A was carried out in an atmosphere of 0.11 mbar of  $\text{N}_2\text{O}$  gas pressure and at a substrate temperature of 730 °C. The target to substrate distance was kept at about 5 cm. The laser fluence for LSCO (or LCO) and LCMO was 1.0 and

$1.5 \text{ J/cm}^2$  with a laser repetition rate of 2 Hz. After each deposition, the  $\text{N}_2\text{O}$  gas was flushed out from the PLD chamber with a flow of  $\text{O}_2$  gas. The  $\text{O}_2$  pressure was then increased to 1 bar, and subsequently the sample was cooled to  $550^\circ\text{C}$  at a rate of  $5^\circ\text{C}/\text{min}$ . At  $550^\circ\text{C}$ , the sample was annealed for one hour before it was rapidly cooled to room temperature.

The growth was monitored with *in-situ* reflection high energy electron diffraction (RHEED). Figure 5.1a-c represents the RHEED patterns (upper panels) of the deposited films and the related time evolution of the (00) Bragg peak (bottom panels) during the growth. The bright vertically elongated streaks in the RHEED pattern are indicative of a flat film surface. The time evolution of the (00) Bragg peak for LSCO exhibits several oscillations. Each of these oscillations corresponds to the deposition of two LaO and one  $\text{CuO}_2$  layer, i.e., of half of a crystallographic unit cell (u.c.) of LSCO. Such oscillations are a good indication for a *layer-by-layer* growth mode, and they allow us to monitor the film thickness with a sub-unit-cell precision. For this growth procedure A, it always occurred that the first two intensity oscillations of the RHEED signal were heavily damped. This damping seems to arise from a so-called Stranski-Krastanov growth mode which involves a mixture of *layer-by-layer* and 3-dimensional (3D) island growths [58]. As a result, the first LSCO monolayer (with a thickness of 1 u.c.) consists a significant amount of disorder. After the deposition of the first monolayer, the growth mode converts into an almost perfect *layer-by-layer* mode, as is indicated by the sharp oscillations until the end of the growth. Unlike LSCO, the oscillations for LCO and LCMO are strongly damped during the entire growth, and thus are only visible upon zooming (see the insets of Figure 5.1b-c). It suggests that the growth modes for the LCO and LCMO films are not purely *layer-by-layer*, perhaps a combination of the *layer-by-layer* and the 3D island growths. For LCMO, each RHEED intensity oscillation corresponds to a single u.c. The minute intensity recovery after the deposition indicates a further rearrangement of the adatoms towards a smoother surface.

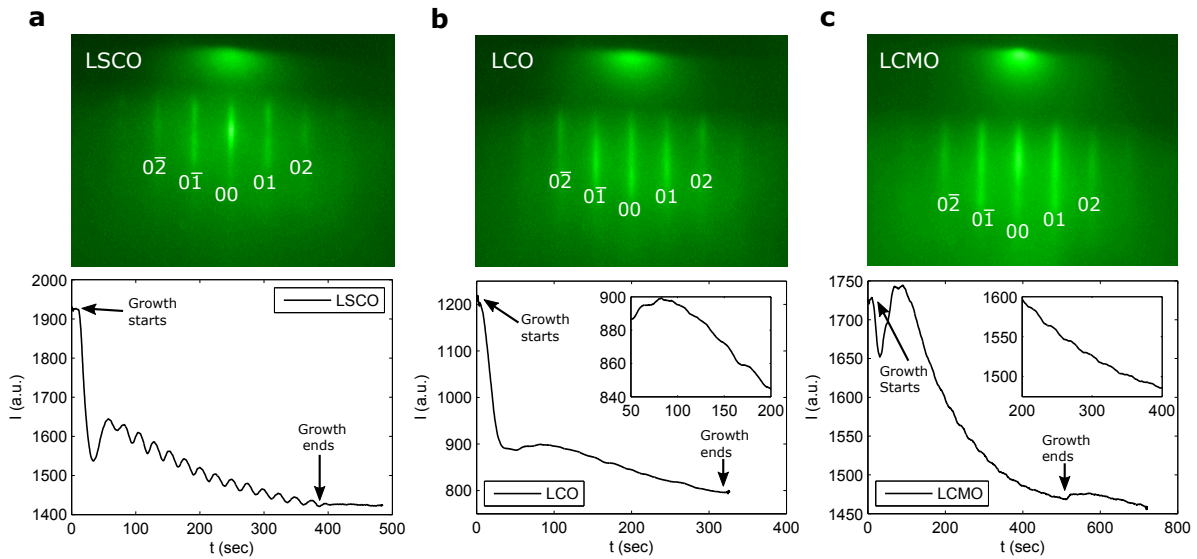


Figure 5.1: The RHEED pattern (upper panel) and time evolution of the average intensity of the (00) Bragg peak (lower panel) during the deposition of thin films of (a) LSCO, (b) LCO and (c) LCMO on SLAO substrates.

## Heterostructures

The number of laser pulses that are required for the growth of a certain number of unit cells of LSCO, LCO or LCMO has been derived from the intensity oscillations of the RHEED signal of the corresponding film that are discussed in the previous paragraph. In the following, the growth procedure of a LSCO(5 u.c.)/LCMO(20 u.c.) bilayer (BL) and a LSCO(5 u.c.)/LCO(2 u.c.)/LCMO(20 u.c.) trilayer (TL) is outlined.

Figure 5.2 displays the RHEED pattern and intensity oscillation during the deposition of the LSCO-LCMO-BL. As discussed earlier, the first two RHEED intensity oscillations for LSCO are heavily damped, which is believed to be an indication of the Stranski-Krastanov growth mode. We do not see clear RHEED intensity oscillations for LCMO when it is grown on top of LSCO or LCO. This is because the growth mode for LCMO in the heterostructures differs from its growth directly on the substrate surface.

Figure 5.3a-c represents the RHEED patterns and intensity oscillations of 5 u.c. of LSCO, 2 u.c. of LCO and 20 u.c. of LCMO for the deposition of the LSCO-LCO-LCMO-TL. Once again, the RHEED intensity oscillations for the first u.c. of LSCO are comparatively damped. As discussed earlier, the first u.c. of the LSCO layer has a considerable amount of disorders and defects. For the deposition of 2 u.c. of LCO, the corresponding four oscillations are well resolved. The RHEED pattern of LCO is comparatively less intense, and also, the corresponding RHEED intensity gradually decreases over time. This is an indication of an increasing surface roughness. After the deposition of each monolayer a minute intensity recovery is observed. We further verified the film thicknesses from the x-ray reflectivity measurements.

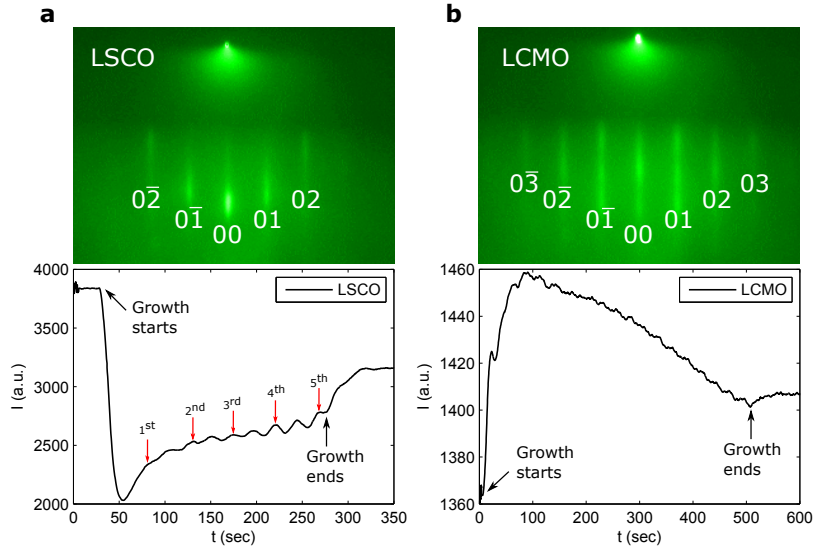


Figure 5.2: The RHEED pattern (upper panel) and time evolution of the average intensity of the (00) Bragg peak (lower panel) during the deposition of (a) 5 u.c. LSCO and (b) 20 u.c. LCMO for a LSCO(5 u.c.)-LCMO(20 u.c.)-BL. The red arrows mark the completion of unit cells.

### 5.1.2 Improving the PLD growth of $\text{La}_{2-x}\text{Sr}_x\text{CuO}_4$

It was noticed that the growth of the LSCO and the LCO films can be further improved using a mixture of the pure  $\text{N}_2\text{O}$  and  $\text{O}_2$  gases. By adjusting the flow control valves, partial pressures of 0.11 mbar of  $\text{N}_2\text{O}$  and 0.03 mbar of  $\text{O}_2$  have been maintained in the PLD chamber during deposition. The rest of the growth parameters and the annealing procedures were the same as mentioned above. In the following, we refer to this as the growth mode B. Figure 5.4 displays the growth of a LSCO/LCO BL, labeled as LSCO-LCO-BL\*, for which the LSCO and the LCO layers are 1 and 2 u.c. thick, respectively. The first two LSCO intensity oscillations are now much more prominent than for the growth mode A. Apparently, the difference in the gas mixture has a strong influence on the growth mode of the first and possibly even the second u.c., which is now an almost perfect *layer-by-layer* mode. Accordingly, it is expected that these first two monolayers of LSCO are significantly less disordered than for the sample grown with mode A. This has also a significant effect on the transport properties of the films, as will be shown in subsection 5.7.1.

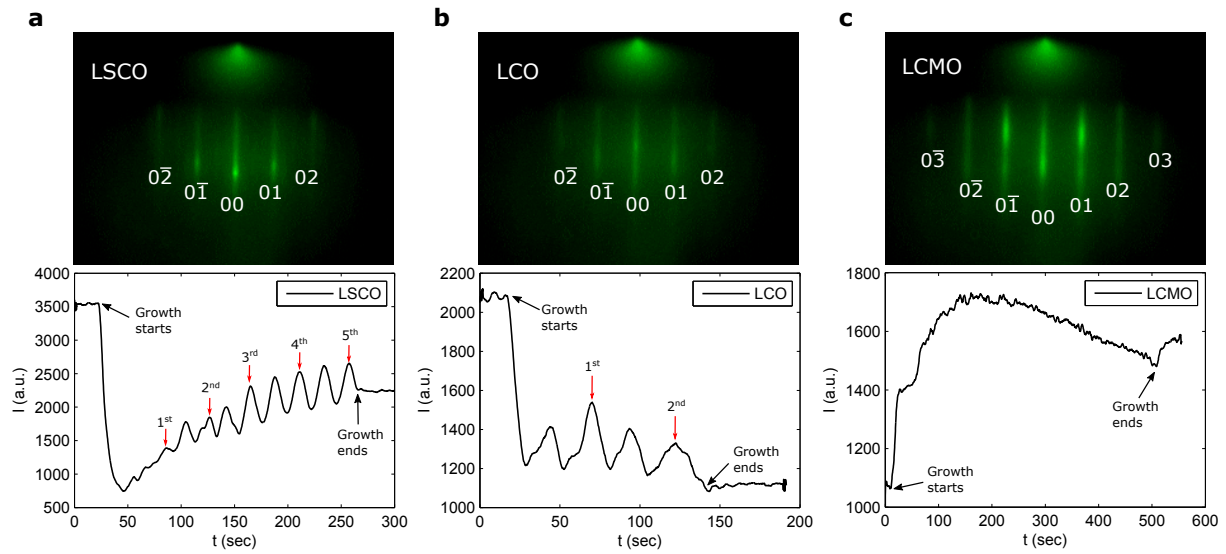


Figure 5.3: The RHEED pattern (upper panel) and time evolution of the average intensity of the (00) Bragg peak (lower panel) during the deposition of (a) 5 u.c. LSCO, (b) 2 u.c. LCO and (c) 20 u.c. LCMO which form a LSCO(5 u.c.)-LCO(2 u.c.)-LCMO(20 u.c.)-TL. The red arrows mark the completion of unit cells.

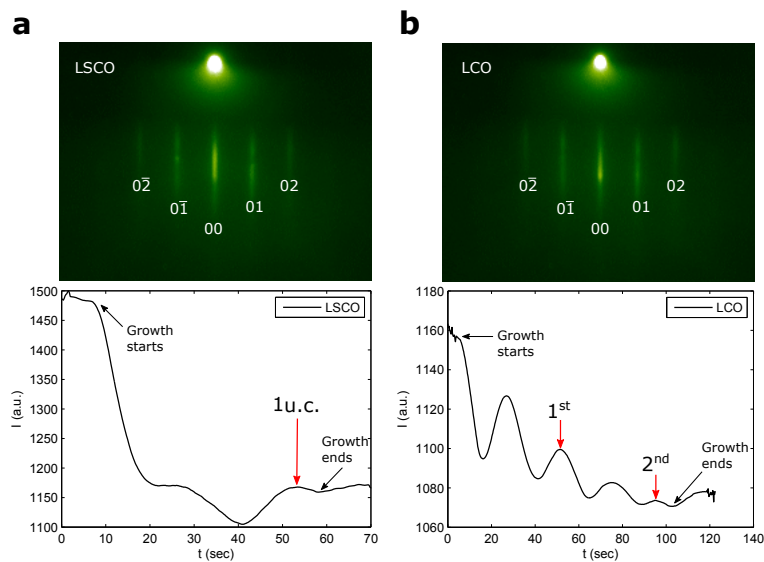


Figure 5.4: The RHEED pattern (upper panel) and time evolution of the average intensity of the (00) Bragg peak (lower panel) during the deposition of (a) 1 u.c. LSCO and (b) 2 u.c. LCO for a LSCO(1 u.c.)-LCO(2 u.c.)-BL\*. The red arrows mark the completion of unit cells.

### 5.1.3 Summary

The PLD technique has been used to prepare LSCO-LCO-BLs, LSCO-LCMO-BLs and LSCO-LCO-LCMO-TLs with atomically flat interfaces and surfaces. The thicknesses of the LSCO and LCO layers in the heterostructures were controlled with a precision on the sub-unit-cell level.

In pure N<sub>2</sub>O gas (growth mode A), the growth of the first LSCO monolayer next to the substrate follows a Stranski-Krastanov growth mode. For the following monolayers, the growth mode converts into a *layer-by-layer* mode. Accordingly, the first LSCO monolayer is expected to contain a significant amount of disorders. On the other hand, by using a mixture of N<sub>2</sub>O and O<sub>2</sub> gases (growth mode B), the growth of the LSCO layer follows right away the *layer-by-layer* mode, i.e., even for the very first monolayer. Inevitably, the first LSCO layer has now considerably less disorders.

## 5.2 Structural characterization of the thin films and heterostructures

The structural characterization of the thin films and heterostructures has been performed with x-ray diffraction measurements using a Rigaku SmartLab triple-axis diffractometer. The results are presented in the following.

### 5.2.1 Thin films

Figure 5.5 shows typical x-ray diffraction (XRD) patterns of thin films of 7 u.c. LSCO, 7 u.c. LCO and 20 u.c. LCMO films that are grown on (001)-oriented SLAO substrates. The XRD patterns were obtained using a symmetric scan mode, i.e., the momentum transfer was along the surface normal of the samples. Only the (00N)-peaks are identified, which confirms that the samples are epitaxial with the *c*-axis perpendicular to the sample surface. For LSCO and LCO, it means that the CuO<sub>2</sub> planes are parallel to the film surface. Despite the large lattice mismatch with the SLAO substrate, the LCMO film is also epitaxial. The sharp structural Bragg peaks for LSCO and LCO are indicative of the high crystalline quality of the samples. The relatively broader Bragg peaks for LCMO suggest that the crystalline quality is not as good as of LSCO or LCO. This is expected from the large lattice mismatch between the LCMO and SLAO, which results in a gradual strain relaxation during the growth. The intensity oscillations around the highly intense LSCO or LCO Bragg peaks demonstrate the low surface and interface roughnesses. The calculated *c*-axis lattice parameters ( $c^{\text{expt}}$ ) of the films are listed in Table 5.1. As a result of the compressive strain, the *c*-axis lattice parameters of the monolayers are larger than their bulk values.

	LSCO	LCO	LCMO
$c^{\text{expt}}$ (Å)	13.2719(14)	13.2096(19)	3.9865(22)
$c^{\text{bulk}}$ (Å)	13.1973	13.1172	3.8556

Table 5.1: Calculated *c*-axis lattice parameters ( $c^{\text{expt}}$ ) of 7 u.c. LSCO, 7 u.c. LCO and 20 u.c. LCMO including their bulk values ( $c^{\text{bulk}}$ ).

### 5.2.2 Heterostructures

The XRD patterns of the LSCO(5 u.c.)-LCO(2 u.c.)-BL, LSCO(5 u.c.)-LCMO(20 u.c.)-BL and LSCO(5 u.c.)-LCO(2 u.c.)-LCMO(20 u.c.)-TL are shown in Figure 5.7. The heterostructures are evidently epitaxial. As the LSCO and LCO have very similar lattice constants, their Bragg peaks are not distinguishable within the experimental resolution. The presence of intensity oscillations around the intense Bragg peaks confirms the sharp interfaces and low surface roughness. Figure 5.7 displays how the *c*-axis lattice parameters ( $c_{\text{LSCO}}^{\text{expt}}$ ) of the LSCO/LCO

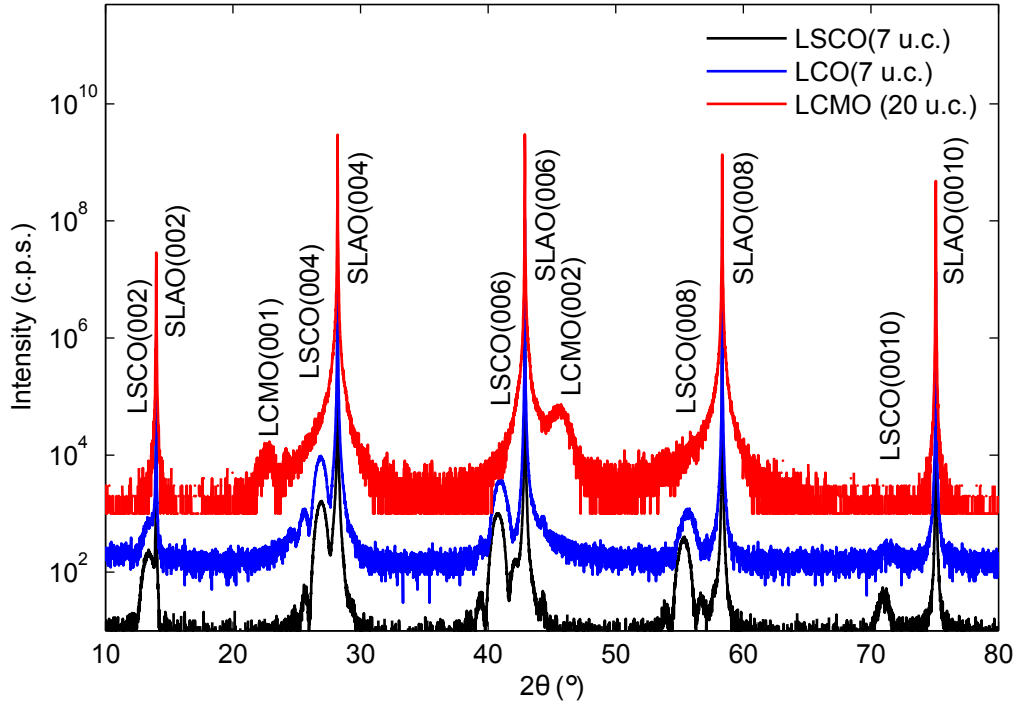


Figure 5.5: Symmetric  $\theta$ - $2\theta$  x-ray diffraction patterns of thin films of (a) 7 u.c. LSCO, (b) 7 u.c. LCO and (c) 20 u.c. LCMO grown on (001)-oriented SLAO substrates.

stackings in the heterostructures vary with the thickness of LSCO. It is found that the  $c_{\text{LSCO}}^{\text{expt}}$  parameters of the heterostructures are not very different.

Figure 5.8 depicts the reciprocal space maps (RSMs) of a LSCO(5 u.c.)-LCMO(20 u.c.)-BL and a LSCO(5 u.c.)-LCO(2 u.c.)-LCMO(20 u.c.)-TL. The (0 1 11) peaks for the LSCO and LCO layers in the trilayer could not be distinguished with the experimental resolution. In both heterostructures, the (0 1 N) peaks for the LSCO and the LSCO/LCO stacking are nearly symmetric around the  $k = 1$  lines, confirming that the layers are almost fully strained. In contrast, the LCMO layers in both samples are significantly strain relaxed. This is due to the 3% mismatch of the in-plane lattice constant of LCMO with respect to the substrate. The calculated in-plane lattice parameters ( $a^{\text{expt}}$ ) for LSCO and LCMO in the bilayer are 3.7619(3) and 3.8165(5) Å, respectively. In the trilayer,  $a^{\text{expt}}$  values of LSCO/LCO stacking and LCMO are 3.7692(7) and 3.8098(13) Å, respectively. The obtained in-plane lattice parameters are smaller than the corresponding bulk values. This is due to compressive strain from the substrate.

### 5.3 Electromagnetic properties of the thin films

In this section, the transport properties of the LSCO, LCO and LCMO films, and the magnetism of the LCMO are discussed. The transport properties were determined in terms of the resistance measurements using a conventional four-probe method with the four wires glued along a line on the sample surface with silver paint. The magnetization measurements were carried out with the VSM option of the QD-PPMS.

#### 5.3.1 LSCO

Figure 5.9a displays the resistance versus temperature (R-T) curve for a 7 u.c. thick LSCO film. The R-T curve shows that the sample is metallic at high temperature. It also reveals a rather sharp superconducting transition with  $T_C(R \rightarrow 0) \approx 33\text{K}$  and a width ( $\Delta T_C$ ) of

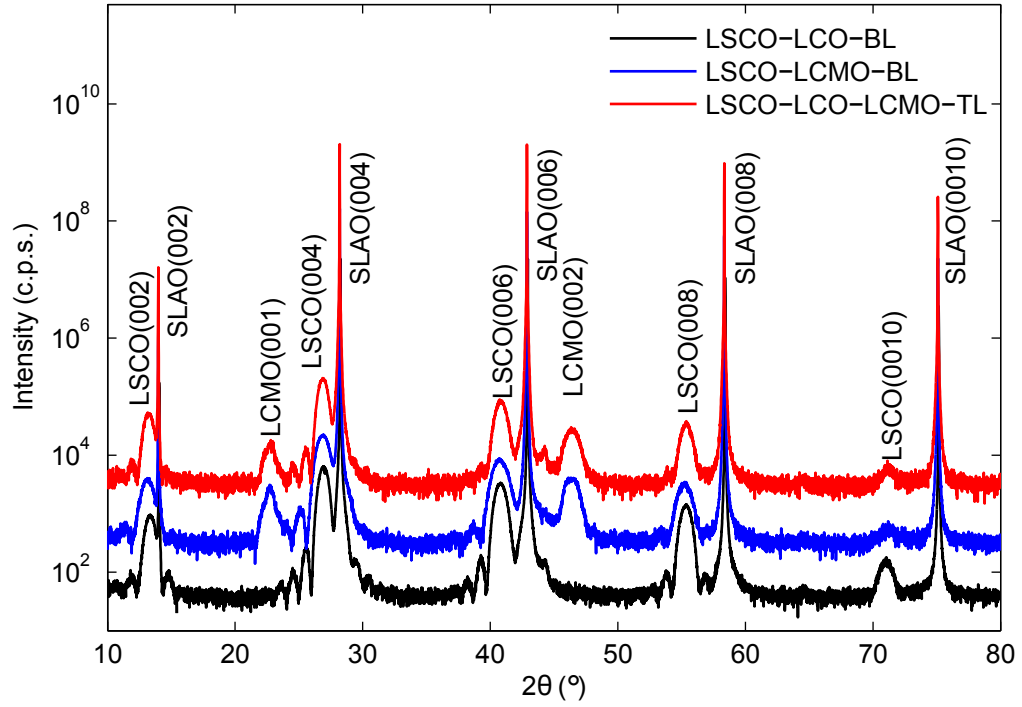


Figure 5.6: Symmetric  $\theta$ - $2\theta$  x-ray diffraction patterns of (a) LSCO(5 u.c.)-LCO(2 u.c.)-BL, (b) LSCO(5 u.c.)-LCMO(20 u.c.)-BL and (c) LSCO(5 u.c.)-LCO(2 u.c.)-LCMO(20 u.c.)-TL samples grown on (001)-oriented SLAO substrates.

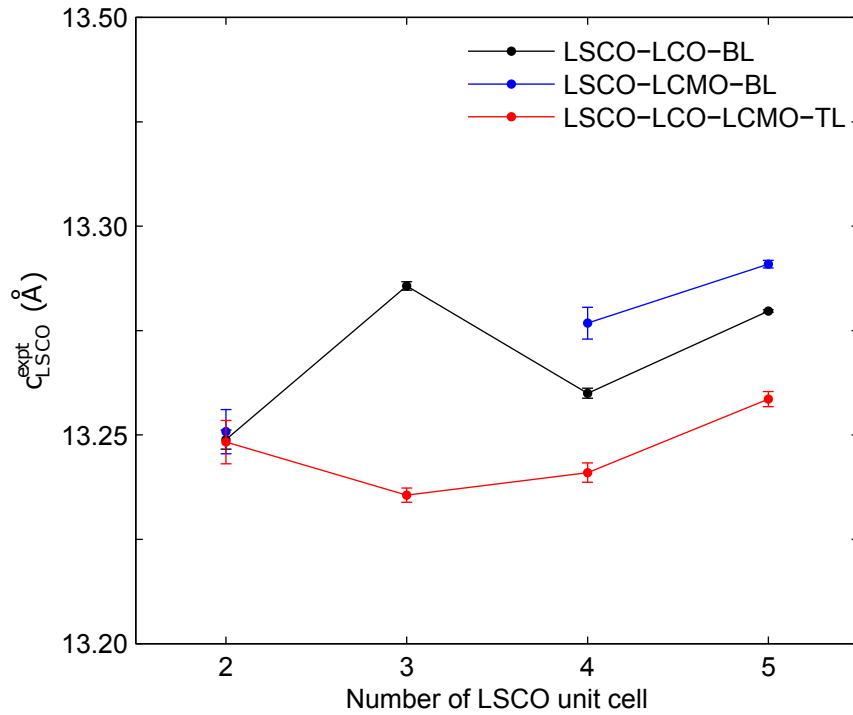


Figure 5.7:  $C$ -axis lattice parameters ( $c_{LSCO}^{expt}$ ) of the LSCO/LCO heterostructures for LSCO( $N$  u.c.)-LCO(2 u.c.)-BLs, LSCO( $N$  u.c.)-LCMO(20 u.c.)-BLs and LSCO( $N$  u.c.)-LCO(2 u.c.)-LCMO(20 u.c.)-TLs.

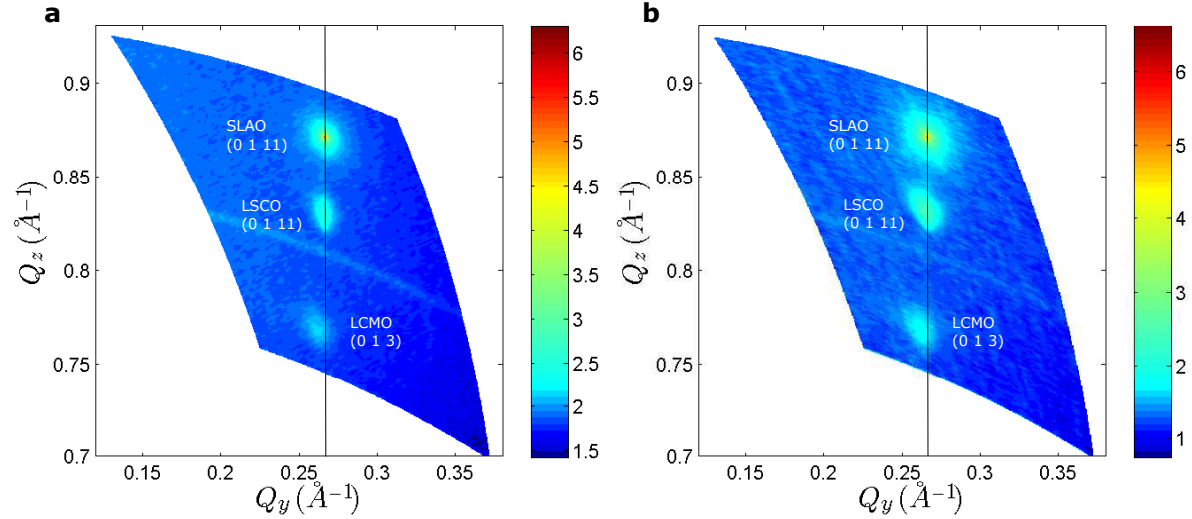


Figure 5.8: Reciprocal space maps (RSMs) around the (0 1 11) Bragg peak of the tetragonal SLAO substrates for (a) LSCO(5 u.c.)-LCMO(20 u.c.)-BL and (b) LSCO(5 u.c.)-LCO(2 u.c.)-LCMO(20 u.c.)-TL. The black lines show the location of  $k = 1$  for SLAO.

about 5 K. The onset of the transition occurs at  $T_{C,on} = 38$  K, i.e., very close to the one of the corresponding bulk LSCO. This confirms that the sample is stoichiometric and relatively free of defects. In addition, the sharp transition reaffirms that the sample is chemically and structurally homogeneous.

### 5.3.2 LCO

Figure 5.9b shows the R-T curve for a 7 u.c. thick LCO film in the range of 10-300 K. The inset of the figure presents the fitting of the R-T curve below 50 K with the 2D variable range hopping model (as detailed in Appendix D). Above 50 K, the resistance follows an Arrhenius law of thermal activation with a single activation energy.

A similar temperature dependence of the resistance has previously been reported for lightly doped  $\text{La}_{2-x}\text{Sr}_x\text{CuO}_4$  and  $\text{La}_2\text{CuO}_{4+\delta}$  [103, 104]. The comparison of the R-T curves suggests that in the LCO film, the source of holes is a small amount of excess oxygen with a concentration of about  $\delta = 0.001$  [104]. Such a small amount of excess oxygen seems feasible since the LCO film has been grown in  $\text{N}_2\text{O}$  gas which is known to supply sizeable amounts of reactive atomic oxygen.

The excess oxygen ions act as acceptors. The Arrhenius type conductivity in the high temperature regime arises from the thermal activation of these holes into the valence band which is made up from hybridized O- $p$  and Cu- $d$  states [103]. At low temperature, these holes are trapped to the acceptor levels, and can only hop between neighbouring sites as described by the 2D VRH model. The hopping is furthermore strongly influenced by the static antiferromagnetic (AF) correlations [105, 106].

### 5.3.3 LCMO

Figure 5.9c depicts the R-T curve of a 20 u.c. thick ( $\approx 8$  nm) LCMO film which was grown on a SLAO substrate. The system goes from a high temperature insulating state to a low-temperature metallic state with a metal-to-insulator (MIT) transition temperature of  $T_{MIT} = 150$  K. The suppression of  $T_{MIT}$  with respect to the bulk value of about 270 K [107] can be understood in terms of the compressive strain due to the lattice mismatch of about 3%. A partial strain relaxation can also account for the relatively large width of the MIT transition. The overall high resistance, even in the metallic state, indicates the reduced charge carrier density with respect to the stoichiometric bulk sample [108]. Since the RBS

measurement on similar film found no evidence of a Ca deficiency [98], it seems that a slight oxygen deficiency is responsible for the large resistance.

Figure 5.10 shows the temperature dependence of the field cooled magnetization (M-T) at 0.1 T and the magnetic hysteresis loop (M-H) at 3 K. Similar to  $T_{MIT}$ , the ferromagnetic transition temperature is also low with  $T^{Curie} \approx 190$  K. The average value of the low-temperature magnetization of  $2 \mu_B/\text{Mn}$  at 3 K is also rather small. All these results are consistent with a phase separated ground state that consists of a mixture of ferromagnetic metallic and antiferromagnetic insulating regions [109].

## 5.4 Impact of ferromagnetic LCMO on ultrathin LSCO

In this section, it is first of all shown that superconductivity (SC) exists in the LSCO films, even if the thickness is as small as two unit cells. In the following, it is discussed that SC is suppressed in the LSCO-LCMO-BLs as a result of the proximity effect with the ferromagnetic (FM) LCMO layer.

### 5.4.1 Superconductivity in ultrathin LSCO films

Figure 5.11 shows the R-T curves of the LSCO-LCO-BLs, for which the thickness of the LSCO layers is varied between 2-5 u.c. while the thickness of the LCO layer is kept constant at 2 u.c. Initially, the insulating 2 u.c. thick LCO layer was added as a capping layer to protect the ultrathin LSCO layer underneath from the degradation in contact with the ambient. Such a capping layer was proved to be essential for the comparative analysis of the R-T curves of different LSCO samples.

All the BLs exhibit metallic properties at high temperature, followed by a SC transition at low temperature. The presence of a clear SC response in the LSCO film (2 u.c.) testifies for the high structural and chemical quality of these samples. This is more remarkable, since the first monolayer of LSCO next to the substrate is considerably disordered, as is suggested by the time evolution of the RHEED intensity (see section 5.1). It is therefore likely that the SC in this LSCO (2 u.c.) sample arises from a single monolayer, i.e., the second one.

A remarkable feature in the R-T curves of these LSCO(N u.c.)-LCO(2 u.c.)-BLs is the upturn of the resistance toward low temperature that sets in before the SC transition, as is shown by the dashed arrows in Figure 5.11. This feature is commonly observed in underdoped cuprates [110], suggests a moderate localization of the charge carriers [111]. It is usually attributed to the disorder effects [112]. In thin films, the reduction of the thickness results in a gradual increase of the disorder. Such disorder may arise from the increased number of grain boundaries (GBs). The effect of such GBs on the charge conduction becomes prominent when the thermal fluctuations in the system are reduced toward low temperature. At intermediate temperatures, the transfer of charge carriers between two conducting grains happens mostly via the tunneling through the insulating GB which tend to be hole depleted. This process involves an electrostatic charging of the grains, and thus leads a thermally activated transport across the electrostatic barriers [113]. The gradual increase of the disorder in the thinner films enhances this activation behavior which consequently arises at higher temperature, as marked by the arrows in Figure 5.11.

The LSCO(N u.c.)-LCO(2 u.c.)-BLs exhibit a complete SC transition with a zero resistance state for  $N=3-5$  u.c. This indicates that their LSCO layers are homogeneous on a macroscopic scale (with a rather low level of disorder). However, for  $N=2$ , the SC transition remains incomplete since the resistance never reaches zero and even increases towards very low temperature. Such a behavior is typical for a granular superconductor, as is discussed in Refs. [114–116]. In the granular regime, the Josephson-coupling between the weak-links across the boundaries between the SC grains is so weak that a macroscopic phase coherence can not develop [117].

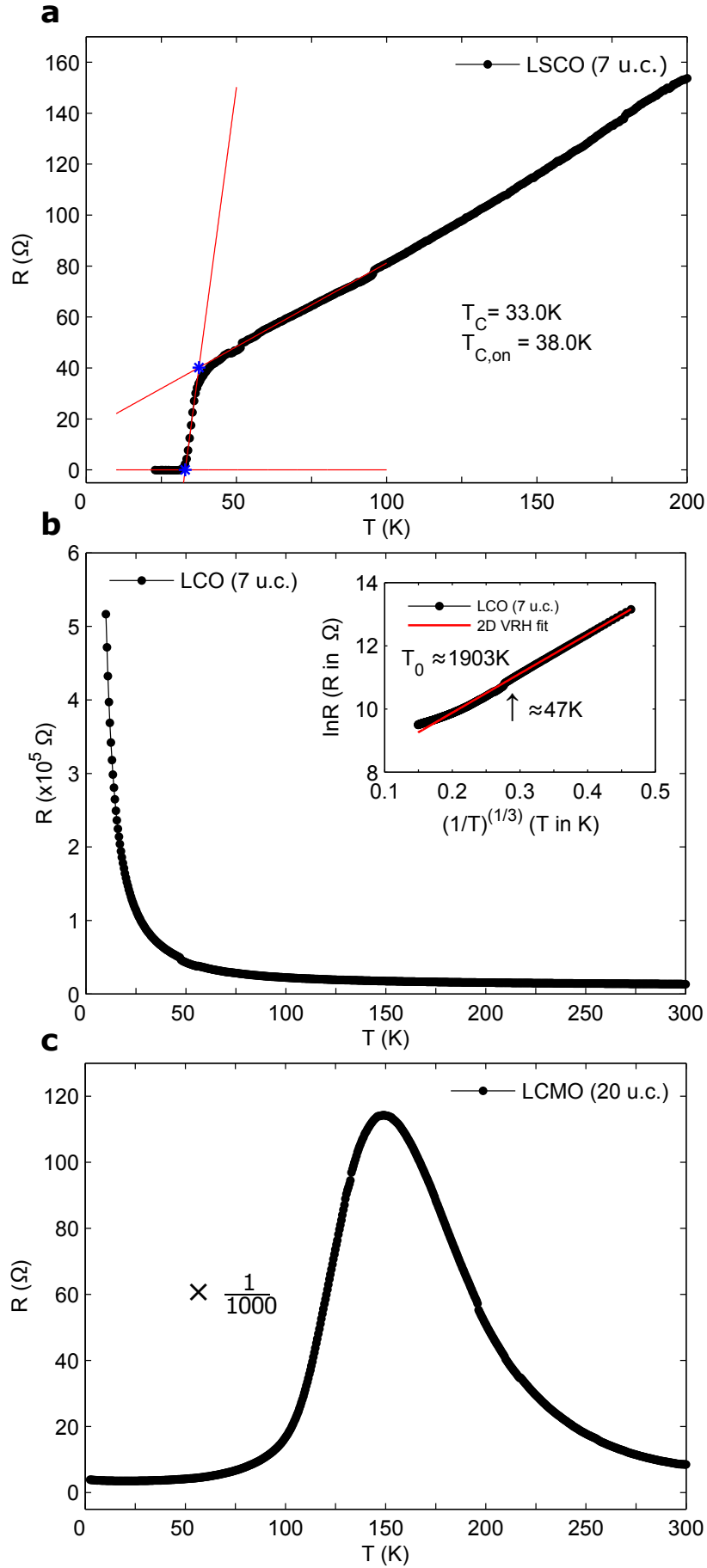


Figure 5.9: R-T curves of thin films of (a) LSCO(7 u.c.), (b) LCO(7 u.c.) and (c) LCMO(20 u.c.). Inset of (b) shows a fit of the low temperature resistance with the 2D VRH model according to the formula:  $\ln R = \ln R_0 + \left(\frac{T_0}{T}\right)^{\frac{1}{3}}$ .

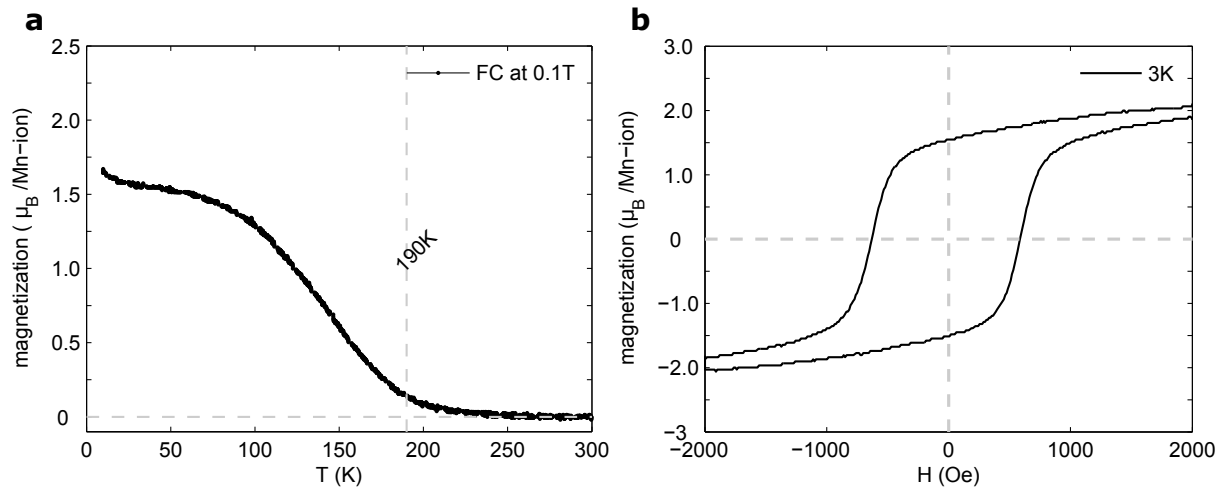


Figure 5.10: (a) Temperature dependence of the field cooled magnetization at 0.1 T of a LCMO (20 u.c.) film. (b) M-H loop of this film at 3 K after field cooling at 9 T.

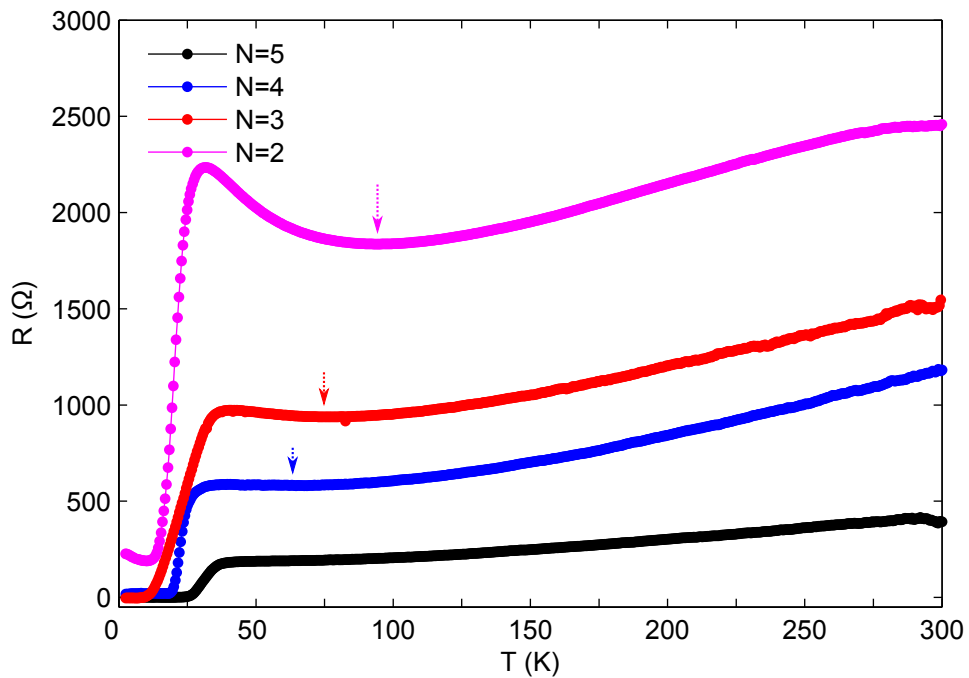


Figure 5.11: R-T curves of LSCO( $N$  u.c.)-LCO(2 u.c.)-BLs. The dashed arrows mark the onset of the charge carrier localization that occurs above the superconducting transition.

### 5.4.2 Suppression of superconductivity in LSCO/LCMO bilayers

Figure 5.12 displays the R-T curves of the LSCO-LCMO-BLs for which the thickness of the LSCO layer varies between 2 and 5 u.c., and the thickness of the LCMO layers is fixed at 20 u.c. In comparison to the LSCO-LCO-BLs (see Figure 5.11), in these LSCO-LCMO-BLs, there is a clear reduction of  $T_C$ . The LSCO (2 u.c.) layer in the LSCO-LCO-BL is still superconducting, whereas in the corresponding LSCO-LCMO-BL the superconductivity is completely suppressed. The 2 and 3 u.c. thick LSCO layers in the LSCO-LCMO-BLs also seem to be only poorly metallic. As a result, at high temperature the corresponding R-T curves are dominated by the metal-to-insulator transition in the LCMO layer. Such an enhancement of the high-temperature resistance of the cuprate layer has also been reported by S. Soltan *et al.* for similar SC/FM BLs which contain YBCO instead of LSCO [118]. They discussed this finding in terms of an enhanced scattering in the cuprate layer due to a diffusion of the spin polarized quasiparticles from the FM LCMO layer.

The critical currents ( $I_C$ ) for the LSCO(5 u.c.)-LCO(2 u.c.)-BL and the LSCO(5 u.c.)-LCMO(20 u.c.)-BL were obtained from their voltage vs. current (V-I) characteristics at 4 K, as shown in Figure 5.13a. A detailed description of these V-I measurements can be found in Appendix E. They show that the  $I_C$  of the LSCO-LCO-BL is considerably larger than the one of the corresponding LSCO-LCMO-BL with values of  $I_C = 4.5$  mA and 2 mA, respectively. The obtained critical current density ( $j_c$ ) is about  $8.6 \times 10^3$  A/cm<sup>2</sup> for the LSCO(5 u.c.)-LCO(2 u.c.)-BL sample. In bulk LSCO, the  $j_c$  could reach  $10^5$ - $10^6$  A/cm<sup>2</sup> [119]. The difference in the value of  $j_c$  may come from the measurement technique, crystal grain size, amount of disorders, etc.

Figure 5.13b compares the evolution of the zero resistance temperature ( $T_C$ ) vs. the thickness of the LSCO layer in terms of monolayers (u.c) for the LSCO(N u.c.)-LCO(2 u.c.)-BLs and the LSCO(N u.c.)-LCMO(20 u.c.)-BLs. It appears that in these ultrathin LSCO layers, the  $T_C$  value is almost proportional to N. It is also found from the plot that the  $T_C$  value of LSCO(N u.c.) layer in the LSCO-LCMO-BLs is almost equal to the one of a LSCO(N-1 u.c.) layer in the LSCO-LCO-BLs. This suggests that the proximity effect with the FM LCMO layer gives rise to a suppression of SC in the LSCO monolayer next to the interface. In the following, we discuss the origin of the suppression of SC and  $I_C$  in these LSCO-LCMO-BLs.

As described in section 2.2, the optimally doped LCMO is a FM with fully spin-polarized charge carriers. In section 5.3, it was shown that a 20 u.c. thick LCMO layer is indeed already a strongly FM. It is well known that the SC and FM are two antagonistic phenomena [1, 14, 16, 21, 24, 97]. One possible mechanism for the suppression of SC is the injection or diffusion of itinerant spin-polarized charge carriers from LCMO into LSCO [118]. This mechanism can be strong enough to break the Cooper pairs in the vicinity of the interface [120]. In addition, the smaller chemical potential of LSCO as compared to the one of LCMO instigates a transfer of electrons from LCMO into LSCO, which reduces the hole doping of LSCO [91, 121], and thus leads to the suppression of the  $T_C$ . Furthermore, the Cu and Mn ions at the LSCO/LCMO interface are antiferromagnetically coupled [98]. It has been demonstrated that the effect of this magnetic exchange coupling on the suppression of SC can be stronger than the one due to the injection of spin-polarized charge carriers [31]. One way or the others, these different effects all contribute to the suppression of SC in the LSCO layer that is in contact with the FM LCMO layer. The pair breaking effects in the LSCO-LCMO-BL can also explain the suppression of the critical current [122].

## 5.5 Transport properties of LSCO/LCO/LCMO trilayers

In this section, we focus on the question whether an insulating LCO layer with a thickness of 2 u.c. can lead to an electronic and magnetic decoupling between LSCO and LCMO in LSCO/LCO/LCMO trilayers.

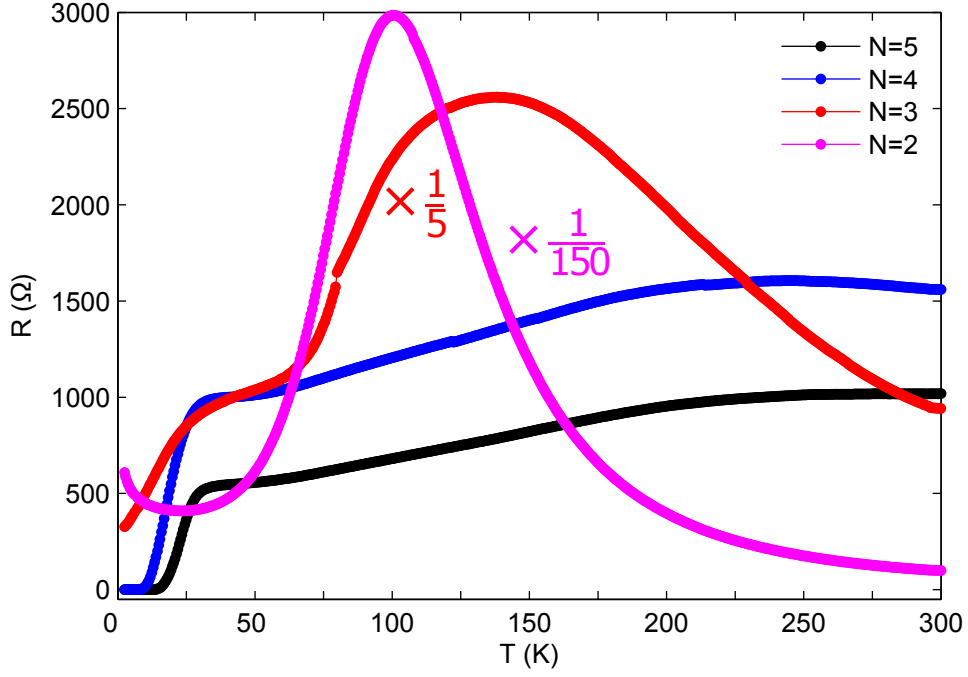


Figure 5.12: R-T curves of the LSCO(N u.c.)-LCMO(20 u.c.)-BLs.

### 5.5.1 Experimental results

Figure 5.14 displays the R-T curves of the LSCO(N u.c.)-LCO(2 u.c.)-LCMO(20 u.c.)-TLs as function of the thickness of the LSCO layers. It is evident that the suppression of SC in these TLs is even stronger than in the LSCO-LCMO-BLs. The TLs with 2 and 3 u.c. of LSCO have insulator-like R-T curves and do not show any sign of a SC transition. Instead, their resistance increases steeply toward low temperature. This resistance upturn suggests that in these TLs the LCMO layers are also not metallic. This has been verified by growing a LCO-LCMO-BL in which the LCO and LCMO layers are 2 and 20 u.c. thick, respectively. This BL exhibits indeed an insulator-like R-T curve that is well described by an Arrhenius-like activation with a single activation energy of 0.11 eV (see Appendix F). It appears that the dome-shaped R-T curve of the TLs with four and five monolayers of LSCO layers do not arise from a metal-to-insulator transition of the LCMO layers, but rather represent the convoluted responses from the metallic LSCO and the insulating LCO/LCMO stackings.

### 5.5.2 Discussion

To understand the conduction mechanism of the highly insulating samples in the low temperature region, the R-T curves have been fitted with the 2D VRH model, as shown in Figure 5.15. These fits show that the R-T curves for the TLs with the 3 and 2 u.c. thick LSCO layers follow the 2D VRH model below about 45 and 32 K, respectively. Coincidentally, the LSCO layers in the corresponding LSCO-LCO(2 u.c.)-BLs become superconducting in this temperature range. The good quality of the fits supports our interpretation that the charge carriers in these TLs are localized in the low-temperature regime, where in the absence of the LCO spacer layer, they would be superconducting. However, based on this 2D VRH model, we can not tell whether the localized state is composed of normal carriers or even Cooper pairs.

It is well known that such a localization of the charge carriers can be induced by structural distortions of the  $\text{CuO}_2$  planes or by other competing interactions, like an external magnetic field, FM or AF exchange interaction etc., which tend to stabilize a competing charge order or stripe phase, and lead to a phase segregation with conducting islands that are embedded in an insulating matrix [114, 117, 123–126].

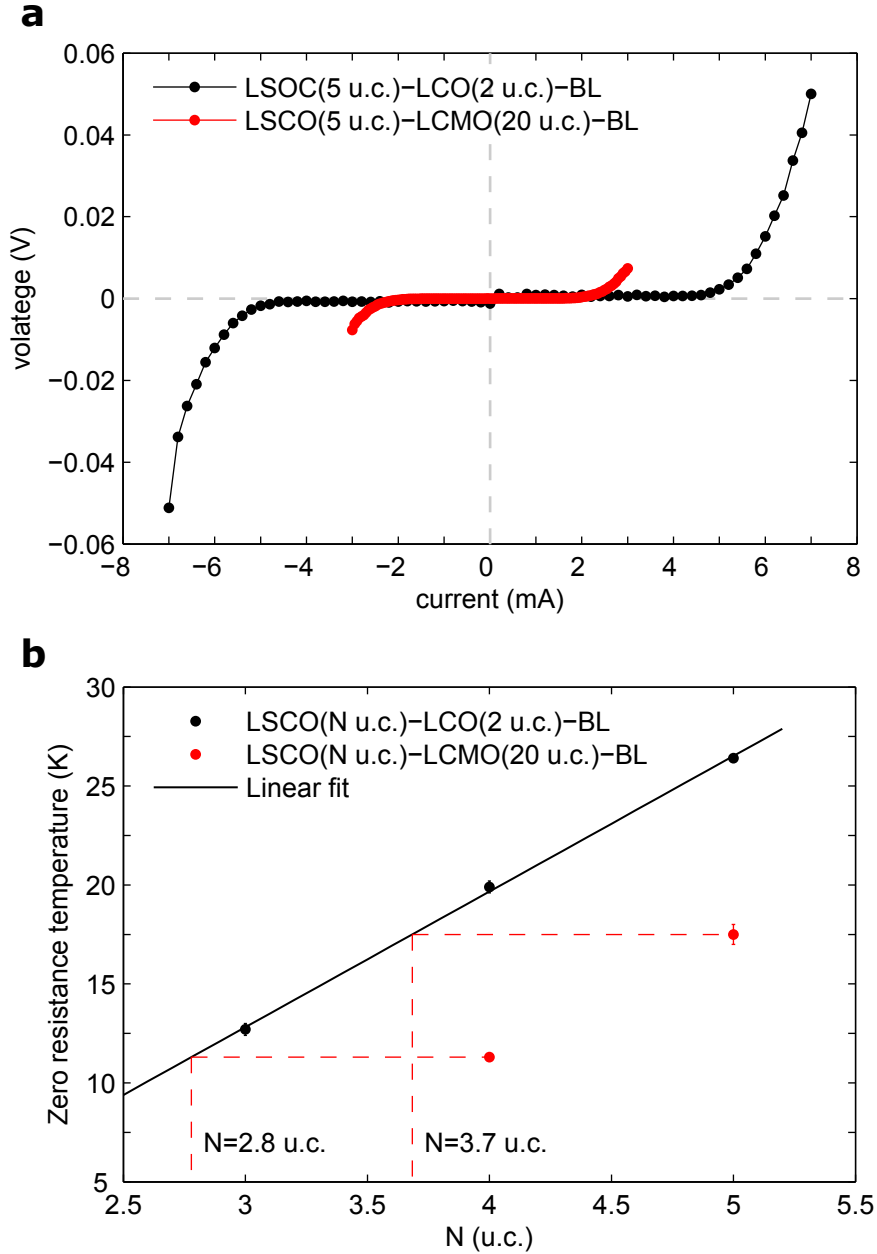


Figure 5.13: **(a)** Voltage vs. current characteristics of LSCO(5 u.c.)-LCO(2 u.c.) and LSCO(5 u.c.)-LCMO(20 u.c.) BLs at 4K and in zero magnetic field. **(b)** Zero resistance temperature ( $T_C$ ) vs. the number ( $N$ ) of LSCO monolayer for the LSCO( $N$  u.c.)-LCO(2 u.c.) and LSCO( $N$  u.c.)-LCMO(20 u.c.) BLs. The solid black line is the best linear fit of the  $T_C$  vs.  $N$  characteristic of the LSCO( $N$  u.c.)-LCO(2 u.c.)-BLs in the ultrathin limit of LSCO.

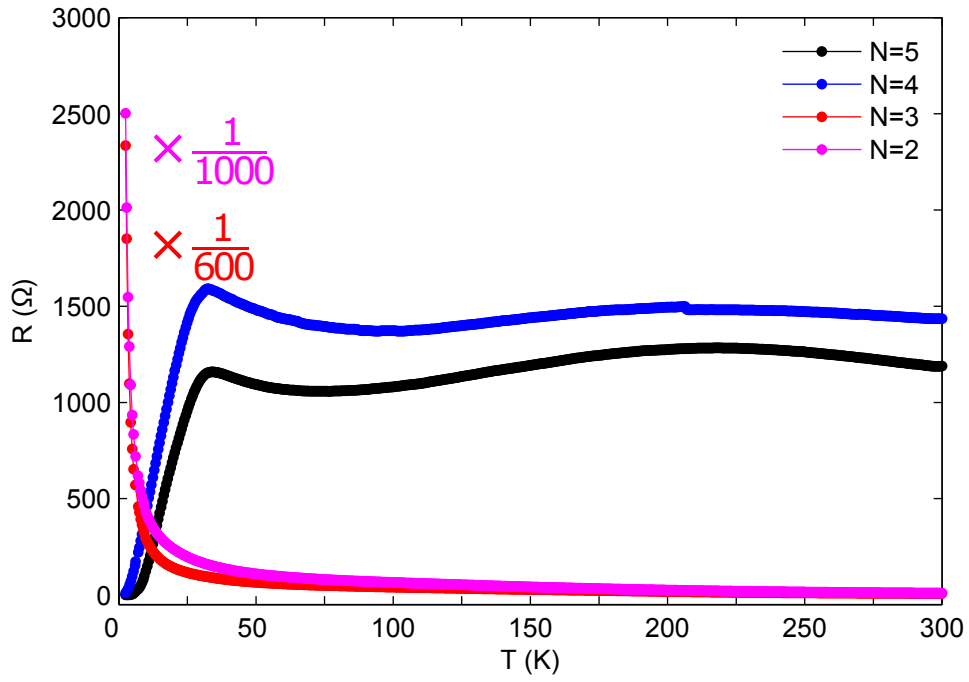


Figure 5.14: R-T curves of LSCO(N u.c.)-LCO(2 u.c.)-LCMO(20 u.c.)-TLs with different thickness of LSCO.

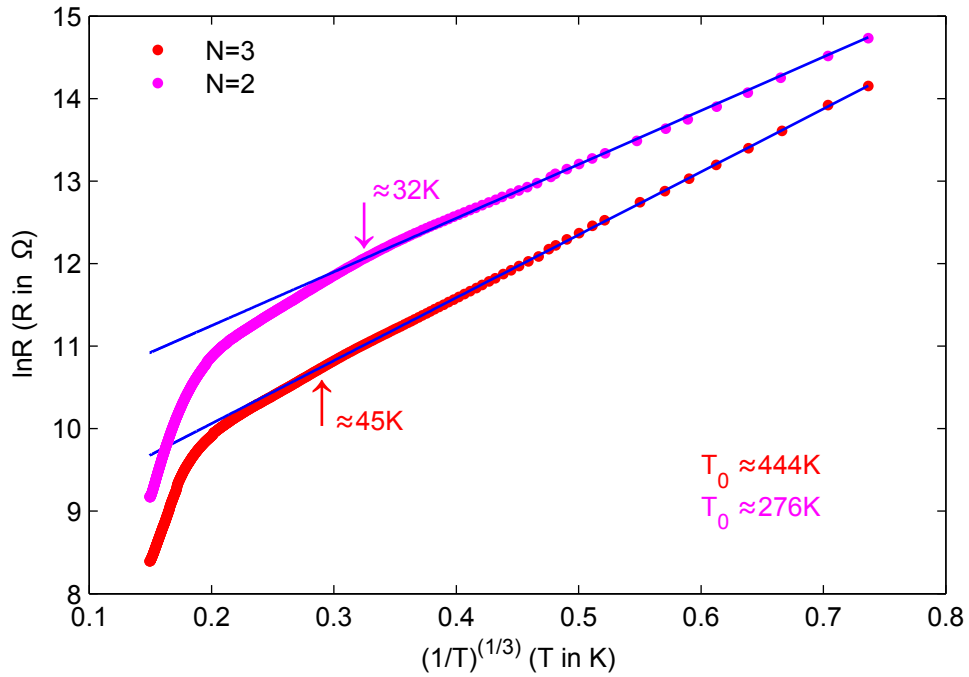


Figure 5.15: 2D VRH fitting of the R-T curves of the LSCO(N u.c.)-LCO(2 u.c.)-LCMO(20 u.c.)-TLs with the formula:  $\ln R = \ln R_0 + \left(\frac{T_0}{T}\right)^{\frac{1}{3}}$ .

## 5.6 Origin of the charge carrier localization

In this section, we show that a similar charge carrier localization is also found in LSCO-LCO-BLs. In this context, we discuss the possible origins of such a localization phenomenon.

### 5.6.1 Charge carrier localization in LSCO/LCO bilayers

Figure 5.16 depicts the R-T curves of two LSCO(3 u.c.)/LCO(M u.c.) BLs with M=2 and 7. In the high temperature regime, these BLs exhibit a rather similar metallic behavior. However, clear differences in the R-T characteristics occur upon cooling in the low temperature regime. These are most striking below about 40 K where the M=2 sample undergoes a SC transition, whereas the M=7 sample exhibits a steep insulator-like increase of the resistance. The low-temperature R-T curve is well described by a 2D VRH (as shown in Appendix G) which is characteristic of a weak localization of the charge carriers. These observations raises the question about the charge carrier localization in the LSCO(3 u.c.)-LCO(7 u.c.)-BL. There are several potential mechanisms, such as (i) a strain-effect due to the LCO layer, (ii) a strong underdoped state of LSCO due to oxygen vacancies or a long-range charge transfer from LSCO to LCO, and (iii) an AF proximity effect.

As to point (i), it has been shown that a complete suppression of SC and a similar localization of the carriers occurs in  $\text{La}_{1.8-x}\text{Eu}_{0.2}\text{Sr}_x\text{CuO}_4$  single crystals with  $x < 0.15$ . In this system the smaller size of the  $\text{Eu}^{3+}$  ions, as compared to  $\text{La}^{3+}$ , gives rise to an enhanced tilting of the  $\text{CuO}_6$  octahedra and a structural phase transition from the low-temperature-orthorhombic (LTO) to the low-temperature-tetragonal (LTT) phase [123]. It has been shown in Ref. [123] that the critical parameter is the rotation of the  $\text{CuO}_6$  octahedra. At a critical angle of about  $3.6^\circ$ , there is a transition from the superconducting state to an insulating static stripe order. This AF stripe order persists up to a doping level of  $x = 0.18$ . A similar tilting of the  $\text{CuO}_6$  octahedra may occur in the LSCO(3 u.c.)-LCO(7 u.c.)-BL. It may for example arise from the strain gradient in the LSCO layer which is clamped between the substrate which exerts a compressive strain and the LCO layer which gives rise to tensile strain with an intrinsic lattice mismatch of -0.5% and 0.7%, respectively. This strain gradient may also lead to misfit dislocations in the ultrathin LSCO layer, which can lead to the pinning of collective modes such as stripe order, charge or spin density waves, and thus the suppression of SC [127]. This strain gradient can be expected to be significantly small for the LSCO(3 u.c.)-LCO(2 u.c.)-BL, for which the LCO layer is much thinner, and thus may adapt the unit cell volume of the underneath LSCO layer due to the ‘Madelung strain’ [128].

Concerning point (ii) the underdoping of the LSCO layer due to the oxygen vacancies, Sr-interdiffusion or a massive transfer of holes into the LCO layer, the following can be said. One may suspect that the thicker ( $\approx 9$  nm) LCO layer is blocking the oxygen diffusion into the LSCO layer during the *in-situ* annealing of the BL. Such a scenario is however not consistent with the SC response of a LSCO(2 u.c.)/ $\text{La}_{1.94}\text{Sr}_{0.06}\text{CuO}_4$ (7 u.c.) (see Appendix I) and a LSCO(3 u.c.)/LCMO(20 u.c.) (see Figure 5.12) bilayers for which the topmost layers have similar thicknesses. The extended duration of the *in-situ* annealing procedure also makes the interpretation in terms of oxygen vacancies unlikely. The scenario of an interdiffusion of Sr into the LCO layer is also unlikely. Such an intermixing would be confined to the interface region, and thus would not depend on the thickness of the LCO layer on top of LSCO. These leaves us with the scenario of a long-range charge transfer from LSCO to LCO. A complete delocalization of the hole over the entire LSCO(3 u.c.)-LCO(7 u.c.)-BL would result in an average hole doping of 0.045 per  $\text{CuO}_2$  plane, and thus can explain the charge localization at low temperature [33]. However, this scenario is in contradiction with a superlattice consisting of LCO and  $\text{La}_{1.64}\text{Sr}_{0.36}\text{CuO}_4$ , where it was found that the transfer of holes from  $\text{La}_{1.64}\text{Sr}_{0.36}\text{CuO}_4$  to LCO involves a length scale of only about 6 Å which is less than one unit cell [129]. Moreover, it has been reported in Ref. [130] that the chemical potentials of LSCO (0.15% Sr doping) and LCO layers are essentially equal which means that no charge transfer across the LSCO/LCO interface will occur.

Finally, as to point (iii), there is the possibility of an AF proximity effect due to the long range AF order in the LCO layer. It was reported that the LCO layers exhibit such a static AF order only if their thickness exceeds a threshold value of about 2.5 monolayers [34]. The absence of the AF order in the very thin LCO layers has been explained in terms of quantum fluctuations which are strongly enhanced by the reduced dimensionality. By analogy, this implies that a static AF order occurs only in the LCO layer of the BL with  $M=7$ , but not for the one with  $M=2$ . The AF exchange coupling across the LSCO/LCO interface thus can be much stronger for  $M=7$  than for  $M=2$ . This AF proximity effect, albeit it is expected to be fairly weak [131], can enhance the AF correlations and slow down the corresponding fluctuations of the optimally doped LSCO. Since it is well known that the charge dynamics is strongly affected by the AF correlations, a slowing down and eventual freezing of the AF fluctuations in the vicinity of the LSCO/LCO interface may well explain that the charge localization occurs at a substantially higher hole concentration than in the bulk.

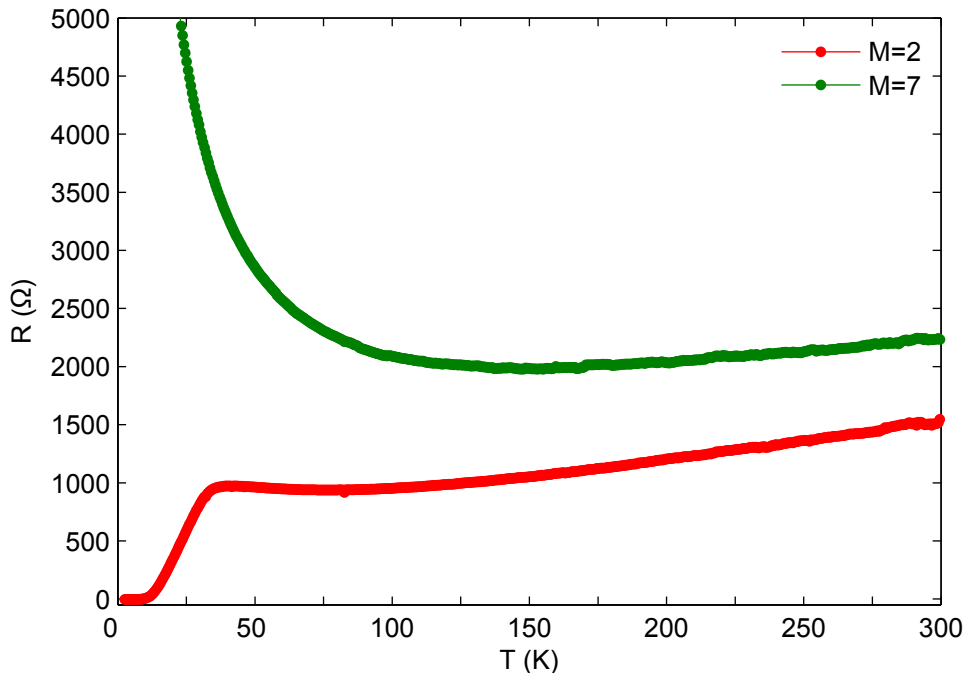


Figure 5.16: R-T curves of LSCO(3 u.c.)-LCO(M u.c.)-BLs for  $M=2$  and  $M=7$ .

### 5.6.2 Magneto-transport in the hopping regime

Figure 5.17 shows the in-plane magneto-resistance (MR) measured at 10 K with the magnetic field along the directions parallel ( $H\parallel ab$ ) and perpendicular ( $H\parallel c$ ) to the  $\text{CuO}_2$  planes. The direction of the electric current was always perpendicular to the magnetic field. The sign of the MR is positive and negative for  $H\parallel c$  and  $H\parallel ab$ , respectively. Such a sign change of the MR suggest that two different mechanisms are governing the charge transport in the low temperature hopping regime.

The first mechanism involves a magnetic field induced reorientation of the Cu spin. The Cu spins in the  $\text{CuO}_2$  planes are antiferromagnetically coupled via strong exchange interaction. But, the AF coupling between the spins in the neighboring layers is very weak [42]. In orthorhombic phase, the Dzyaloshinsky-Moriya interaction leads to a canting of the spins along the  $c$ -axis direction, which gives rise to an out-of-plane ferromagnetic component of the Cu spins. The weak interlayer AF exchange coupling between the  $\text{CuO}_2$  planes give rise to an AF alignment of these weak ferromagnetic (WF) moments. A large applied magnetic field along the  $ab$ -plane leads to a gradual rotation of the Cu spins and eventually a spin-flip transition for which the staggered moments are directed along the  $c$ -axis, whereas the WF moments are

aligned along the field direction [132, 133], as schematically shown in Figure 5.18. This FM alignment of the WF moments in the neighboring planes allows the interlayer hopping of the localized holes. As a result, the hopping probability increases, and a negative MR (n-MR) is obtained [133, 134].

The second mechanism involves the Zeeman effect of the magnetic field on the spin of the doped holes which can explain the positive MR (p-MR) that is observed for the  $H\parallel c$ -axis configuration. This p-MR is not so commonly observed in the strongly underdoped cuprates. It seems to be enhanced in disordered samples [135, 136] for which, in the presence of a strong Coulomb repulsion between two holes in the localized state, the Zeeman splitting gives rise to the p-MR [137]. Raičević *et al.* reported such a p-MR in  $\text{La}_{1.97}\text{Sr}_{0.03}\text{CuO}_4$  single crystal [138]. At this doping level, the 3D long-range AF order breaks down, and a (cluster) spin glass state emerges. The authors argued that the coupling of the applied magnetic field to the spin of the doped holes results in such p-MR. The magnetic background appears to be unimportant for the observed p-MR. This is consistent with the picture of ‘charged stripes’, where the holes reside only at the AF domain walls [139], and can give rise to the observed p-MR.

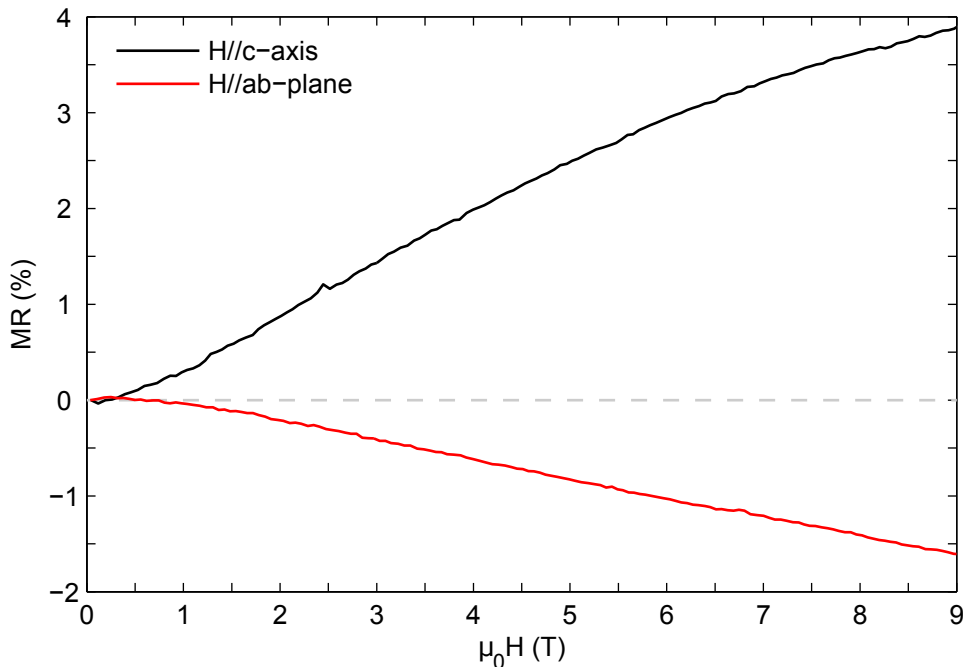


Figure 5.17: Magneto-resistance (MR),  $\frac{R(H)-R(0)}{R(0)}$  curves of a LSCO(3 u.c.)-LCO(7 u.c.)-BL measured at 10 K with the field ( $H$ ) applied either along the  $c$ -axis or the  $ab$ -plane of the sample.

### 5.6.3 Summary

The charge carriers in the LSCO(3 u.c.)-LCO(M=7 u.c.)-BL get localized at low temperature, whereas in a corresponding LSCO(3 u.c.)-LCO(M=2 u.c.)-BL they form a coherent superconducting state. To explain the localization behavior of the M=7 sample, we discussed three possible scenarios. A central aspect of the first scenario is the strong AF correlations of the Cu spins which persist into the superconducting regime of the doping phase diagram in the form of AF fluctuation. These AF correlations can be strongly affected by lattice distortions which lead to a buckling of the  $\text{CuO}_2$  planes and by various kinds of defects which tend to restore a short-range AF order that gives rise to a spatially inhomogeneous state of hole-rich regions that are separated by AF ordered domains. The second scenario would involve a massive charge transfer of holes across the LSCO/LCO interface such that the hole concentration in both layers become similar and corresponds to a strongly underdoped state with  $x = 0.045$ .

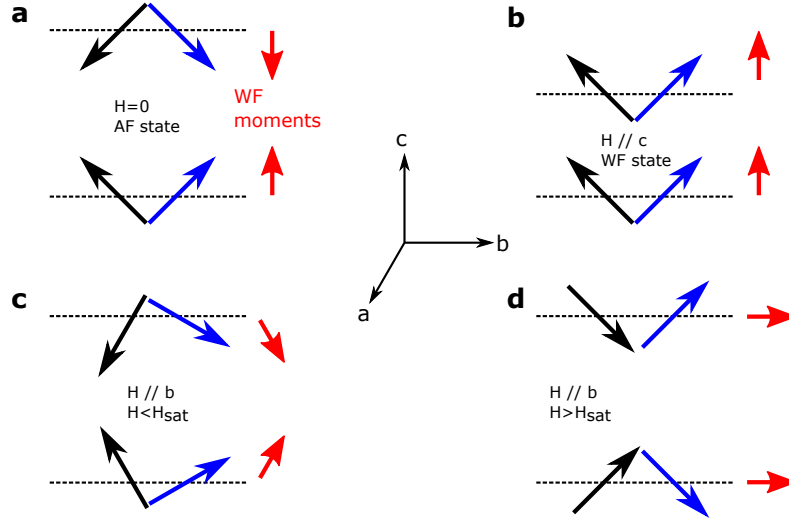


Figure 5.18: A schematic diagram showing how the canted, weak ferromagnetic (WF) moments in the adjacent CuO<sub>2</sub> planes respond to an applied magnetic field. (a) 3D AF arrangement of the Cu spins at zero field. (b) A strong applied strong field along the  $c$ -axis orients the canted WF moments. (c) An applied field along the  $b$ -axis gradually aligns the WF moments along this direction. (d) An extreme case where the WF moments are fully aligned along the  $b$ -direction. The diagram is adapted from Ref. [132].

Previous work by other groups on the charge transfer in such LSCO/LCO multilayers does not support this second scenario, since it shows that the charge transfer is limited to a length scale of less than one monolayer and occurs only for the doping level of the LSCO layer with  $x > 0.18$ . The third scenario involves an occurrence of a strong AF correlations in the LSCO layer near the LSCO/LCO interface in the presence of a static AF order in the capping LCO layer of 7 u.c. thick.

## 5.7 Further studies of charge carrier localization

In this section, we show that the observed charge carrier localization is a reproducible phenomenon. The new set of BLs, labeled as LSCO-LCO-BLs\*, was grown in a mixture of N<sub>2</sub>O and O<sub>2</sub> gases (growth mode B). This helped to achieve SC state even for a LSCO layer with a thickness of only 1 u.c.

### 5.7.1 Superconductivity in 1 u.c. thick LSCO

Figure 5.19 displays the R-T curves of the LSCO(N u.c.)-LCO(2 u.c.)-BLs\* for which the thickness of the LSCO layer is varied between 1 and 5 u.c. All the samples are metallic at high temperature, and show a SC transition at low temperature. The samples for N=5, 3 and 2 u.c. exhibit values of  $T_{C,on}$  and  $T_C$  around 35 and 22 K, respectively. For the LSCO(1 u.c.)-LCO(2 u.c.)-BL\*, a moderate localization is evident at temperatures somewhat above  $T_{C,on} \approx 20$  K. This localization, and the finite value of the resistance down to about 2 K suggest that the 1 u.c. thick LSCO is homogeneously disordered. The disorder may arise from the increased number of grain boundaries (GBs) in the ultrathin film.

This contrasts with the minimum thickness of 2 u.c. LSCO for superconductivity to occur in the LSCO-LCO-BLs that were grown in pure N<sub>2</sub>O gas, i.e., growth mode A (see subsection 5.4.1). This striking difference in the transport properties of these two types of bilayer samples (BL and BL\*) can be readily understood from their different growth modes in the two gas environments. It was shown for the LSCO-LCO-BLs\* that the growth of the LSCO layer follows an almost *layer-by-layer* mode since from the very first u.c., which directs to the minimal disorder in the 1 u.c. thick LSCO (see subsection 5.1.2). To the contrary, the first

u.c. of the LSCO layer in the LSCO-LCO-BLs is expected to have a significant amount of disorder, as is discussed in subsection 5.1.1.

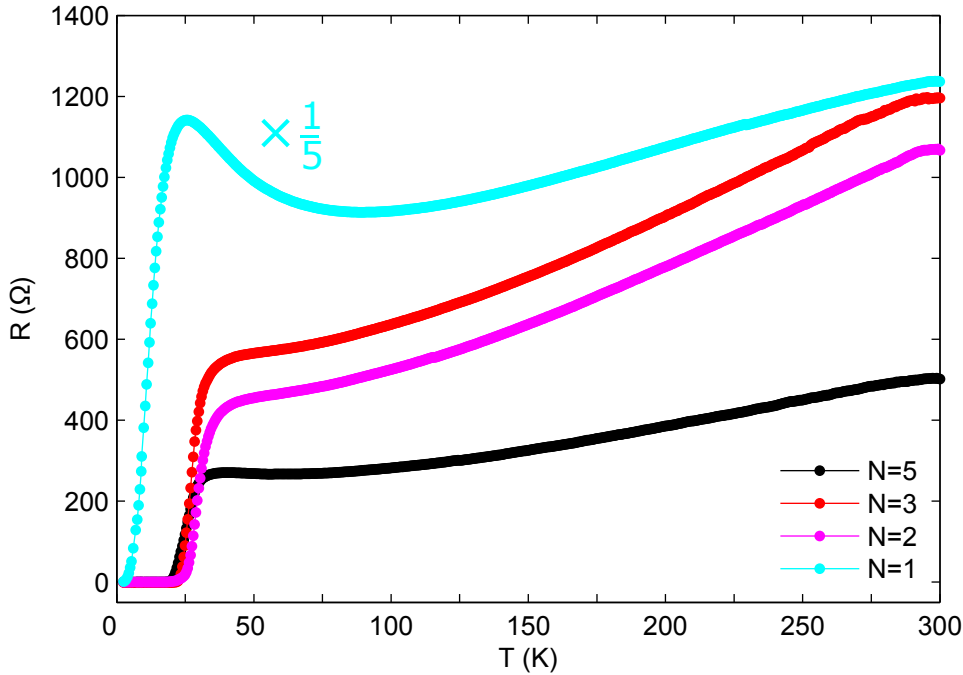


Figure 5.19: Temperature dependent resistance of LSCO( $N$  u.c.)-LCO(2 u.c.)-BLs\* grown in the mixture of  $N_2O$  and  $O_2$  gas (growth mode B).

### 5.7.2 Impact of a thicker LCO layer on superconductivity

Figure 5.20a-d summarizes the R-T curves of the LSCO films of various thicknesses with the LCO capping layers of 2 and 7 u.c. The R-T curves are normalized with respect to the resistance at 300 K for a comparative analysis. Figure 5.20a shows that the transport property of the 5 u.c. thick LSCO layer does not depend on the thickness of the LCO capping layer. The resistance upturn below  $T_C$  for the  $M=7$  sample arises most likely from the highly resistive LCO layer, since the resistance was measured by attaching four contacts on the surface of the LCO layer. For the sample with 3 u.c. of LSCO, the thicker LCO layer with  $M=7$  leads to a slight suppression of the SC transition, as shown in Figure 5.20b. A moderate charge carrier localization just above the SC transition is observed in the LSCO(3 u.c.)-LCO(7 u.c.)-BL\*. This suggests that some kind of AF correlations are induced in the LSCO layer due to the coupling with the thick LCO layer. For the samples with the 2 u.c. thick LSCO layer, the 7 u.c. thick LCO capping layer does already suppress macroscopic SC, only a granular SC seems to emerge (see Figure 5.20c). This is possibly a result of the weak coupling between the SC grains in the presence of a static AF order. Also, the moderate charge localization is present above  $T_{C,on}$ . The static AF order, as a result of the thick LCO layer, destroys the SC in the 1 u.c. thick LSCO layer, and gives rise to a strong localization of the charges carriers. At the low temperature regime, the conduction mechanism of the localized charge carriers follows the 2D VRH model (as shown in Appendix H).

In comparing the four cases in Figure 5.20, it appears that a static AF order seems to be induced at the LSCO/LCO interface due to the 7 u.c. thick LCO layer. For the bilayer samples with  $N=1-3$ , a moderate carrier localization in the normal state occurs around a similar temperature of 200 K. This temperature may also mark the onset of the static AF order at the LSCO/LCO interface.

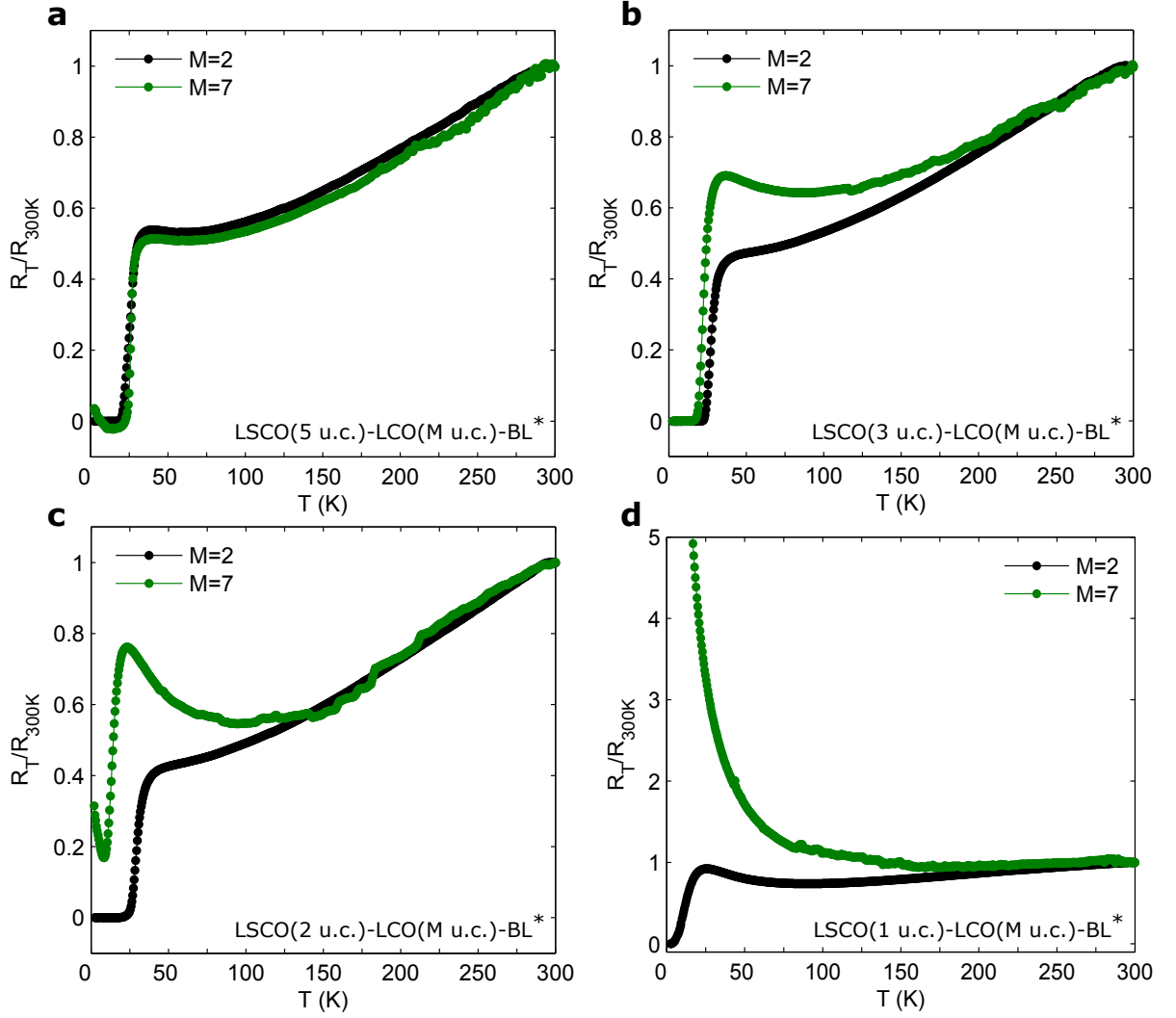


Figure 5.20: Temperature dependent normalized resistance ( $R_T/R_{300K}$ ) of (a) LSCO(5 u.c.)-LCO(M u.c.)-BL\*, (b) LSCO(3 u.c.)-LCO(M u.c.)-BL\*, (c) LSCO(2 u.c.)-LCO(M u.c.)-BL\* and (d) LSCO(1 u.c.)-LCO(M u.c.)-BL\*.

### 5.7.3 Charge glass state in the LSCO(1 u.c.)-LCO(7 u.c.)-BL\*

Figure 5.21 illustrates the field dependent MR curves for the LSCO(1 u.c.)-LCO(7 u.c.)-BL\* that was measured at 2 K, i.e., in the range of hopping conduction. The sample was cooled down at zero field to 2 K. Subsequently, the R-H curves were measured by sweeping the field at a rate of 0.01 T/sec from 0 T to 9 T and back. Irrespective of the applied field ( $H$ ) direction (either along  $ab$ -plane or  $c$ -axis of the sample), the current was always perpendicular to  $H$ . The MR is calculated following the formula  $\frac{R(H)-R(0)}{R(0)}$ , where  $R(0)$  corresponds to the first data point which was measured at zero field.

The irreversible MR data near low field indicate the presence of a ‘charge glass’ state in the system. To understand the observed glassy dynamics of the charge carriers, we recall the ‘charge stripe’ order, where the charge carriers reside at the AF domain boundaries in the  $\text{CuO}_2$  planes. As discussed in subsection 5.6.2, the Dzyaloshinskii-Moriya interaction gives rise to a spin canting in the  $\text{CuO}_2$  planes. This yields a weak ferromagnetic (WF) moment that is uniquely linked to each AF domain. Due to the interlayer coupling between the  $\text{CuO}_2$  planes, the WF moments form a staggered ordering along the  $c$ -axis. Below the spin glass transition temperature, these WF moments freeze [140], and the spin glass state emerges. In this glassy state, the irreversible orientation of the WF moments in response to the applied field causes a realignment of the associated AF domains and the domain boundaries. As the charge carriers

stay at these domain boundaries, they show the observed glassy dynamics. This type of spin glass state is common to lightly doped  $\text{La}_{2-x}\text{Sr}_x\text{CuO}_4$ , where the AF domains are prevalent over the long-range AF order [141].

The sign of the MR is determined by a competition between two inverse mechanisms. These are the coupling of the applied magnetic field to the canted ferromagnetic moment and to the spin of the doped holes, as explicitly discussed in subsection 5.6.2.

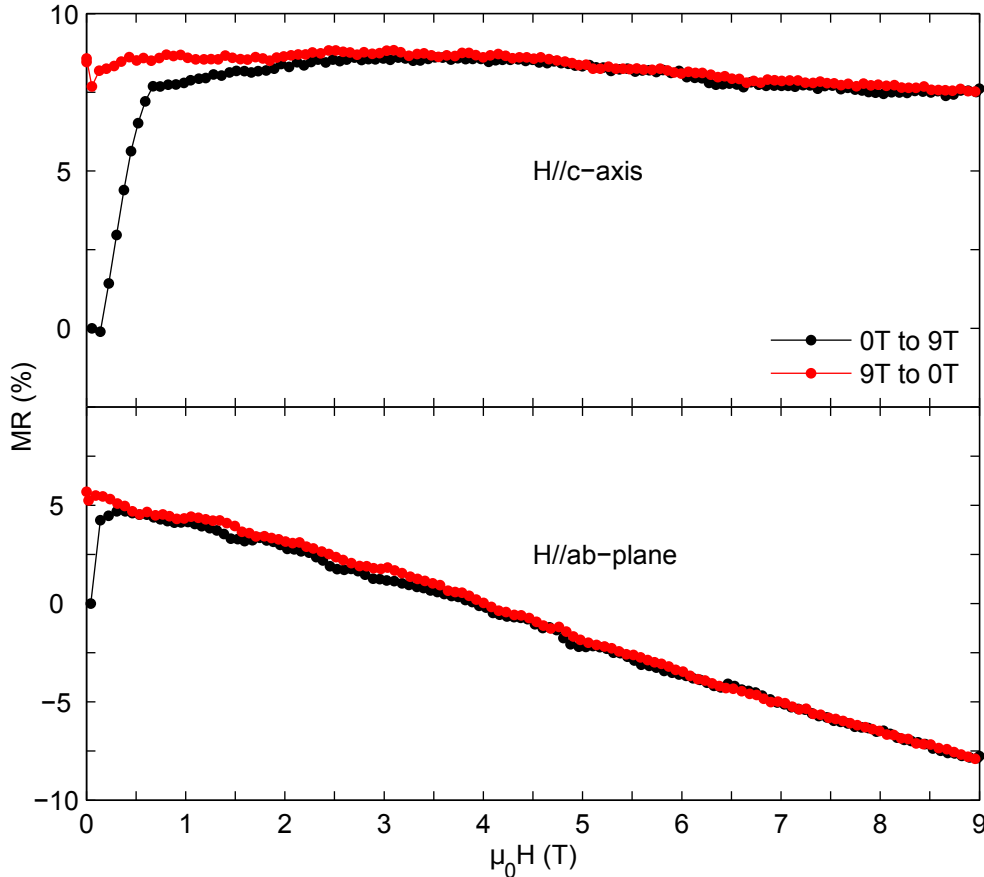


Figure 5.21: Magneto-resistance (MR),  $\frac{R(H)-R(0)}{R(0)}$  of the LSCO(1 u.c.)-LCO(7 u.c.)-BL\* measured after zero field cooling at 2K. Upper and bottom panels are for the two MR curves with the applied field along  $c$ -axis and  $ab$ -plane of the sample, respectively.

#### 5.7.4 Summary

Superconductivity has been realized in a 1 u.c. thick LSCO film by reducing the amount of disorder. A 7 u.c. thick LCO capping layer destroys the SC in the 1 u.c. thick LSCO, and leads to a charge carrier localization at low temperature. It is found that the effect of the thicker LCO layer on the SC of the LSCO layer is limited to the vicinity of the interface. The magneto-transport data for a LSCO(1 u.c.)-LCO(7 u.c.)-BL\* indicate the occurrence of a spin-glass-like state at low temperature.

### 5.8 Concluding remarks

Thin films of  $\text{La}_{2-x}\text{Sr}_x\text{CuO}_4$  and LCMO, and the related heterostructures were grown on (001)-oriented SLAO substrates using the PLD technique. The sharp RHEED intensity oscillations allowed to control the thicknesses of the  $\text{La}_{2-x}\text{Sr}_x\text{CuO}_4$  films on the sub-unit-cell level. The LSCO layer of about 1 u.c. thickness next to the substrate has a significant disorder if it is grown in pure  $\text{N}_2\text{O}$ . The use of a mixture of  $\text{N}_2\text{O}$  and  $\text{O}_2$  gases during the deposition helps to

substantially reduce this kind of disorder. The XRD studies confirmed the epitaxial growth of each component of the investigated heterostructures with the  $c$ -axis along the surface normal. The RSM measurements showed that the LSCO or the LCO layers are almost fully strained while the LCMO layers are partially strain relaxed in the bilayers and the trilayers.

The 7 u.c. thick LSCO film has a reasonably sharp SC transition with  $T_{C,on} \approx 38$  K that is very close to the bulk value of 40 K. The high temperature conductivity of a 7 u.c. thick LCO film is governed by an Arrhenius-like thermal activation, whereas the low temperature conduction follows the 2D VRH model. The low temperature VRH conduction has been explained in terms of the excess oxygen in the film, i.e., the formation of  $\text{La}_2\text{CuO}_{4+\delta}$ . The 20 u.c. thick LCMO has a  $T^{Curie}$  of 190 K and a low temperature magnetization of  $2 \mu_B/\text{Mn-ion}$ .

The LSCO layers with a 2 u.c. thick LCO capping layer show superconductivity down to a 2 u.c. thickness. Note that the LSCO monolayer next to the substrate is strongly disordered. In the LSCO-LCMO-BLs, the FM LCMO suppresses the superconductivity of the LSCO layers. This is most likely due to injected/diffused spin-polarized charge carriers from the LCMO into the LSCO that break the Cooper pairs.

The LSCO(N u.c.)-LCO(2 u.c.)-LCMO(20 u.c.)-TLs were grown to electronically and magnetically decouple the LSCO and the LCMO layers to retain the superconductivity in the LSCO layers. However, the suppression of the superconductivity is stronger in these TLs than in the LSCO-LCMO-BLs. To our surprise, the 2 and 3 u.c. thick LSCO layers in the TLs show a strong charge carrier localization at low temperature. The conduction in this temperature regime is driven by the hopping mechanism.

The origin of the observed charge carrier localization has been studied by varying the thickness of the LCO layer for a series of LSCO(N u.c.)/LCO(M u.c.) bilayers. It is found that a sample with  $N=3$  and  $M=2$  is superconducting, whereas a corresponding BL with  $M=7$  exhibits a charge carrier localization. The magneto-transport data for the LSCO(3 u.c.)-LCO(7 u.c.)-BL confirmed that the holes are localized in an AF background. It was previously reported that a static AF order develops in the LCO films if their thickness exceeds a critical value of 2.5 u.c [34]. Therefore, an interesting possibility of the charge carrier localization is a proximity induced strong AF correlations in the LSCO layer in the presence of the static AF order in the  $M=7$  LCO capping layer. The low temperature hopping conduction and the high temperature metallic transport in the LSCO(3 u.c.)-LCO(7 u.c.)-BL may be understood in terms of a ‘charged stripe’ state.

The thickness of the LCO layer in the LSCO-LCO-LCMO-TLs is only 2 u.c. However, a static AF order may arise in such thin LCO as a result of the strong exchange coupling between Cu and Mn, which is reportedly present at the LCO/LCMO interface [4]. In fact, B. Lake *et al.* reported that an applied magnetic field can induce an AF stripe order in the cuprates [142].

The 1 u.c. thick LSCO layer, grown in the mixture of  $\text{N}_2\text{O}$  and  $\text{O}_2$  gases, is superconducting. We verified that the charge carrier localization phenomena are reproducible in a new set of bilayers (LSCO-LCO-BLs\*) that were grown in such mixed gas environment. The systematic study finds that the proximity effect as mentioned above is bound to the LSCO/LCO interface. The magneto-transport data for the LSCO(1 u.c.)-LCO(7 u.c.)-BL suggest that the holes delocalize in a spin-glass like background.

In addition, we investigated the SC property of the 2 u.c. thick LSCO by reducing the AF order in the capping layer. It is found that the suppression of superconductivity is weak in this case (see Appendix I).

# Chapter 6

## Conclusions and outlook

### 6.1 Conclusions

**The first topic of this thesis** was devoted to the investigation of how the strength of the antiferromagnetic exchange interaction (AEI) between the Cu and the Mn ions at the interfaces of YBCO/LCMO multilayers (MLs) depends on the electronic and magnetic properties of the LCMO layers. For this purpose, three types of MLs (YL\_1-3) were grown on (001)-oriented LSAT substrates with the pulsed laser deposition (PLD) technique. The x-ray diffraction (XRD) and reciprocal space map (RSM) measurements confirmed that the samples are epitaxial and fully strained, respectively. Electron energy loss spectroscopy studies of YL\_2 found the interfacial stacking of  $\text{CuO}_2\text{-BaO-MnO}_2$  at both interfaces. The same type of interface termination was also reported for YL\_1 in Ref. [71].

Rutherford backscattering studies showed that the LCMO layers in YL\_2 are cation deficient, and thus less hole doped than the stoichiometric LCMO. The DC transport measurements and the spectroscopic ellipsometry studies revealed that the LCMO layers in YL\_2 are less conducting than the ones in YL\_1. In addition, the spectroscopic ellipsometry measurements found an evidence for ferromagnetic (FM) polarons in the LCMO layers in YL\_2. The Curie temperatures ( $T^{\text{Curie}}$ ) of the LCMO layers in YL\_1 and YL\_2 are 215 and 180 K, respectively. The saturation values of the average DC magnetization are 2.0 and 2.5  $\mu_B$  per Mn, respectively. On the other hand, the FM order is strongly suppressed for the very thin (5 nm) LCMO layer in YL\_3, where the average magnetization value is 0.25  $\mu_B$  per Mn.

The polarized neutron reflectometry (PNR) study on YL\_2 yielded the thicknesses ( $t^{\text{depl}}$ ) of the so-called ‘depleted layer’ at the YBCO/LCMO and the LCMO/YBCO interfaces, which are 0.83 and 0.66 nm, respectively. The reported values of  $t^{\text{depl}}$  for YL\_1 are 1.32 and 1.10 nm, respectively [3, 29]. The findings suggest that the FM order of the Mn moments at the interfaces of YL\_2 is more robust than in YL\_1.

The x-ray linear dichroism (XLD) studies revealed that the interfacial Cu ions in all three kinds of samples undergo an orbital reconstruction which involves a redistribution of the electrons between the Cu  $3d_{3z^2-r^2}$  and  $3d_{x^2-y^2}$  orbitals. This leads to an almost equal hole occupancies of both orbitals. The x-ray magnetic circular dichroism (XMCD) studies showed that the AEI between the interfacial Cu and Mn ions for YL\_1, YL\_2 and YL\_3 are strong, weak and absent, respectively. Independent of the strength of the AEI, the effective spin magnetic moments per interfacial Cu ions are in the range of 0.11-0.24  $\mu_B$ . This suggests that the Cu moments are not induced by the AEI with Mn, but are intrinsic to the interfacial  $\text{CuO}_2$  planes. It is argued that a weakly FM intra-planar magnetic exchange interaction between the Cu ions may arise due to the nearly equal hole occupation of the Cu  $3d_{3z^2-r^2}$  and  $3d_{x^2-y^2}$  orbitals. Furthermore, it was proposed that the strong suppression of the AEI in YL\_2 may be caused by the FM polaron order in poorly hole doped LCMO layers.

**The second topic of this thesis** was to study superconductivity and charge carrier localization in ultrathin  $\text{La}_{1.85}\text{Sr}_{0.15}\text{CuO}_4$  (LSCO) films. The required thin films of  $\text{La}_{2-x}\text{Sr}_x\text{CuO}_4$  and LCMO, and the related heterostructures were grown on (001)-oriented SLAO substrates

with the PLD technique. The XRD studies confirmed the epitaxial growth of the samples. The RSM measurements revealed that the LCMO layers are partially strain-relaxed. The structural peaks for the LSCO and  $\text{La}_2\text{CuO}_4$  (LCO) layers in the heterostructures could not be separately resolved within the available experimental resolutions in the XRD and RSM measurements.

The LSCO monolayer of 7 u.c. thick has a sharp superconducting (SC) transition with the SC onset temperature ( $T_{C,on}$ ) at 38 K. The  $T^{Curie}$  of the 20 u.c. thick LCMO monolayer is about 190 K, and the low-temperature average magnetization amounts to  $2.0 \mu_B$  per Mn.

The LSCO thin films of 2-5 unit cell (u.c.) thickness with a 2 u.c. thick LCO capping layer have reasonably sharp SC transitions. The values of  $T_{C,on}$  are in the range of 30-38 K. The SC transition temperatures ( $T_{C,on}$  and  $T_C$ ) are reduced in LSCO/LCMO bilayers (BLs), most likely as a result of the injection and/or diffusion of the spin polarized charge carriers from the FM LCMO layers into the LSCO layers across the interface. This effect due to the ferromagnetism of LCMO is apparently limited to the first LSCO monolayer next to the interface. To our surprise, the  $T_C$  is more strongly reduced in LSCO/LCO(2 u.c.)/LCMO(20 u.c.) trilayers (TLs) where the LSCO and LCMO layers are not in direct contact, i.e., they are separated by 2 u.c. of LCO.

Further studies on LSCO/LCO BLs showed that a LSCO(3 u.c.)/LCO(2 u.c.) BL is SC, whereas a LSCO(3 u.c.)/LCO(7 u.c.) BL exhibits a charge carrier localization phenomenon at low temperature. The magneto-transport data in the localization regime seem to indicate that the holes are localized due to the presence of a static AF order. It was reported that the static AF order in single LCO films get stabilized if their thickness exceeds a threshold value of about 2.5 u.c. thick [34]. One interesting possibility is therefore that the observed charge carrier localization in the LSCO/LCO BL arises from an AF proximity effect that emerges in the presence of the static AF order in thicker LCO layer.

The charge carrier localization phenomenon was further reproduced in another set of LSCO/LCO BLs. The systematic studies revealed that this is an interfacial phenomenon. In addition, it was shown that the charge localization is prominent if the AF correlations are strong in the capping layer.

## 6.2 Outlook

The weak AEI between the Cu and Mn ions at the interfaces of YBCO/LCMO MLs is explained in terms of the FM polaron order in the poorly conducting LCMO layers. The occurrence of such FM polarons was evident in the bulk sensitive spectroscopic ellipsometry probe, and it was assumed that such a FM polaron state is also prevalent near the interfaces. Further experiment is therefore necessary to confirm that the FM polaron order exists at the interface region as much as in the core of the LCMO layers. Further experiment should explore Mn XLD on YBCO terminated YBCO/LCMO ML in TEY mode to access the Mn ions at the LCMO/YBCO interface. In the presence of such a FM polaron order, the alternating occupancy of the Mn  $3d_{x^2-y^2}$  and  $3d_{3z^2-r^2}$  orbitals gives rise to a negligible orbital polarization.

It was discussed that the charge carrier localization in the LSCO/LCO BL may arise due to the AF proximity effect in the presence of the static AF order in the LCO layer. However, no experimental results are available to confirm the static AF order in the LCO layer and the occurrence of AF correlations in the LSCO layer next to the interface. In future one could perform the resonant elastic x-ray scattering experiment to confirm the static AF order in the LCO layer. Additionally, the strength of the AF correlations along  $c$ -axis could be found from the experiment. This in return can validate the hypothesis of the proximity induced AF correlations in the LSCO layer. A massive transfer of holes from the LSCO layer into the LCO layer was discussed as another underlying mechanism behind the observed charge localization. The doped holes reside at the oxygen sites in the  $\text{CuO}_2$  planes and form the so-called Zhang-Rice singlets. This leads to the mobile carrier peak (MCP) near the O K-edge.

The resonant x-ray reflectometry at this MCP can determine the charge distribution in the LSCO/LCO bilayers.

We have shown that the strength of the AF coupling between the Mn moments and the induced Cu moments can be strongly reduced such that their relative orientation can be changed from antiparallel to parallel with the external magnetic field. This is a promising step toward the engineering of SC/FM interfaces where the control of the interfacial magnetic structure is a prerequisite. For an example, a high temperature spin-triplet state requires a specific kind of non-collinear magnetic structure in the vicinity of the SC/FM interface. The findings can also be applied in FM/SC/FM type of transistors where the applied magnetic field can give rise to the desired current vs. voltage characteristics that are immensely valuable in future oxide electronics.

We have documented that the 1 u.c. thick SC LSCO films can be grown with the PLD technique. This proves the versatility of the technique, and thus can be applied to deposit ultrathin films of other complex materials. The presence of high temperature superconductivity in a LSCO monolayer (1.3 nm) can be useful in SC quantum computing devices where an ultrathin SC layer is required. Also, this ultrathin SC layer serves as an ideal system to understand the high- $T_C$  cuprate systems better. For instance, we have investigated the effect of strong AF correlations in the system.

# Appendix A

## Analysis of the x-ray absorption curves

### A.1 Background subtraction and normalization of the x-ray absorption spectra

The as measured x-ray absorption spectra (XAS) at the resonance of a particular element contain a background that originates from the post-edge absorption of other elements. To obtain the XMCD and XLD signals, and to perform a meaningful sum rule analysis it is necessary to subtract this background from the XAS curves in a consistent way. As an example, we discuss in the following the subtraction procedure for a set of left and right circularly polarized XAS curves in TEY mode at the Cu and Mn  $L_{3,2}$ -edges. The same procedure has been applied to the XMCD and XLD data in TFY mode.

Figure A.1a shows a series of XAS curves for YL.2 in TEY mode at the Cu  $L_{3,2}$ -edge with left and right circularly polarized light, measured at 2 K and 0.5 T. In a first step, they have been normalized at the pre-edges to correct the finite intensity drift which most likely arises from a weak ‘charging effect’ of the sample. For each helicity we performed multiple measurements to enhance the signal to noise ratio and to confirm the reproducibility. In a next step, we corrected the background of these normalized XAS curves. Assuming a linear background, we fitted the pre-edge of the averaged XAS curves for both helicities with a straight line, as shown in Figure A.1b. This linear background was then subtracted from the XAS curves to obtain the curves that are displayed in Figure A.1c. Finally, we normalized the XAS curves at the ‘edge sum’ region as shown in Figure A.1d. The Mn XAS data were corrected and normalized in a corresponding way, as shown in Figure A.2.

### A.2 Multi-peak fitting to the XAS curves at the $L_3$ -edges

Here, we describe the method of the multi-peak fitting at the  $L_3$ -edge of the Cu XAS curves in TEY and TFY mode. We have followed the same approach as detailed in Refs. [4, 69]. For the Cu atoms, we consider four transitions. These are (a) and (b) the  $2p^63d^9 \rightarrow 2p^53d^{10}$  transitions of the interfacial and the bulk  $\text{Cu}^{2+}$  ions, respectively, and (c) and (d) the  $2p^63d^9\bar{L} \rightarrow 2p^53d^{10}\bar{L}$  transitions related to the Zhang-Rice singlets of bulk Cu ions in the  $\text{CuO}_2$  planes and CuO chains, respectively. Accordingly, we used four Lorentzian functions for the fitting of the XAS near the  $L_3$ -edges (equation (A.1)). To account for the edge jumps and the remaining background under the XAS curves, we added a combination of linear and sigmodal functions (equation (A.2)). To find the peak positions, all TFY and TEY XAS curves of a given sample have been fitted simultaneously with the peak positions as common parameters. In a next step, the peak positions have been fixed and each pair of XAS curves ( $\mu_+$  and  $\mu_-$ ;  $\mu_{ab}$  and  $\mu_c$ ) are fitted simultaneously for TFY/TEY mode by considering the parameters for background and widths of the Lorentzian profiles as common parameters. The fitting gives the weight

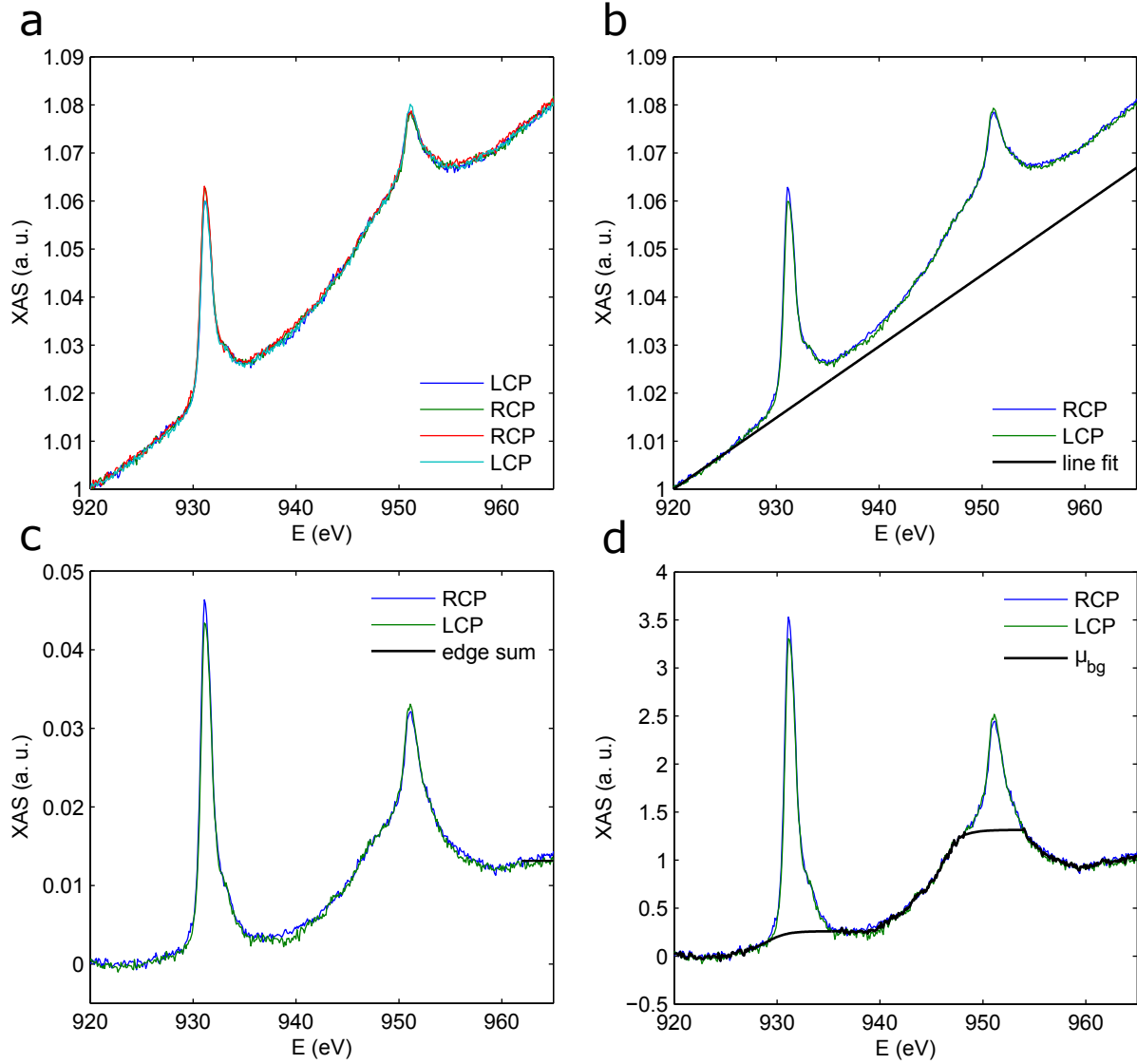


Figure A.1: (a) Normalization with respect to the pre-edge of the Cu XAS curves for left and right circularly polarized light (LCP and RCP) at 2K and in 0.5T. (b) Normalized and averaged XAS curves for the two helicities, and a linear fit of the background signal in the pre-edge region. (c) XAS curves after subtracting the linear background. (d) XAS curves after the normalization with respect to the post-edge showing the estimate of  $\mu_{bg}$  which accounts for the non-linear background and the edge jumps.

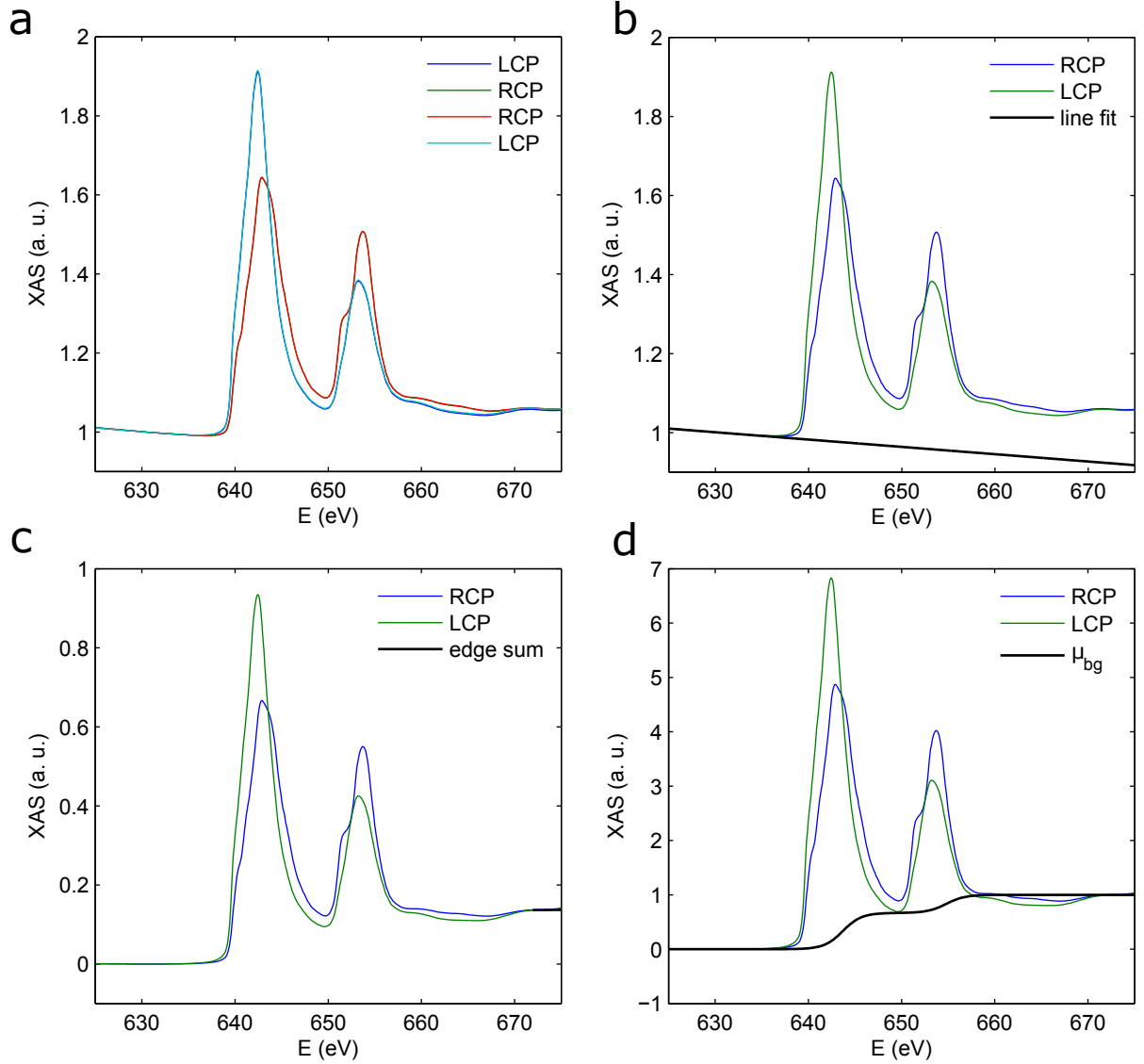


Figure A.2: (a) Normalization with respect to the pre-edge of the Mn XAS curves for left and right circularly polarized light at 2K and at 0.5T. (b) Normalized and averaged XAS curves for the two helicities, and a linear fit of the background signal in the pre-edge region. (c) XAS curves after subtracting the linear background. (d) XAS curves after the normalization with respect to the post-edge showing the estimate of  $\mu_{bg}$  which is representative of the edge jumps.

of each transition for each absorption spectrum. The relative weight ( $w_i$ ) of each Lorentzian peak has been calculated by following the equation (A.3). The  $w_i$  correspond to the fraction of Cu ions that contribute to the particular ( $i$ ) transition.

$$y_L(E) = \sum_{i=1}^4 \frac{2A_i}{\pi} \frac{w_i}{4(E - x_{c,i})^2 + w_i^2} \quad (\text{A.1})$$

$$y_{bg}(E) = y_0 + y_1 E + \frac{B}{1 + \exp(-k(E - x_0))} \quad (\text{A.2})$$

$$w_i = \frac{2\mu_{ab,i} + \mu_{c,i}}{\sum_{j=1}^4 (2\mu_{ab,j} + \mu_{c,j})} = \frac{N_i}{\sum_{j=1}^4 N_j} \quad (\text{A.3})$$

### A.3 Deriving the orbital and effective spin magnetic moment from XMCD in TEY mode

The magnetic moment of the Cu and Mn ions has been obtained from the XMCD data using conventional sum rules [69, 92–94]. We restricted this analysis to the TEY mode, since in TFY mode, the Cu XMCD signal is very small and the Mn XAS curves are strongly distorted due to ‘self-absorption effect’. The spin moments of Cu and Mn have been obtained using the following equations.

$$\langle L_j \rangle = -\frac{2}{3} \frac{\int_{L_3+L_2} (\mu_+ - \mu_-) d\omega}{\int_{L_3+L_2} (\frac{\mu_+ + \mu_-}{2} - \mu_{bg}) d\omega} n_{3d} \quad (\text{A.4})$$

$$\langle S_j \rangle + \frac{7}{2} \langle T_j \rangle = -\frac{1}{2} \frac{\int_{L_3} (\mu_+ - \mu_-) d\omega - 2 \int_{L_2} (\mu_+ - \mu_-) d\omega}{\int_{L_3+L_2} (\frac{\mu_+ + \mu_-}{2} - \mu_{bg}) d\omega} n_{3d} \quad (\text{A.5})$$

where,  $\langle L_j \rangle$ ,  $\langle S_j \rangle$  and  $\langle T_j \rangle$  are the expectation values of the orbital, spin and magnetic dipole operator along the beam direction ( $j$ ), respectively. The parameters  $\mu_+$  and  $\mu_-$  represent the x-ray absorption with the photon angular momentum parallel and antiparallel to the applied magnetic field.  $\mu_{bg}$  is the correction of the edge-jumps and remaining background of the absorption curves. For the Mn XAS curves, the linear background has been corrected with the procedure described above. In addition, the contribution of the edge jumps has been subtracted using a step-like sigmoidal function with relative amplitudes of 2/3 and 1/3 at the  $L_3$  and  $L_2$  edges, respectively, as shown in Figure A.2d. For the Cu XAS spectra the choice of  $\mu_{bg}$  is complicated by the presence of a nonlinear background that arises because the magnitude of the resonant part of the Cu XAS signal is very small (due to the limited escape depth of the photo-electrons and the fact that they have to pass through the topmost LCMO layer) and it gets further affected by the strong post-edge features of the La  $M_{4,5}$  absorption. As shown in Figure A.1d, we found that the best choice of  $\mu_{bg}$  is a combination of the background of the average of the XAS curves for RCP and LCP x-rays, and a sigmoidal function that accounts for the edge-jumps.  $n_{3d}$  is the number of holes in the 3d-orbitals, whose values are taken as 6.33 and 1 for the Mn and Cu ions, respectively. Finally, the orbital and effective spin magnetic moments ( $m_l$  and  $m_{s,eff}$ ) have been obtained using the following relationships:

$$m_l = -\langle L_j \rangle \mu_B \quad (\text{A.6})$$

$$m_{s,eff} = -2(\langle S_j \rangle + \frac{7}{2} \langle T_j \rangle) \mu_B \quad (\text{A.7})$$

The factor ‘-1’ in equation (A.6) and ‘-2’ in equation (A.7) corresponds to the Landé g-factor of an electron for its orbital and spin momentum, respectively. The derived values of the orbital and effective spin magnetic moments for the Cu and Mn ions are listed in Tables A.1 and A.2, respectively.

	YL_1		YL_2		YL_3	
	0.5 T	5 T	0.5 T	6 T	0.5 T	5 T
$m_l$ ( $\mu_B/\text{Cu}$ )	-0.012(2)	-0.014(4)	-0.014(4)	0.008(2)	0.005(1)	0.025(5)
$m_{s,eff}$ ( $\mu_B/\text{Cu}$ )	-0.07(1)	-0.06(2)	-0.05(2)	0.06(2)	0.03(1)	0.14(3)

Table A.1: Orbital and effective spin moments for Cu ions as derived from the XMCD signal in TEY mode by using the sum rules in equations (A.6) and (A.7). The error bar represents the uncertainty related to the background subtraction.

	YL_1		YL_2		YL_3	
	0.5 T	5 T	0.5 T	6 T	0.5 T	5 T
$m_l$ ( $\mu_B/\text{Mn}$ )	-0.065(6)	-0.064(6)	-0.023(2)	-0.007(1)	-0.052(5)	-0.104(10)
$m_{s,eff}$ ( $\mu_B/\text{Mn}$ )	1.79(18)	2.00(20)	2.28(23)	2.56(26)	0.27(3)	0.75(8)

Table A.2: Orbital and effective spin moments for Mn ions as derived from the XMCD signal in TEY mode by using the sum rules in equations (A.6) and (A.7). The error bar represents the uncertainty related to the background subtraction.

## A.4 Electron polarization of the Mn $e_g$ -orbitals

The orbital polarization,  $P_{e_g}$  of the LCMO layers in YL-1-3 has been deduced following the procedure of Refs. [67, 69].

$$P_{e_g} = \frac{n_{3z^2-r^2} - n_{x^2-y^2}}{n_{3z^2-r^2} + n_{x^2-y^2}} = \frac{19}{2} \frac{\int_{L_3+L_2} 2(\mu_{ab} - \mu_c) d\omega}{\int_{L_3+L_2} (2\mu_{ab} + \mu_c - 3\mu_{bg}) d\omega} \quad (\text{A.8})$$

Here,  $n_{3z^2-r^2}$  and  $n_{x^2-y^2}$  are the number of electrons in the  $d_{3z^2-r^2}$  and  $d_{x^2-y^2}$  orbitals, respectively.  $\mu_{ab}$  and  $\mu_c$  represents the absorption for linear polarization along  $ab$ -plane and  $c$ -axis of a sample, respectively.  $\mu_{bg}$  accounts for the baseline correction about which we discussed earlier. As an example, Figure A.3 shows a set of XAS curves with the baseline for the case of YL\_2. The obtained values for the electron orbital polarization of the Mn

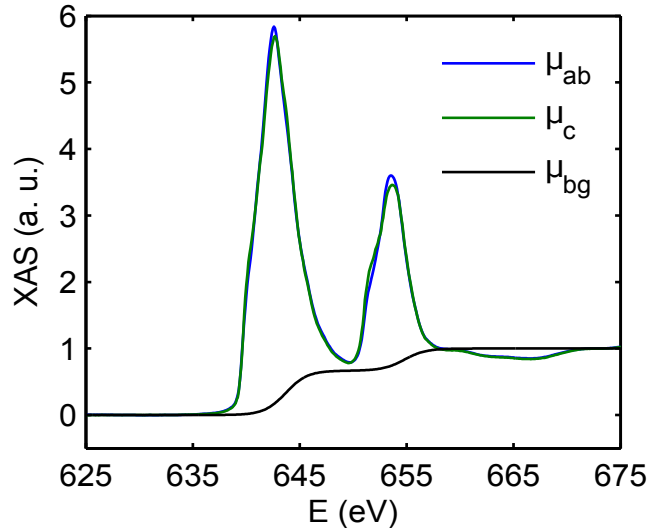


Figure A.3: (a) Mn XLD curves of YL\_2 in TEY mode showing  $\mu_{ab}$  and  $\mu_c$  and base line,  $\mu_{bg}$  which accounts for edge jumps.

ions of YL\_1, YL\_2 and YL\_3 are +14.3(14)%, +2.7(3)% and +15.4(15)%, respectively. The positive sign of  $P_{e_g}$  shows that the  $3d_{x^2-y^2}$  has a higher hole concentration, i.e., the electrons preferably occupy the  $3d_{3z^2-r^2}$  orbital.

## Appendix B

# Electron polarization of $e_g$ -orbitals in a FM polaron

In the following, it is shown that the ferromagnetic (FM) polarons do not give rise to x-ray linear dichroism signal (XLD), i.e., the electron polarization of their  $e_g$ -orbitals amounts to zero.

As shown in Figure 4.8a, a FM polaron consists of two  $3d_{3z^2-r^2}$ , two  $3d_{3x^2-r^2}$  and two  $3d_{3y^2-r^2}$  orbitals. Among them, the last two orbitals are in-plane orbitals. In the following, they are represented in the basis of  $|x^2 - y^2\rangle$  and  $|3z^2 - r^2\rangle$ .

$$\begin{aligned} 3d_{x^2-y^2} &: |x^2 - y^2\rangle \\ 3d_{3z^2-r^2} &: |3z^2 - r^2\rangle \\ 3d_{3x^2-r^2} &: \frac{3}{2\sqrt{3}} |x^2 - y^2\rangle - \frac{1}{2} |3z^2 - r^2\rangle \\ 3d_{3y^2-r^2} &: -\frac{3}{2\sqrt{3}} |x^2 - y^2\rangle - \frac{1}{2} |3z^2 - r^2\rangle \end{aligned}$$

Calculation of the expectation value of the  $|x^2 - y^2\rangle$  and  $|3z^2 - r^2\rangle$  thus yields:

$$\begin{aligned} \text{Number of } 3d_{x^2-y^2} \text{ orbitals} &= 2 \times 0 + 2 \times \frac{9}{12} + 2 \times \frac{9}{12} = 3. \\ \text{Number of } 3d_{3z^2-r^2} \text{ orbitals} &= 2 \times 1 + 2 \times \frac{1}{4} + 2 \times \frac{1}{4} = 3. \end{aligned}$$

The  $3d_{x^2-r^2}$  and  $3d_{3z^2-r^2}$  orbitals thus have the same occupation probability which means that the XLD and the electron polarization of the  $e_g$ -orbitals amount to zero.

## Appendix C

# Origin of the Cu moment at the interfacial $\text{CuO}_2$ planes

In subsection 4.8.2, it was shown for interfacial Cu ions that the  $3d_{3z^2-r^2}$  and  $3d_{x^2-y^2}$  orbitals have similar amount of holes. This is known as ‘orbital reconstruction’. Considering the fact, Prof. Dr. D. Munzar and his student Mr. J. Vašátko performed exact diagonalization calculations for a cluster that contains four Cu sites with one hole per site. Details of the calculation can be found in Ref. [143]. The outcome of the calculation is that the orbital reconstruction may lead to a weak ferromagnetic (FM) exchange coupling between the Cu moments in the interfacial  $\text{CuO}_2$  planes. In the following, we qualitatively discuss this finding assuming the average hole occupancy of the two  $e_g$ -orbitals is the same.

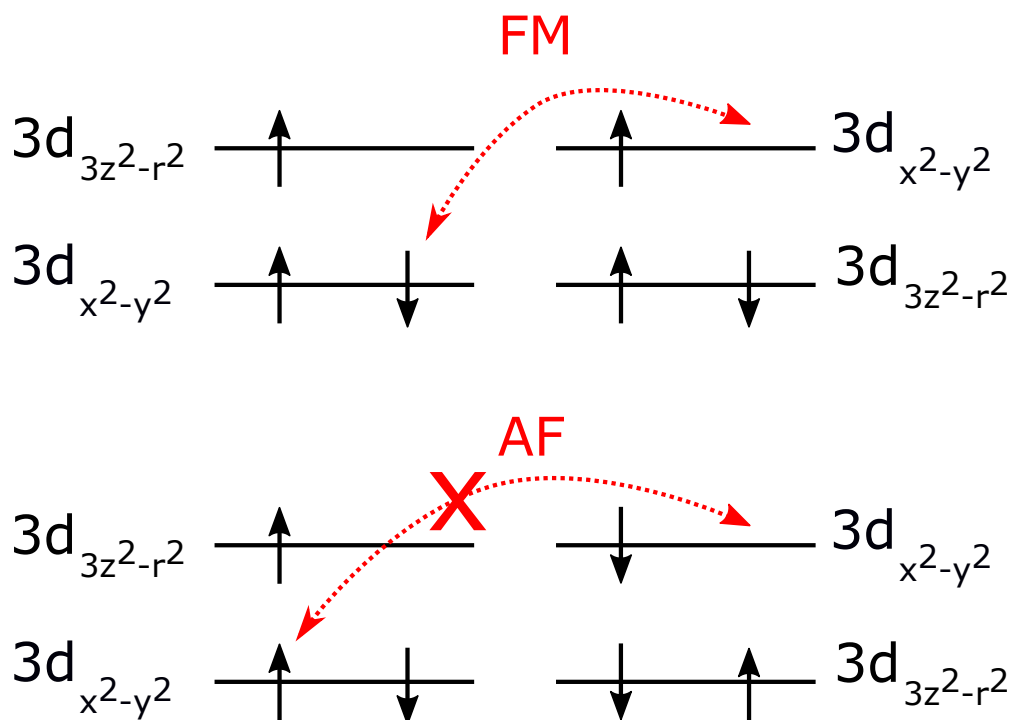


Figure C.1: Virtual hopping between two neighboring Cu ions for which the hole occupancy of two  $e_g$ -orbitals is equal, but  $t_{x^2-y^2} \gg t_{3z^2-r^2}$ . Upper and bottom panels show the ferromagnetic (FM) and antiferromagnetic (AF) coupling schemes, respectively. The FM coupling scheme appears to be energetically favorable.

Figure C.1 shows a level scheme for the intermediate energy levels of the two  $e_g$ -orbitals for which the hole occupancy of the two  $e_g$ -orbitals is equally probable. Virtual hopping of electrons is restricted to the  $3d_{x^2-y^2}$  orbitals as their hybridization through oxygen is much stronger than the one of the  $3d_{3z^2-r^2}$  orbitals. The upper panel shows the case of a FM

coupling with parallel spins in the partially occupied levels of neighbouring Cu ions. Here, the down spin electron can hop between the  $3d_{x^2-y^2}$  orbitals without violating the local Hund's coupling which requires that the spins of partially occupied  $3d_{x^2-y^2}$  and  $3d_{3z^2-r^2}$  levels are parallel. On the other hand, the lower panel shows that this local Hund's coupling is violated for the case of an antiferromagnetic (AF) coupling with antiparallel spins in the partially occupied levels of the neighbouring Cu ions. In this case, the hopping of the spin up electron between the Cu  $3d_{x^2-y^2}$  orbitals, leads to a violation of the local Hund's coupling for the left hand Cu ion. For this reason, the AF scheme becomes energetically less favorable than to the FM case. As a consequence, the in-plane ferromagnetic order prevails at the interfacial  $\text{CuO}_2$  plane where the Cu ions undergo an orbital reconstruction.

## Appendix D

# Variable range hopping model

In disordered media, when charge carriers localize, the charge conduction between the localized states often follows the variable-range hopping (VRH) model [144, 145] as described by the following equations.

$$R = R_0 \exp\left(\frac{T_0}{T}\right)^{\frac{1}{d+1}} \quad (\text{D.1})$$

or,

$$\ln R = \ln R_0 + \left(\frac{T_0}{T}\right)^{\frac{1}{d+1}} \quad (\text{D.2})$$

where  $R$  is the temperature dependent resistance,  $R_0$  is a constant,  $T_0$  is a characteristic temperature and  $d$  is the dimension of the density of states. The localization length ( $\xi$ ) is inversely proportional to  $T_0$ . In this conduction regime, the charge carriers hop from a localized state to another to minimize their kinetic energy. The hopping probability depends on the energy separation, as well as the spatial separation of the localized states.

In the present case of the lightly doped cuprate or the hole motion in an antiferromagnetic (AF) background, the low temperature R-T characteristics of the thin films and the heterostructures are well described with the 2 dimensional ( $d = 2$ ) VRH model.

## Appendix E

# MATLAB code to measure V-I characteristics with Keithley

With the help of MATLAB instrument control toolbox, we established communication between the computer and a Keithley SourceMeter via a serial port. The following MATLAB code was used to measure V-I characteristic. This code is compatible with the Keithley KE26xx series.

```
%% Create serial instrument
s=serial('COM8','BaudRate',9600); % Construction of a serial port
fopen(s); % Connect to the serial port
% fprintf(s,'*IDN?'); % To query the device

%% Instrument KE26XX compatible language
fprintf(s,'smub.reset()'); %Restore 2602 defaults
fprintf(s,'display.screen = 1'); % Select channel B display
fprintf(s,'display.smub.measure.func = display.MEASURE.DCVOLTS'); % Display current
% fprintf(s,'smub.source.level1 = 10e-3'); % Set the current limit to 10 mA
% fprintf(s,'smub.measure.autorange1 = smub.AUTORANGE.ON'); % Select measure I auto range
fprintf(s,'smub.source.output = smub.OUTPUT.ON'); % Turn on output
vv=0e-3:-0.1e-3:-6e-3; % Enter your current range range in Amps (start:step:end)
for i=1:length(vv)
    v_command=sprintf('smub.source.level1 = %15.15f',vv(i)); % Generate command
    fprintf(s,v_command);
    fprintf(s,'triggered = trigger.wait(0.1)'); % Time taken for a data point
    fprintf(s,'print(smub.measure.v())'); % print measured data
    temp{i}=fscanf(s,'%f'); % Get the reading to the workspace
    % fprintf(s,'smub.source.levelv = 0'); % Set the output to zero after
    % each data point
    % fprintf(s,'triggered = trigger.wait(0.5)'); % Waiting time at zero
end
ii=cell2mat(temp);
fprintf(s,'smub.source.output = smub.OUTPUT.OFF'); % Turn off output
%% Save data
VI=[vv ii];
fid=fopen('BL-1955-ch3-VvsI-T2K.dat','w'); % Give the name of the file
for i=1:length(ii)
    fprintf(fid,'\n%15.15f %15.15f\r',vv(i),ii(i));
end
fclose(fid);
%% Plot data
plot(vv,ii,'--rs','LineWidth',1,'MarkerEdgeColor','k','MarkerFaceColor','g','MarkerSize',5);
xlabel('I [amp]','fontsize',12);
ylabel('V [Volt]','fontsize',12);
saveas(gca,'BLs-1955-ch3-VvsI-T2K.pdf','pdf'); % Save the plot as pdf
%% Delete serial instrument
fclose(s);
delete(s);
```

## Appendix F

# The R-T curves of a LCO(2 u.c.)-LCMO(20 u.c.)-BL

Figure F.1 shows the R-T characteristic of a LCO(2 u.c.)-LCMO(20 u.c.)-BL. As the sample is very insulating, we were not able to measure its resistance below 125 K. The R-T curve can be well described with an Arrhenius-like thermal activation model, suggesting a typical semiconducting behavior.

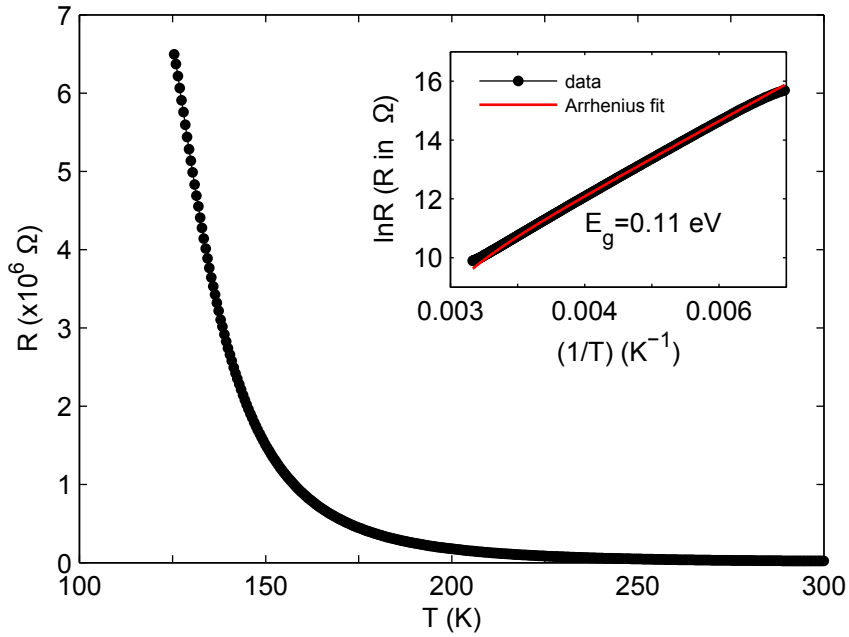


Figure F.1: Temperature dependent resistance of a LCO(2 u.c.)-LCMO(20 u.c.)-BL. Inset shows the fitting of the raw data with the Arrhenius model of activation:  $\ln R = \ln R_0 + (\frac{E_g}{k_B T})$ .

## Appendix G

# Hopping conduction in the LSCO(3 u.c.)-LCO(7 u.c.)-BL

Figure G.1a shows the fitting of the R-T curve of the LSCO(3 u.c.)-LCO(7 u.c.)-BL with the 2D VRH model, suggesting a charge carrier localization at low temperature. Two distinct  $T_0$  indicate a subtle change in the hopping mechanism below around 12 K. Around the similar temperature, the positive MR steeply increases (see Figure G.1b), demonstrating a realignment of the spin background in which the charge carriers move. Only from the R-T measurement, it is difficult to determine what sort of spin alignment increases the localization length at  $T \rightarrow 0$ .

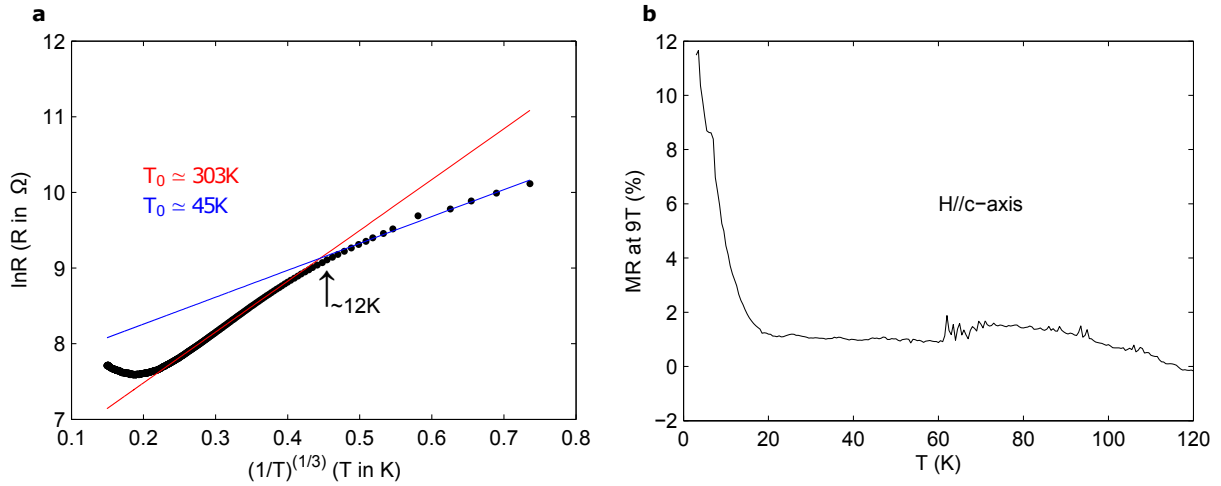


Figure G.1: (a) 2D VRH fitting of the R-T curve of the LSCO(3 u.c.)-LCO(7 u.c.)-BL at 0 T. Different values of  $T_0$  are necessary to fit the different ranges of the low temperature R-T curve. The crossover occurs around 12 K. (b) Temperature dependent MR at 9 T. This is calculated from the R-T characteristics that were measured at 0 and 9 T fields with the field direction along  $c$ -axis.

## Appendix H

# Hopping conduction in the LCO(1 u.c.)-LCO(7 u.c.)-BL\*

Figure H.1 shows the R-T curve of the LSCO(1 u.c.)-LCO(7 u.c.)-BL\*. The low temperature data, below around 40 K, can be described well with the 2D VRH model, suggesting a charge carrier localization at low temperature. In this regime, the charge carriers hop from one localized state to another to minimize their kinetic energy.

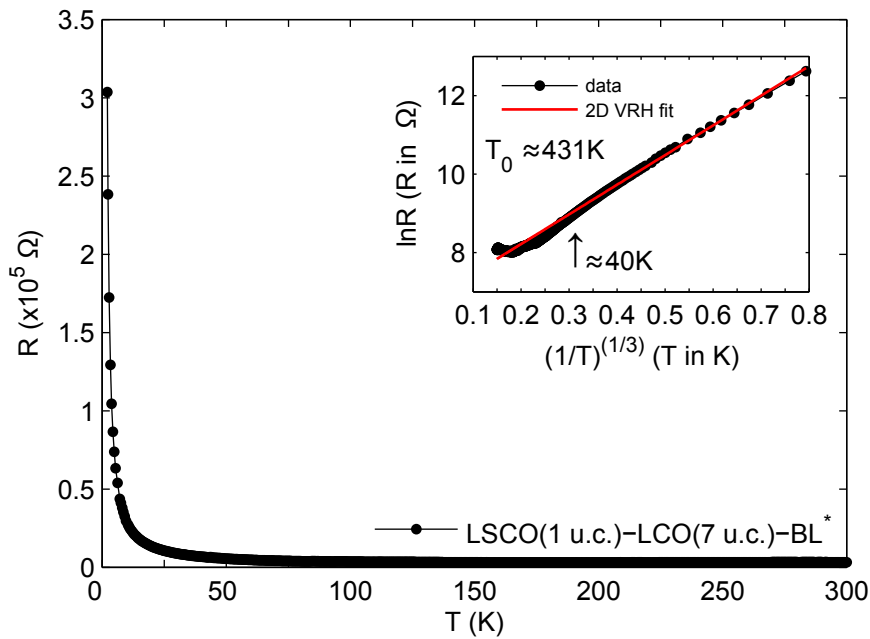


Figure H.1: Temperature dependent resistance of LSCO(1 u.c.)-LCO(7 u.c.)-BL\*. Inset shows the best fit to the raw data at the low temperature with the 2D VRH model:  $\ln R = \ln R_0 + \left(\frac{T_0}{T}\right)^{\frac{1}{3}}$ .

# Appendix I

## 7 u.c. thick $\text{La}_{1.94}\text{Sr}_{0.06}\text{CuO}_4$ capping on 2 u.c. thick LSCO

The 7 u.c. thick  $\text{La}_{1.94}\text{Sr}_{0.06}\text{CuO}_4$  (LSCO\_06) capping layer weakly suppresses the superconductivity of the 2 u.c. LSCO, as shown in Figure I.1. In contrast, the 7 u.c. thick LCO capping layer destroys the macroscopic superconductivity in the corresponding bilayer. This could be the consequence of the weak AF correlations in the LSCO\_06 layer [42]. Strikingly, the high temperature R-T characteristics are very similar. This indicates the common mechanism involves with the charge conduction at high temperature where the AF correlations are expected to be weak. This common mechanism may arise from the formation of a so-called ‘charge stripe’ order.

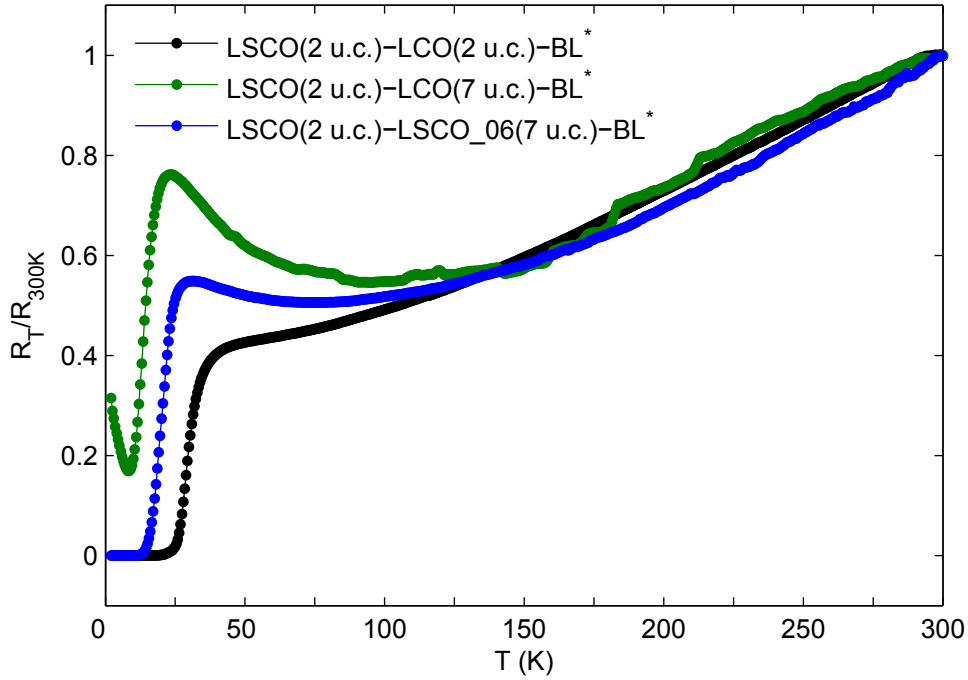


Figure I.1: Temperature dependent resistances of LSCO(2 u.c.)-LCO(2 u.c.)-BL\*, LSCO(2 u.c.)-LCO(7 u.c.)-BL\* and LSCO(2 u.c.)-LSCO\_06(7 u.c.)-BL\*.

# Acknowledgement

It has been four years and two months since I started my PhD. I have been very lucky during these years for being surrounded by good and intelligent people who directly and indirectly shaped me and my thesis. I am deeply indebted to all these people, and in the following, I would like to thank them.

First and foremost, I wish to express my gratitude to my supervisor Prof. Christian Bernhard for several reasons. Firstly, his relentless engagement towards my research always helped me to be on the right track, and to broaden my scientific wisdom. Secondly, his careful comments on various occasions were extremely helpful to develop my scientific writing and communication skills. If I have improved my writing skill, then the credit goes to him. Finally, his scientific passion and working style always enchanted me. I will consider myself very lucky if I can reflect some of his qualities in my research and professional careers.

When I first entered into the PLD laboratory, I was clueless after seeing multiple pumps, gas bottles, and complex arrangement of electrical wires and gas tubes. But, the careful guidance of my former colleagues Dr. Saikat Das and Dr. Ivan Marozau helped me to soon become a confident PLD user. Moreover, a significant part of my thesis is an extension of the PhD work of Dr. Das. His tremendous hard work made my research work quite easy to reach the successful end. After he left our group, whenever necessary, he was there just a Viber call away. I am also indebted to him for giving me inspiration and suggestions in my bad times. I absolutely had no idea about the large-scale research facilities such as neutron reflectometry and x-ray absorption spectroscopy. Dr. Miguel Angel Uribe-Laverde taught me every detail of these techniques and the corresponding data analysis. From him, I have learnt an attitude to look for an appropriate theoretical model to fit an experimental data in order to extract maximum possible information. Furthermore, the beamtimes would not become fun without the wonderful company of Dr. Uribe-Laverde and Dr. Das.

Once I needed to submit an abstract for the M<sup>2</sup>S conference in Geneva at the deadline. A careful guidance of Dr. Edith Perret in writing the abstract helped me to win an invited talk in the prestigious conference on superconductivity. When I was busy in writing thesis, Dr. Perret and Dr. Aurora Alberca were generous to measure my samples.

Numerous theories on high- $T_C$  superconductors always puzzle me. Whenever I needed a discussion on superconductivity, Dr. Benjamin Mallett was there to help me out of my confusion. I am very grateful for his time and patience to listen me. Also, he helped to shape my cover letter for the application for postdoc position. I am obliged for that as well. We had many moments when we discussed about the philosophical meaning of life, and I enjoyed his enthusiasm in finding the meaning.

I also appreciate the company of my other colleagues Dr. Andrea Cerreta, Dr. Premysl Marsik, Meghdad Yazdi-Rizi, Jarji Khmaladze, Roberto de Andres Prada, Evgeniia Sheveleva, Fryderyk Lyzwa. Specially, I would like to thank Meghdad for all the chats which were very relaxing at the hectic times of writing thesis.

For the assistance in carrying out the neutron reflectometry and the x-ray absorption spectroscopy experiments, I would like to thank Dr. Yuri Khaydukov and Dr. Olaf Soltwedel from the Max-Planck Institute for Solid State Research, Dr. Jochen Stahn and Dr. Cinthia Piamonteze from the Paul Scherrer Institute. I would also like to thank Prof. Dominik Munzar and Jiri Vařátko from the Masaryk University, Dr. Max Döbeli from the ETH Zürich, Dr. Neven Biškup and Prof. Maria Varela from the Universidad Complutense de Madrid for the

successful collaboration.

I am thankful to the secretaries Eliane Esseiva, Nadia Pury and Bernadette Kuhn-Piccand for the administrative support. I am sincerely obliged to Oswald Raezo, Jean-Luis Andrey and Francis Bourqui for the technical helps.

I would like to thank my flatmate Mr. Thierry Bertsch for his friendship and his constant effort to keep the flat nice and tidy. I am grateful for his phone calls whenever I got stuck in the laboratory at night. At the end, I got a flat which was a home away from my home.

I am deeply indebted to my parents and beloved brother for their support through out my stay in abroad. Specially, I would like to thank my brother to take care of my parents and all the family matters when I was busy with my PhD.

In the times of turmoil, as happened in the life of most PhD students, my fiancé Shraddha kept encouraging me to fight back all the odds, and gave me a cozy shelter whenever she saw me restless. I am grateful for all her support, understanding, patience, and love.

# Curriculum Vitae

## Personal Details

Name: Sen  
First name: Kaushik  
Date of birth: May 6, 1989  
Place of birth: Rajbalhat, India  
Nationality: Indian

## Education

2012-2016: PhD in Physics  
Department of Physics  
University of Fribourg  
Fribourg, Switzerland

2009-2011: MSc in Physics  
Department of Physics  
Indian Institute of Technology Bombay  
Powai, India

2006-2009: BSc in Physics  
University of Calcutta  
West Bengal, India

## Languages

Bengali: Native  
English: Advanced

## Publications as First Author

*Superconductivity and charge localization in ultrathin  $La_{1.85}Sr_{0.15}CuO_4$*

K. Sen *et al.*

To be submitted to Phys. Rev. B.

*X-ray absorption study of the ferromagnetic Cu moment at the  $YBa_2Cu_3O_7/La_{2/3}Ca_{1/3}MnO_3$  interface and the variation of its exchange interaction with the Mn moment*

K. Sen, E. Perret, A. Alberca, M. A. Uribe-Laverde, I. Marozau, M. Yazdi-Rizi, B.P.P. Mallett, P. Marsik, C. Piamonteze, Y. Khaydukov, M. Döbeli, T. Keller, N. Biškup, M. Varela, J. Vašátko, D. Munzar and C. Bernhard  
Phys. Rev. B **93**, 205131 (2016).

## Publications as Contributing Author

*Terahertz ellipsometry study of the soft mode behavior in ultrathin  $SrTiO_3$  films.*

P. Marsik, K. Sen, J. Khmaladze, M. Yazdi-Rizi, B.P.P. Mallett and C. Bernhard  
Appl. Phys. Lett. **108**, 052901 (2016).

*X-ray absorption spectroscopy study of the electronic and magnetic proximity effects in  $YBa_2Cu_3O_7/La_{2/3}Ca_{1/3}MnO_3$  and  $La_{2-x}Sr_xCuO_4/La_{2/3}Ca_{1/3}MnO_3$  multilayers.*

M.A. Uribe-Laverde, S. Das, K. Sen, I. Marozau, E. Peret, A. Alberca, J. Heidler, C. Piamonteze, M. Merz, P. Nagel, S. Schuppler, D. Munzar and C. Bernhard  
Phys. Rev. B **90**, 205135 (2014).

*Structural, magnetic and superconducting properties of pulsed-laser-deposition-grown  $La_{2-x}Sr_xCuO_4/La_{2/3}Ca_{1/3}MnO_3$  superlattices on (001)-oriented  $SrLaAlO_4$  substrates*

S. Das, K. Sen, I. Marozau, M. A. Uribe-Laverde, N. Biskup, M. Varela, Y. Khaydukov, O. Soltwedel, T. Keller, M. D'obeli, C. W. Schneider, and C. Bernhard  
Phys. Rev. B **89**, 094511 (2014).

*Depth Profile of the Ferromagnetic Order in a  $YBa_2Cu_3O_7/La_{2/3}Ca_{1/3}MnO_3$  Superlattice on a LSAT Substrate: A Polarized Neutron Reflectometry Study*

M. A. Uribe-Laverde, D. K. Satapathy, I. Marozau, V. K. Malik, S. Das, K. Sen, J. Stahn, A. Ruhm, J. H. Kim, T. Keller, A. Devishvili, B. P. Toperverg, and C. Bernhard  
Phys. Rev. B **87**, 115105 (2013).

# Bibliography

- [1] J. Chakhalian, J. W. Freeland, G. Srajer, J. Stremper, G. Khaliullin, J. C. Cezar, T. Charlton, R. Dalgliesh, C. Bernhard, G. Cristiani, H.-U. Habermeier, and B. Keimer, *Nat Phys* **2**, 244 (2006).
- [2] R. Werner, C. Raisch, A. Ruosi, B. A. Davidson, P. Nagel, M. Merz, S. Schuppler, M. Glaser, J. Fujii, T. Chassé, R. Kleiner, and D. Koelle, *Phys. Rev. B* **82**, 224509 (2010).
- [3] D. K. Satapathy, M. A. Uribe-Laverde, I. Marozau, V. K. Malik, S. Das, T. Wagner, C. Marcelot, J. Stahn, S. Brück, A. Rühm, S. Macke, T. Tietze, E. Goering, A. Frañó, J. H. Kim, M. Wu, E. Benckiser, B. Keimer, A. Devishvili, B. P. Toperverg, M. Merz, P. Nagel, S. Schuppler, and C. Bernhard, *Phys. Rev. Lett.* **108**, 197201 (2012).
- [4] M. A. Uribe-Laverde, S. Das, K. Sen, I. Marozau, E. Perret, A. Alberca, J. Heidler, C. Piamonteze, M. Merz, P. Nagel, S. Schuppler, D. Munzar, and C. Bernhard, *Phys. Rev. B* **90**, 205135 (2014).
- [5] J. Chakhalian, J. W. Freeland, H.-U. Habermeier, G. Cristiani, G. Khaliullin, M. van Veenendaal, and B. Keimer, *Science* **318**, 1114 (2007).
- [6] J. Bardeen, L. N. Cooper, and J. R. Schrieffer, *Phys. Rev.* **106**, 162 (1957).
- [7] W. Heisenberg, *Zeitschrift für Physik* **49**, 619.
- [8] J. Orenstein and A. J. Millis, *Science* **288**, 468 (2000).
- [9] A. B. Karki, V. O. Garlea, R. Custelcean, S. Stadler, E. W. Plummer, and R. Jin, *Proc Natl Acad Sci U S A* **110**, 9283 (2013).
- [10] J. Wen, G. Xu, G. Gu, J. M. Tranquada, and R. J. Birgeneau, *Reports on Progress in Physics* **74**, 124503 (2011).
- [11] A. I. Buzdin and A. S. Mel'nikov, *Phys. Rev. B* **67**, 020503 (2003).
- [12] J. S. Jiang, D. Davidović, D. H. Reich, and C. L. Chien, *Phys. Rev. Lett.* **74**, 314 (1995).
- [13] R. S. Keizer, S. T. B. Goennenwein, T. M. Klapwijk, G. Miao, G. Xiao, and A. Gupta, *Nature* **439**, 825 (2006).
- [14] Z. Sefrioui, D. Arias, V. Peña, J. E. Villegas, M. Varela, P. Prieto, C. León, J. L. Martinez, and J. Santamaria, *Phys. Rev. B* **67**, 214511 (2003).
- [15] K. Dybko, K. Werner-Malento, M. Sawicki, and P. Przyslupski, *EPL (Europhysics Letters)* **85**, 57010 (2009).
- [16] V. Peña, Z. Sefrioui, D. Arias, C. Leon, J. Santamaria, J. L. Martinez, S. G. E. te Velthuis, and A. Hoffmann, *Phys. Rev. Lett.* **94**, 057002 (2005).
- [17] V. N. Krivoruchko, *Journal of Experimental and Theoretical Physics* **84**, 300.

- [18] C. Bell, E. J. Tarte, G. Burnell, C. W. Leung, D.-J. Kang, and M. G. Blamire, *Phys. Rev. B* **68**, 144517 (2003).
- [19] A. Mani, T. Geetha Kumary, and J. G. Lin, *Sci Rep* **5**, 12780 (2015).
- [20] I. Bozovic, G. Logvenov, M. A. J. Verhoeven, P. Caputo, E. Goldobin, and T. H. Geballe, *Nature* **422**, 873 (2003).
- [21] P. Przyslupski, I. Komissarov, W. Paszkowicz, P. Dluzewski, R. Minikayev, and M. Sawicki, *Phys. Rev. B* **69**, 134428 (2004).
- [22] J. Stahn, J. Chakhalian, C. Niedermayer, J. Hoppler, T. Gutberlet, J. Voigt, F. Treubel, H.-U. Habermeier, G. Cristiani, B. Keimer, and C. Bernhard, *Phys. Rev. B* **71**, 140509 (2005).
- [23] A. Hoffmann, S. G. E. te Velthuis, Z. Sefrioui, J. Santamaría, M. R. Fitzsimmons, S. Park, and M. Varela, *Phys. Rev. B* **72**, 140407 (2005).
- [24] J. Hoppler, J. Stahn, C. Niedermayer, V. K. Malik, H. Bouyanff, A. J. Drew, M. Rossle, A. Buzdin, G. Cristiani, H.-U. Habermeier, B. Keimer, and C. Bernhard, *Nat Mater* **8**, 315 (2009).
- [25] S. R. Giblin, J. W. Taylor, J. A. Duffy, M. W. Butchers, C. Utfeld, S. B. Dugdale, T. Nakamura, C. Visani, and J. Santamaria, *Phys. Rev. Lett.* **109**, 137005 (2012).
- [26] C. Visani, Z. Sefrioui, J. Tornos, C. Leon, J. Briatico, M. Bibes, A. Barthelemy, J. Santamaria, and J. E. Villegas, *Nat Phys* **8**, 539 (2012).
- [27] T. Golod, A. Rydh, V. M. Krasnov, I. Marozau, M. A. Uribe-Laverde, D. K. Satapathy, T. Wagner, and C. Bernhard, *Phys. Rev. B* **87**, 134520 (2013).
- [28] Y. Kalcheim, I. Felner, O. Millo, T. Kirzhner, G. Koren, A. Di Bernardo, M. Egilmez, M. G. Blamire, and J. W. A. Robinson, *Phys. Rev. B* **89**, 180506 (2014).
- [29] M. A. Uribe-Laverde, D. K. Satapathy, I. Marozau, V. K. Malik, S. Das, K. Sen, J. Stahn, A. Rühm, J.-H. Kim, T. Keller, A. Devishvili, B. P. Toperverg, and C. Bernhard, *Phys. Rev. B* **87**, 115105 (2013).
- [30] A. Alberca, M. A. Uribe-Laverde, Y. W. Windsor, M. Ramakrishnan, L. Rettig, I. Marozau, J.-M. Tonnerre, J. Stahn, U. Staub, and C. Bernhard, *Phys. Rev. B* **92**, 174415 (2015).
- [31] J. Salafranca and S. Okamoto, *Phys. Rev. Lett.* **105**, 256804 (2010).
- [32] J. Salafranca, J. Rincón, J. Tornos, C. León, J. Santamaria, E. Dagotto, S. J. Pennycook, and M. Varela, *Phys. Rev. Lett.* **112**, 196802 (2014).
- [33] X. Shi, G. Logvenov, A. T. Bollinger, I. Božović, C. Panagopoulos, and D. Popović, *Nat Mater* **12**, 47 (2013).
- [34] A. Suter, E. Morenzoni, T. Prokscha, B. M. Wojek, H. Luetkens, G. Nieuwenhuys, A. Gozar, G. Logvenov, and I. Božović, *Phys. Rev. Lett.* **106**, 237003 (2011).
- [35] J. G. Bednorz and K. A. Müller, *Zeitschrift für Physik B Condensed Matter* **64**, 189.
- [36] J. M. TARASCON, L. H. GREENE, W. R. MCKINNON, G. W. HULL, and T. H. GEBALLE, *Science* **235**, 1373 (1987).
- [37] R. J. Cava, R. B. van Dover, B. Batlogg, and E. A. Rietman, *Phys. Rev. Lett.* **58**, 408 (1987).

- 
- [38] M. K. Wu, J. R. Ashburn, C. J. Torng, P. H. Hor, R. L. Meng, L. Gao, Z. J. Huang, Y. Q. Wang, and C. W. Chu, *Phys. Rev. Lett.* **58**, 908 (1987).
- [39] R. J. Cava, B. Batlogg, R. B. van Dover, D. W. Murphy, S. Sunshine, T. Siegrist, J. P. Remeika, E. A. Rietman, S. Zahurak, and G. P. Espinosa, *Phys. Rev. Lett.* **58**, 1676 (1987).
- [40] M. Naito, A. Tsukada, T. Greibe, and H. Sato, *Proc. SPIE* **4811**, 140 (2002).
- [41] M. Reehuis, C. Ulrich, K. Prokeš, A. Gozar, G. Blumberg, S. Komiya, Y. Ando, P. Pattison, and B. Keimer, *Phys. Rev. B* **73**, 144513 (2006).
- [42] M. A. Kastner, R. J. Birgeneau, G. Shirane, and Y. Endoh, *Rev. Mod. Phys.* **70**, 897 (1998).
- [43] N. Plakida, *High-Temperature Cuprate Superconductors* (Springer Berlin Heidelberg, 2010).
- [44] M. Imada, A. Fujimori, and Y. Tokura, *Rev. Mod. Phys.* **70**, 1039 (1998).
- [45] J. Zaanen, G. A. Sawatzky, and J. W. Allen, *Phys. Rev. Lett.* **55**, 418 (1985).
- [46] J. M. Tranquada, S. M. Heald, and A. R. Moodenbaugh, *Phys. Rev. B* **36**, 5263 (1987).
- [47] C. Niedermayer, C. Bernhard, T. Blasius, A. Golnik, A. Moodenbaugh, and J. I. Budnick, *Phys. Rev. Lett.* **80**, 3843 (1998).
- [48] P. W. ANDERSON, *Science* **235**, 1196 (1987).
- [49] C. Bernhard, J. L. Tallon, T. Blasius, A. Golnik, and C. Niedermayer, *Phys. Rev. Lett.* **86**, 1614 (2001).
- [50] D. M. Ginsberg, *Physical Properties of High Temperature Superconductors IV (v. 4)* (World Scientific Pub Co Inc, 1994).
- [51] J. J. Capponi, C. Chailout, A. W. Hewat, P. Lejay, M. Marezio, N. Nguyen, B. Raveau, J. L. Soubeyroux, J. L. Tholence, and R. Tournier, *EPL (Europhysics Letters)* **3**, 1301 (1987).
- [52] Y. Tokura and Y. Tomioka, *Journal of Magnetism and Magnetic Materials* **200**, 1 (1999).
- [53] J. Blasco, J. Garca, J. M. de Teresa, M. R. Ibarra, P. A. Algarabel, and C. Marquina, *Journal of Physics: Condensed Matter* **8**, 7427 (1996).
- [54] I. Marozau, P. T. Das, M. Döbeli, J. G. Storey, M. A. Uribe-Laverde, S. Das, C. Wang, M. Rössle, and C. Bernhard, *Phys. Rev. B* **89**, 174422 (2014).
- [55] J. Geck, P. Wochner, S. Kiele, R. Klingeler, A. Revcolevschi, M. v Zimmermann, B. Bchner, and P. Reutler, *New Journal of Physics* **6**, 152 (2004).
- [56] R. Kilian and G. Khaliullin, *Phys. Rev. B* **60**, 13458 (1999).
- [57] E. Dagotto, T. Hotta, and A. Moreo, *Physics Reports* **344**, 1 (2001).
- [58] M. Opel, *Journal of Physics D: Applied Physics* **45**, 033001 (2012).
- [59] S. Das, *Growth of  $La_{2-x}Sr_xCuO_4/La_{2/3}Ca_{1/3}MnO_3$  superlattices and characterization of their structural, electronic and magnetic properties*, Ph.D. thesis, University of Fribourg, Switzerland (2014).

- [60] SURFACE, always one step ahead, <http://www.surface-tec.com/index.php> (2016).
- [61] K. Oura, M. Katayama, A. V. Zotov, V. G. Lifshits, and A. A. Saranin, *Surface Science* (Springer Berlin Heidelberg, 2003).
- [62] M. Steffen Rössle, *Infrared ellipsometry study of the lattice and charge dynamics in bulk SrTiO<sub>3</sub>, thin SrTiO<sub>3</sub> films, and LaAlO<sub>3</sub>/SrTiO<sub>3</sub> heterostructures*, Ph.D. thesis, University of Fribourg, Switzerland (2012).
- [63] J. Daillant and A. Gibaud, eds., *X-ray and Neutron Reflectivity* (Springer Berlin Heidelberg, 2009).
- [64] V. F. Sears, *Neutron News* **3**, 26 (1992).
- [65] Y. Khaydukov, O. Soltwedel, and T. Keller, *Journal of large-scale research facilities JLSRF* **1** (2015), 10.17815/jlsrf-1-30.
- [66] J. Fink, N. Ncker, E. Pellegrin, H. Romberg, M. Alexander, and M. Knupfer, *Journal of Electron Spectroscopy and Related Phenomena* **66**, 395 (1994).
- [67] J. Stöhr, *Journal of Electron Spectroscopy and Related Phenomena* **75**, 253 (1995), future Perspectives for Electron Spectroscopy with Synchrotron Radiation.
- [68] L. Baumgarten, in *43rd IFF Spring School: "Scattering Methods for Condensed Matter Research: Towards Novel Applications at Future Sources"*, Vol. 33, edited by M. Angst, T. Brckel, D. Richter, and R. Zorn (Forschungszentrum Jülich GmbH, JCNS, PGI, ICS, IAS, Jülich, 2012) pp. F4.1 – F4.37.
- [69] M. Uribe-Laverde, *Magnetic proximity effect in oxide-based superconductor/ferromagnet superlattices*, Ph.D. thesis, University of Fribourg, Switzerland (2014).
- [70] F. de Groot and A. Kotani, *Core Level Spectroscopy of Solids (Advances in Condensed Matter Science)* (CRC Press, 2008).
- [71] V. K. Malik, I. Marozau, S. Das, B. Doggett, D. K. Satapathy, M. A. Uribe-Laverde, N. Biskup, M. Varela, C. W. Schneider, C. Marcelot, J. Stahn, and C. Bernhard, *Phys. Rev. B* **85**, 054514 (2012).
- [72] M. Bosman, M. Watanabe, D. Alexander, and V. Keast, *Ultramicroscopy* **106**, 1024 (2006).
- [73] C. Visani, J. Tornos, N. M. Nemes, M. Rocci, C. Leon, J. Santamaria, S. G. E. te Velthuis, Y. Liu, A. Hoffmann, J. W. Freeland, M. Garcia-Hernandez, M. R. Fitzsimmons, B. J. Kirby, M. Varela, and S. J. Pennycook, *Phys. Rev. B* **84**, 060405 (2011).
- [74] M. Döbeli, *Journal of Physics: Condensed Matter* **20**, 264010 (2008).
- [75] L. R. Doolittle, *Nuclear Instruments and Methods in Physics Research Section B: Beam Interactions with Materials and Atoms* **15**, 227 (1986).
- [76] Å. Mosen, J. E. Boschker, F. Maci, J. W. Wells, P. Nordblad, A. D. Kent, R. Mathieu, T. Tybell, and E. Wahlström, *Journal of Magnetism and Magnetic Materials* **369**, 197 (2014).
- [77] C. Bernhard, J. Humlicek, and B. Keimer, *Thin Solid Films* **455456**, 143 (2004).
- [78] J.A. Woollam Co. Inc., <http://www.jawoollam.com/> (2015).
- [79] Y. Okimoto, T. Katsufuji, T. Ishikawa, T. Arima, and Y. Tokura, *Phys. Rev. B* **55**, 4206 (1997).

- 
- [80] E. Fermi and L. Marshall, *Phys. Rev.* **71**, 666 (1947).
- [81] M. Björck and G. Andersson, *Journal of Applied Crystallography* **40**, 1174 (2007).
- [82] S. Valencia, Z. Konstantinovic, D. Schmitz, A. Gaupp, L. Balcells, and B. Martínez, *Phys. Rev. B* **84**, 024413 (2011).
- [83] F. C. Zhang and T. M. Rice, *Phys. Rev. B* **37**, 3759 (1988).
- [84] D. Meyers, S. Mukherjee, J.-G. Cheng, S. Middey, J.-S. Zhou, J. B. Goodenough, B. A. Gray, J. W. Freeland, T. Saha-Dasgupta, and J. Chakhalian, *Scientific Reports* **3**, 1834 EP (2013), article.
- [85] C. Piamonteze, P. Miedema, and F. M. F. de Groot, *Phys. Rev. B* **80**, 184410 (2009).
- [86] J. P. Crocombette, B. T. Thole, and F. Jollet, *Journal of Physics: Condensed Matter* **8**, 4095 (1996).
- [87] F. M. F. de Groot, *Nat Chem* **4**, 766 (2012).
- [88] B. B. Van Aken, O. D. Jurchescu, A. Meetsma, Y. Tomioka, Y. Tokura, and T. T. M. Palstra, *Phys. Rev. Lett.* **90**, 066403 (2003).
- [89] D. Pesquera, G. Herranz, A. Barla, E. Pellegrin, F. Bondino, E. Magnano, F. Sánchez, and J. Fontcuberta, *Nat Commun* **3**, 1189 (2012).
- [90] G. M. De Luca, G. Ghiringhelli, M. Moretti Sala, S. Di Matteo, M. W. Haverkort, H. Berger, V. Bisogni, J. C. Cezar, N. B. Brookes, and M. Salluzzo, *Phys. Rev. B* **82**, 214504 (2010).
- [91] G. M. De Luca, G. Ghiringhelli, C. A. Perroni, V. Cataudella, F. Chiarella, C. Cantoni, A. R. Lupini, N. B. Brookes, M. Huijben, G. Koster, G. Rijnders, and M. Salluzzo, *Nat Commun* **5** (2014).
- [92] B. T. Thole, P. Carra, F. Sette, and G. van der Laan, *Phys. Rev. Lett.* **68**, 1943 (1992).
- [93] P. Carra, B. T. Thole, M. Altarelli, and X. Wang, *Phys. Rev. Lett.* **70**, 694 (1993).
- [94] C. T. Chen, Y. U. Idzerda, H.-J. Lin, N. V. Smith, G. Meigs, E. Chaban, G. H. Ho, E. Pellegrin, and F. Sette, *Phys. Rev. Lett.* **75**, 152 (1995).
- [95] A. Gupta, G. Q. Gong, G. Xiao, P. R. Duncombe, P. Lecoeur, P. Trouilloud, Y. Y. Wang, V. P. Dravid, and J. Z. Sun, *Phys. Rev. B* **54**, R15629 (1996).
- [96] J. Dreiser, K. S. Pedersen, C. Piamonteze, S. Rusponi, Z. Salman, M. E. Ali, M. Schau-Magnussen, C. A. Thuesen, S. Piligkos, H. Weihe, H. Mutka, O. Waldmann, P. Oppeneer, J. Bendix, F. Nolting, and H. Brune, *Chem. Sci.* **3**, 1024 (2012).
- [97] M. Varela, A. R. Lupini, S. J. Pennycook, Z. Sefrioui, and J. Santamaria, *Solid-State Electronics* **47**, 2245 (2003).
- [98] S. Das, K. Sen, I. Marozau, M. A. Uribe-Laverde, N. Biskup, M. Varela, Y. Khaydukov, O. Soltwedel, T. Keller, M. Döbeli, C. W. Schneider, and C. Bernhard, *Phys. Rev. B* **89**, 094511 (2014).
- [99] MTI Corporation, <http://www.mtixtl.com> (2016).
- [100] CRYSTAL Gmbh, <http://crystal-gmbh.com/en/products.php> (2016).
- [101] M. Z. Cieplak, M. Berkowski, S. Guha, E. Cheng, A. S. Vagelos, D. J. Rabinowitz, B. Wu, I. E. Tofimov, and P. Lindenfeld, *Applied Physics Letters* **65** (1994).

- [102] P. G. Radaelli, D. G. Hinks, A. W. Mitchell, B. A. Hunter, J. L. Wagner, B. Dabrowski, K. G. Vandervoort, H. K. Viswanathan, and J. D. Jorgensen, *Phys. Rev. B* **49**, 4163 (1994).
- [103] N. W. Preyer, R. J. Birgeneau, C. Y. Chen, D. R. Gabbe, H. P. Jenssen, M. A. Kastner, P. J. Picone, and T. Thio, *Phys. Rev. B* **39**, 11563 (1989).
- [104] C. Y. Chen, E. C. Branlund, C. Bae, K. Yang, M. A. Kastner, A. Cassanho, and R. J. Birgeneau, *Phys. Rev. B* **51**, 3671 (1995).
- [105] I. Bose, *Phys. Rev. B* **47**, 11537 (1993).
- [106] S.-P. Kou and Z.-Y. Weng, *The European Physical Journal B* **47**, 37 (2005).
- [107] G. J. Snyder, R. Hiskes, S. DiCarolis, M. R. Beasley, and T. H. Geballe, *Phys. Rev. B* **53**, 14434 (1996).
- [108] K. Dörr, J. M. D. Teresa, K.-H. Müller, D. Eckert, T. Walter, E. Vlahov, K. Nenkov, and L. Schultz, *Journal of Physics: Condensed Matter* **12**, 7099 (2000).
- [109] H. Ju and H. Sohn, *Journal of Magnetism and Magnetic Materials* **167**, 200 (1997).
- [110] H. Luo and H.-H. Wen, *Phys. Rev. B* **89**, 024506 (2014).
- [111] X. Shi, *Magnetotransport Properties in Underdoped High  $T_c$  Superconductors*, Ph.D. thesis, Florida State University, US (2012).
- [112] F. Rullier-Albenque, H. Alloul, and R. Tourbot, *Phys. Rev. Lett.* **87**, 157001 (2001).
- [113] C. J. Adkins, J. M. D. Thomas, and M. W. Young, *Journal of Physics C: Solid State Physics* **13**, 3427 (1980).
- [114] T. I. Baturina, A. Y. Mironov, V. M. Vinokur, M. R. Baklanov, and C. Strunk, *Phys. Rev. Lett.* **99**, 257003 (2007).
- [115] A. Frydman, O. Naaman, and R. C. Dynes, *Phys. Rev. B* **66**, 052509 (2002).
- [116] H. M. Jaeger, D. B. Haviland, B. G. Orr, and A. M. Goldman, *Phys. Rev. B* **40**, 182 (1989).
- [117] T. I. Baturina and V. M. Vinokur, *Annals of Physics* **331**, 236 (2013).
- [118] S. Soltan, J. Albrecht, and H.-U. Habermeier, *Solid State Communications* **135**, 461 (2005).
- [119] S. Senoussi, M. Oussena, M. Ribault, and G. Collin, *Phys. Rev. B* **36**, 4003 (1987).
- [120] S. Soltan, *Interaction of superconductivity and ferromagnetism in YBCO/LCMO heterostructures*, Ph.D. thesis, Universität Stuttgart, Germany (2005).
- [121] S. Yunoki, A. Moreo, E. Dagotto, S. Okamoto, S. S. Kancharla, and A. Fujimori, *Phys. Rev. B* **76**, 064532 (2007).
- [122] J. Tallon, *Applied Superconductivity, IEEE Transactions on* **25**, 1 (2015).
- [123] H.-H. Klauss, W. Wagener, M. Hillberg, W. Kopmann, H. Walf, F. J. Litterst, M. Hücker, and B. Büchner, *Phys. Rev. Lett.* **85**, 4590 (2000).
- [124] K. Beauchamp, T. Wang, G. Spalding, and A. Goldman, *Physica A: Statistical Mechanics and its Applications* **200**, 287 (1993).

- 
- [125] K. Dybko, P. Aleshkevych, M. Sawicki, W. Paszkowicz, and P. Przyslupski, *Journal of Physics: Condensed Matter* **25**, 376001 (2013).
- [126] S. Tanda, S. Ohzeki, and T. Nakayama, *Phys. Rev. Lett.* **69**, 530 (1992).
- [127] E. Stilp, A. Suter, T. Prokscha, E. Morenzoni, H. Keller, B. M. Wojek, H. Luetkens, A. Gozar, G. Logvenov, and I. Božović, *Phys. Rev. B* **88**, 064419 (2013).
- [128] V. Y. Butko, G. Logvenov, N. Boovi, Z. Radovi, and I. Boovi, *Advanced Materials* **21**, 3644 (2009).
- [129] S. Smadici, J. C. T. Lee, S. Wang, P. Abbamonte, G. Logvenov, A. Gozar, C. D. Cavellin, and I. Bozovic, *Phys. Rev. Lett.* **102**, 107004 (2009).
- [130] J. Wu, O. Pelleg, G. Logvenov, A. T. Bollinger, Y.-J. Sun, G. S. Boebinger, M. Vanević, Z. Radović, and I. Božovoć, *Nat Mater* **12**, 877 (2013), letter.
- [131] M. Hücker, H.-H. Klauss, and B. Büchner, *Phys. Rev. B* **70**, 220507 (2004).
- [132] A. Gozar, B. S. Dennis, G. Blumberg, S. Komiya, and Y. Ando, *Phys. Rev. Lett.* **93**, 027001 (2004).
- [133] S. Ono, S. Komiya, A. N. Lavrov, Y. Ando, F. F. Balakirev, J. B. Betts, and G. S. Boebinger, *Phys. Rev. B* **70**, 184527 (2004).
- [134] V. N. Kotov, O. P. Sushkov, M. B. Silva Neto, L. Benfatto, and A. H. Castro Neto, *Phys. Rev. B* **76**, 224512 (2007).
- [135] A. Frydman and Z. Ovadyahu, *Solid State Communications* **94**, 745 (1995).
- [136] K. M. Mertes, D. Simonian, M. P. Sarachik, S. V. Kravchenko, and T. M. Klapwijk, *Phys. Rev. B* **60**, R5093 (1999).
- [137] A. Kurobe and H. Kamimura, *Journal of the Physical Society of Japan* **51**, 1904 (1982).
- [138] I. Raičević, D. Popović, C. Panagopoulos, and T. Sasagawa, *Phys. Rev. B* **81**, 235104 (2010).
- [139] Y. Ando, A. N. Lavrov, and K. Segawa, *Phys. Rev. Lett.* **83**, 2813 (1999).
- [140] J. H. Cho, F. Borsa, D. C. Johnston, and D. R. Torgeson, *Phys. Rev. B* **46**, 3179 (1992).
- [141] S. Wakimoto, S. Ueki, Y. Endoh, and K. Yamada, *Phys. Rev. B* **62**, 3547 (2000).
- [142] B. Lake, H. M. Ronnow, N. B. Christensen, G. Aeppli, K. Lefmann, D. F. McMorrow, P. Vorderwisch, P. Smeibidl, N. Mangkorntong, T. Sasagawa, M. Nohara, H. Takagi, and T. E. Mason, *Nature* **415**, 299 (2002).
- [143] K. Sen *et al.*, unpublished .
- [144] N. F. Mott, *Philosophical Magazine* **19**, 835 (1969).
- [145] S. N. Mott, *Physics Today* **31** (1978).